The Mechanics of Slip at the

Updip Limit of the Seismogenic Zone

Noah John Phillips

Department of Earth and Planetary Sciences

McGill University, Montréal

A thesis submitted to McGill University in partial fulfillment of the requirements of the degree of

Doctor of Philosophy

August, 2019

© Noah John Phillips 2019

ACKNOWLEDGEMENTS

I would first and foremost like to thank Christie Rowe for guiding me through this PhD. Her guidance and support throughout the course of my time at McGill have made this thesis possible, and I have learned and grown (scientifically and otherwise) a great deal.

I have been blessed with an ever growing number of office mates, all of whom have made the 4th floor the best place to work. From beginning to end, Nick Harrichhausen, Erik Young, Randy Williams, and Sam Metteer have provided me with stimulating academic discussions, fruitful alternative plans to academia, and too many evening barley pops to count. Samantha Carruthers has been here through it all, and it may now be time for us to join the circus. Cat Ross is thanked for putting up with much coffee pushing. Caroline Seyler is thanked for infinite scientific discussions, many adventures, and for putting up with me through it all. The grad students, the earth science department, and (of course) Anne Kosowski are thanked for making McGill a wonderful place to do a PhD. The Stoners forced me to keep my stick on the ice.

The Ujiie-supergroup helped a great deal during my visits to Japan. Without their support the field work included in this thesis would not have been possible. In particular, Kohtaro Ujiie has been excited in the science, encouraged creative ideas, and accepted me into his group during my visits. Mamma and Poppa Ross are thanked for hosting me during my time in Texas, getting me out cycling, and for getting me to the hospital.

Finally, I would like to thank my family, who have always wholeheartedly supported me. Without their love and support, none of this would have been possible.

CONTRIBUTION OF AUTHORS

Unless indicated in the outline below, all work presented in this thesis was performed by the author, Noah John Phillips.

- Dr. Christie Rowe: Advisory roll, financial support, help defining thesis questions, and editorial work
- Dr. Kohtaro Ujiie: Introduced student to field area, helped with field work, helped define questions, and provided lab space during stays in Tsukuba
- Dr. Melodie French: Trained student on operation of the triaxial deformation apparatus at Rice University and helped develop an experimental framework to test questions in chapter 3
- Ginta Motohashi: Provided field assistance during field work in Japan
- Ben Belzer: Assisted in experimentation at Rice University and independently performed experiments SM2, SM3, AB2 & AB3 (Chapter 3)
- Lang Shi: Assistance in operation of the scanning electron microscope and electron microprobe at McGill University

ABSTRACT

The world's largest earthquakes occur within the seismogenic zones of subduction thrusts, which lock between large magnitude earthquakes. At the updip limit of seismogenic zones, a transitional zone occurs if the subduction interface is not locked to the trench. Within this transitional zone a range of slip behaviors including seismic slip events propagating to the trench, slow slip events (SSEs), tremor, low frequency events (LFEs) and very low frequency events (VLFEs) are observed using geodetic and seismological data sets. Slip in transitional zones is believed to load the seismogenic zone, and may precede large magnitude earthquakes. Understanding the mechanics of slip in transitional zones is therefore important for characterizing the earthquake cycle.

Exhumed subduction zone fault rocks preserve information about the composition, structure, and behavior of subduction zones. This thesis examines deformation structures from an exhumed, shallow ($T = 190^{\circ}$ C), subduction mélange (the Mugi Mélange, Japan) to provide insights into the mechanics of deformation in shallow transitional zones. Mapping, microstructural observations, experiments, and models are used to characterize the distribution of slip surfaces, and relate the observed surfaces to geophysical observations.

Localized slip in subduction zones is expected to occur in velocity-weakening materials; however, most subducting materials (gabbro, basalt, calcite, and shale) have previously been shown to be velocity-strengthening at the updip limit of seismogenic zones. Field mapping in this study of basaltic blocks and slabs (embedded within a shale matrix) demonstrates that unstable slip occurred along their altered margins, where we document well-developed cataclasites and slip surfaces. We report the first documented occurrence of pseudotachylyte (quenched frictional melt) in a basaltic host, identified through microstructural criteria along the upper altered contact of a

basaltic slab. Deformation in altered basalt is shown to have occurred through cataclasis and frictional sliding, while the surrounding shale matrix deformed through distributed pressure solution accommodated processes.

Triaxial friction experiments were performed on crushed natural altered basalt and shale samples from the Mugi Mélange, at the *in situ* conditions of deformation, to characterize their frictional strengths and rate-and-state friction parameters. The shale is frictionally weaker (μ = 0.4) than altered basalt (μ = 0.6). and exhibits velocity-strengthening (a-b = ~0.01) behavior. Altered basalt exhibits velocity weakening behavior (a-b = ~-0.005), indicating that unstable slip may nucleate and propagate along altered basaltic margins. Numerical models of stress and strain-rates around basaltic blocks embedded in a shale matrix demonstrate that the stress threshold required for frictional failure in altered basalt is reached before the shale with increasing slip-rate. Experimental results are used to calculate critical nucleation lengths for dynamic slip in basaltic blocks with altered margins. At the conditions required to produce LFEs and VLFEs, basaltic blocks on the m- to 10's of m-scale are required to produce dynamic failure. Blocks sitting close to this threshold are hypothesized to produce LFEs and VLFEs.

Altered basalt is a ubiquitous lithology in subduction zones, and may provide a source of velocity-weakening material along which earthquakes can preferentially nucleate and propagate. Incorporation of velocity weakening altered basalt into a velocity strengthening matrix may provide a source for LFEs and VLFEs at near lithostatic pore fluid pressure conditions. Incorporation of blocks into the surrounding matrix may occur more readily around subducted seamounts and ridges.

ABRÉGÉ

Les plus grands séismes du monde se produisent dans des zones sismogéniques de failles de chevauchement de subduction, qui se verrouillent entre des séismes de forte magnitude. À la limite supérieure de zones sismogéniques, une zone de transition se forme si l'interface de subduction n'est pas verrouillée solidairement à la fosse. Dans cette zone de transition, un éventail de comportements de déplacement, incluant des épisodes de glissement sismique qui se propagent jusqu'à la fosse, des épisodes de glissement lent (EGL), des trémors, des séismes de basse fréquence (SBF) et des séismes de très basse fréquence (STBF), sont relevés à la lumière d'ensembles de données géodésiques et sismologiques. Il a été postulé que le glissement dans les zones de transition chargerait la zone sismogénique et pourrait précéder des tremblements de terre de grande magnitude. La compréhension de la mécanique du glissement dans les zones de transition est donc importante pour la caractérisation du cycle sismique.

Les roches faillées exhumées de zones de subduction renferment de l'information sur la composition, la structure et le comportement de ces zones de subduction. Le présent mémoire se penche sur les structures de déformation dans un mélange de subduction (le mélange de Mugi, au Japon) peu profond (T = 190°C) exhumé, afin d'en apprendre davantage sur la mécanique de la déformation dans les zones de transition peu profondes. La cartographie, des observations microstructurales, des expériences et des modèles sont utilisés pour caractériser la répartition des surfaces de glissement et relier les surfaces observées aux observations géophysiques.

Le glissement localisé dans les zones de subduction devrait se produire dans des matériaux qui s'adoucissent en glissement; il a toutefois déjà été démontré que la plupart des matériaux de zones de subduction (gabbro, basalte, calcite et schiste) se durcissent en glissement à la limite supérieure de zones sismogéniques. La cartographie de terrain de blocs et de plaques basaltiques (encastrés

dans une matrice de schiste) réalisée dans le cadre de la présente étude a démontré qu'un glissement instable s'est produit le long de leurs bordures altérées, où nous documentons la présence de cataclasites et de surfaces de glissement bien développées. Nous faisons état du premier cas documenté de pseudotachylite (produit de fusion frictionnelle refroidi rapidement) dans un hôte basaltique, identifiée selon des critères microstructuraux, le long du contact supérieur d'une plaque basaltique altérée. Il est démontré que la déformation dans le basalte altéré s'est opérée par cataclase et glissement rigide, alors que la matrice de schiste l'entourant s'est déformée par des processus distribués modulés par la solution par pression.

Des expériences triaxiales de frottement ont été réalisées sur des échantillons naturels broyés de basaltes altérés et de schiste provenant du mélange de Mugi, aux conditions de la déformation, afin de caractériser leurs résistances au frottement et des paramètres de lois de type vitesse de glissement et état de l'interface "rate-and-state". Le schiste est moins résistant au frottement ($\mu = 0.4$) que le basalte altéré ($\mu = 0.6$) et présente un comportement de durcissement en glissement (a-b = ~0,01). Le basalte altéré présente un comportement d'adoucissement en glissement (a-b = ~-0,005), ce qui indique qu'un glissement instable pourrait commencer et se propager le long de bordures basaltiques altérées. Des modèles numériques des contraintes et vitesses de déformation autour de blocs basaltiques encastrés dans une matrice de schiste démontrent que le seuil de contraintes requis pour la rupture en frottement dans les basaltes altérés est atteint avant l'atteinte de ce seuil dans le schiste quand la vitesse de glissement augmente. Les résultats expérimentaux sont utilisés pour calculer les longueurs de nucléation critiques pour le glissement dynamique dans des blocs basaltiques aux bordures altérées. Aux conditions requises pour produire des SBF et des STBF, des blocs basaltiques de l'ordre de mètres ou de dizaines de

mètres sont nécessaires pour produire une rupture dynamique. Il est postulé que des blocs s'approchant de ce seuil produisent des SBF et des STBF.

Des basaltes altérés sont omniprésents dans les zones de subduction et pourraient constituer une source de matériaux s'adoucissant en glissement le long desquels des séismes peuvent naître et se propager préférentiellement. L'incorporation de basalte altéré à adoucissement en glissement dans une matrice à durcissement en glissement pourrait produire des sources de SBF et de STBF à des conditions quasi-lithostatiques de pression des fluides. L'incorporation de blocs dans une matrice pourrait se produire plus facilement autour de monts marins ou de crêtes subductés. Les expériences futures devront tenir compte des modifications des propriétés frictionnelles de roches subductées découlant de réactions métasomatiques et métamorphiques le long de l'interface de subduction. La nature de ces réactions peut être déterminée à la lumière d'observations sur le terrain de zones de subduction exhumées de différentes profondeurs. Les modèles de dynamique des zones de subduction futurs devront prendre en considération la répartition et la variabilité des paramètres associés à la vitesse de glissement et à l'état de l'interface des unités subductées, afin de mieux caractériser et idéalement, à terme, prédire les mégaséismes.

TABLE OF CONTENTS

Acknow	wledgements	ii
Contri	bution of Authors	iii
Abstra	act	iv
Abrég	é	vi
Table o	of Contents	ix
List of	Figures	xiii
List of	Tables	XV
Chapt	er 1	1
Introdi	uction & Background	
1.1	Why study the geology of subduction zones?	1
1.2	The discovery of transitional zones	2
1.3	The shallow transitional zone	4
1.4	Modelling and experimental perspectives on slow slip phenomena	5
1.5	Geological perspectives on the source of slow slip phenomena	6
1.6	What do subduction zones look like?	7
1.7	The Mugi mélange: A typical shallow transitional zone	8
1.8	Thesis outline and contents	9
1.9	References	10
Chapt	er 2	19
For ho	ow long are pseudotachylytes strong? Rapid alteration of basalt-hosted pseudo	otachylytes
from a	shallow subduction complex	
2.1	Abstract	19
2.2	Introduction	20
2.3	Field Locality and Observations	22

2.4	Pse	eudotachylyte-Bearing Fault	24
2.5	Pse	eudotachylyte Characteristics	26
2.6	Dis	ssolution Rates of Pseudotachylyte	31
2.7	Imp	plications for the Strength of Faults	35
2.8	Cor	nclusions	36
2.9	Acl	knowledgements	37
2.10	Re	eferences	37
Chapte	er 3		42
Friction	nal S	trengths of Subduction Zone Materials at the Updip Limit of the Seismogenic Z	one
3.1	Ab	stract	42
3.2	Intr	roduction	43
3.3	Ma	terials and Methods	45
3.3	3.1	Samples	45
3.3	3.2	X-Ray Diffraction	47
3.3	3.3	Experimental Setup and Procedure	48
3.3	3.4	Rate-and-State Fitting	51
3.3	3.5	Microstructures and Grain Size / Shape Analysis	54
3.4	Res	sults	57
3.4	4.1	X-Ray Diffraction	57
3.4	4.2	Rate-and-State Friction Parameters	58
3.4	4.3	Microstructures of Experimentally-Deformed Samples	60
3.4	4.4	Microstructures of Natural Samples	62
3.5	Inte	erpretations	64
3.5	5.1	Interpretation of Experimental Results and Microstructures	64
3.5	5.2	Comparison of the Natural and Experimental Microstructures	67

3.6	Dis	cussion	69
3.7	Coı	nclusions	74
3.8	Acl	knowledgements	74
3.9	Ref	erences	74
Chapte	er 4		85
Eviden	ce of	Localized Failure Along Altered Basaltic Blocks at the Updip Limit of the S	Seismogenic
Zone: I	Impli	cations for the Shallow Tremor Source	
4.1	Abs	stract	85
4.2	Intr	oduction	86
4.3	Geo	ologic Setting	88
4.4	Fie	ld Observations	89
4.5	Mic	crostructures	94
4.6	Mo	dels of Stress Distributions	96
4.	6.1	Why Model Stress Distributions?	96
4.	6.2	Modelling Methods:	98
4.	6.3	Model Results:	100
4.7	Dis	cussion	101
4.	7.1	What happens when the stress threshold is reached?	101
4.	7.2	Calculations of block sizes required to nucleate a real earthquake	103
4.	7.3	Comparison with geological models from the downdip limit of the seisme	ogenic zone
			105
4.	7.4	Relationship of Seamounts and Ridges to LFEs and VLFEs	107
4.8	Coı	nclusions	107
4.9	Acl	knowledgements	108
4.10	Re	eferences	108
Concli	usion		117

Appendix A	119
Supplementary Materials for Chapter 2	
Appendix B	122
Supplementary Materials for Chapter 3	
Appendix C	131
Supplementary Materials for Chapter 4	

LIST OF FIGURES

Figure 2-1: Location of the reworked pseudotachylytes	21
Figure 2-2: Map of the basalt layer	23
Figure 2-3: Outcrop photo and interpretation of pseudotachylyte-bearing fault	25
Figure 2-4: Microstructures of pseudotachylyte	27
Figure 2-5: Time scales of dissolution for pseudotachylytes	33
Figure 3-1: Geotectonic setting of studied samples	44
Figure 3-2: Typical natural microstructures of basalt-shale interface	46
Figure 3-3: X-Ray Diffraction results	48
Figure 3-4: Experimental friction results	53
Figure 3-5: Methods and definitions for shape and grain size analyses	58
Figure 3-6: Microstructures of shale experiments	61
Figure 3-7: Microstructures of altered basalt experiments	63
Figure 3-8: Grain size distributions	65
Figure 3-9: Velocity dependence of friction with temperature	68
Figure 3-10: Cartoon of the shallow subduction interface	72
Figure 4-1: Maps and stratigraphy of Upper Mugi mélange	87
Figure 4-2: Geologic map of basalt horizon 3	90
Figure 4-3: Geologic map of basalt horizon 1	92
Figure 4-4: Field photos of basaltic block macrostructures	92
Figure 4-5: Representative examples of well developed cataclasites	93
Figure 4-6: Example of fault linking blocks	95
Figure 4-7: Model setup of stress around blocks	97
Figure 4-8: Model results of stress and strain-rates	99
Figure 4-9: Calculations of critical nucleation lengths for basaltic blocks	103

Figure 4-10: Schematic cartoon of the subduction interface	106
Figure A1: Phase maps from EDS maps of the clast-bearing cataclasite	. 120
Figure A2: Photomicrograph and interpretation of the pseudotachylyte bearing fault	. 121
Figure B1: Fabrics observed in polished pucks	. 123
Figure B2: Un-annotated SEM photomicrographs used in the determination of fabrics	. 124
Figure B3: Optical microscopy photomosaics of the natural microstructures	. 125
Figure B4: Comparison between fitting methods from previous studies	. 126
Figure B5: Reitveld results on fresh basalt from the Mugi Mélange	. 127
Figure C1: Relationship between aspect ratio and basaltic block lengths	. 131
Figure C2: Magnetic susceptibility of the basaltic slab at the base of Unit 4	. 132

LIST OF TABLES

Table 2-1: EDS analysis of plagioclase	29
Table 2-2: EDS analysis of the aphanitic matrix	30
Table 3-1: Experimental conditions	49
Table 3-2: Calculated fractal dimensions (D) of the grain size distributions	55
Table 3-3: Mean and median values for shape factors	59
Table 4-1: Summary of results from friction experiments in a triaxial apparatus	101
Table B1: Calculated rate-and-state parameters for each rate step	128
Table B2: Comparison between data fitting methods	129

CHAPTER 1

Introduction & Background

1.1 Why study the geology of subduction zones?

Subduction zones are where the world's largest earthquakes occur (i.e. megathrust earthquakes), and slip along the subduction interface is responsible for 90 – 95 percent of all tsunamis [Keim, 2011; Bilek and Lay, 2018]. These natural disasters are responsible for billions of dollars in damage annually and a substantial loss of life [Shi et al., 2016; Koks et al., 2019]. Megathrust earthquakes are caused by a buildup of elastic strain energy during an interseismic period, and sudden release of that energy during slip along a subduction thrust fault [Wang et al., 2012]. The rates at which elastic strain energy is built up (whether the fault interface locks at all or simply creeps) and how/where the sudden slip occurs is controlled by the physical properties and rheologies of rocks located along the subduction interface [Fagereng, 2011b; Rowe et al., 2011; Avouac, 2015; Gao and Wang, 2017]. These properties are important parameters in models of subduction zone behavior, which hopefully will one day predict when and where large magnitude earthquakes occur [e.g. Lapusta and Rice, 2003; Liu and Rice, 2007; Noda and Lapusta, 2013].

A major challenge in the study of earthquake mechanics is that the rocks where earthquakes nucleate, and through which they propagate, are located at depth in the crust. Earthquakes tend to occur within a thermally defined seismogenic zone, thought to be controlled by changes in rock properties during metamorphism as fault rocks are subducted to depth [*Hyndman et al.*, 1997; *Oleskevich et al.*, 1999; *Moore and Saffer*, 2001; *Moore et al.*, 2007]. This seismogenic zone occurs between ~150-350°C at many locked subduction interfaces (the updip limit corresponding to depths of 5-15 km below the surface depending on the thermal gradient) [*Hyndman et al.*, 1997;

Moore et al., 2007]. Since major drilling projects to date have only accessed ~3 km depth in active subduction fault zones, physical rocks from the seismogenic zone of active megathrusts have not been obtained. A deep International Ocean Drilling Project (IODP; NantroSEIZE) is currently attempting to drill into the updip limit of the seismogenic zone (at 7 km depth and ~150°C; [Tobin and Kinoshita, 2006; Harris et al., 2011]), however it is unclear if the major engineering hurdles will be overcome during the current expedition (IODP #358).

One method of gaining insights into the deformational processes in subduction zones is to study exhumed subduction interfaces (which have been underplated to the accretionary prism, and brought to the surface through erosion and uplift) [e.g. *Moore et al.*, 2007; *Trepmann and Stöckhert*, 2009; *Fagereng*, 2011; *Rowe et al.*, 2011; *Ujiie et al.*, 2018; *Kotowski and Behr*, 2019]. Exhumed subduction zones preserve information about the composition, structure, and behavior of the subduction interface. Slip in exhumed subduction zones was both controlled by, and recorded by, the preserved rocks and structures. Examining these rocks therefore provides constraints on deformation mechanisms and slip partitioning in active subduction interfaces.

1.2 The discovery of transitional zones

In subduction zones where megathrust earthquakes occur (e.g. Nankai, Cascadia, Costa Rica), the subduction interface has been traditionally delineated into locked and creeping zones [e.g. *Thatcher and Rundle*, 1979; *Savage et al.*, 1981; *Ruff and Tichelaar*, 1996; *Hyndman et al.*, 1997; *Oleskevich et al.*, 1999]. Locked zones do not slip between large magnitude earthquakes, accumulating elastic strain energy, which is then released during earthquakes. Creeping zones accommodate slip (at nearly plate tectonic rates) between the oceanic plate and the overriding continent through stable fault creep, and large magnitude earthquakes do not occur within this zone [*Wang and Dixon*, 2004; *Avouac*, 2015]. Stable creeping zones at depth were thought to slowly

and continuously load locked zones until an earthquake occurred. Until the early 2000's, models of subduction zone dynamics used this paradigm to simulate the dynamics of the earthquake cycle [e.g. *Savage*, 1983; *Wang and Dixon*, 2004], however a major shift in our view of subduction zone coupling has occurred over the past 17 years.

A new form of slip was discovered at the downdip limit of subduction zones in the early 2000's. The deployment of a dense array of seismometers in Japan (the Hi-net network) led to the discovery of deep tremor, a long period, low-frequency signal occurring just below the seismogenic zone which had been previously attributed to noise [*Obara*, 2002]. The activity of tremor occurred as clusters in time (days to weeks in length), separated by months, and was attributed to cracking and slip as fluids from the subducting slab were expelled through metamorphism [*Obara*, 2002; *Audet and Bürgmann*, 2014]. A more in-depth analysis of the tremor signal revealed that it was composed of small individual events, known as low frequency events (LFEs) and very-low frequency events (VLFEs), which lacked a high frequency component to the signal [*Shelly et al.*, 2007; *Beroza and Ide*, 2011].

Around the same time that tremor was discovered, geodetic observations (using Global Positioning System (GPS) sites) recorded slow slip at depth during tremor sequences at Cascadia, indicating that slow slip along the subduction interface and tremor were coeval processes [Rogers and Dragert, 2003]. Slow slip (as the name implies) is much slower than typical earthquakes, and in of itself, may not produce seismic signals (i.e. when slow slip occurs without tremor, there may be no seismic record of the process, and when there is a signal, it is very low frequency). Since these original discoveries, slow slip and tremor have been documented along many subduction zones globally, and they are thought to represent a nearly ubiquitous process downdip of locked subduction margins [Beroza and Ide, 2011; Bürgmann, 2018]. While a nearly ubiquitous process,

the interval between, duration of, and regularity of slow slip events varies from subduction zone to subduction zone [*Beroza and Ide*, 2011].

The discovery of slow slip and tremor at the downdip limit of the seismogenic zone has revolutionized our conceptual model of subduction zone coupling. Rather than continuous creep at depth loading the locked portion of subduction zones, slip in transitional zones (between locked and creeping zones) is now thought to load the seismogenic zone, and may precede large magnitude earthquakes [*Obara and Kato*, 2016; *Uchida et al.*, 2016; *Voss et al.*, 2018]. Understanding the mechanisms of slow slip phenomena is therefore important for characterizing the earthquake cycle.

1.3 The shallow transitional zone

With increasing deployments of seismometers and GPS stations, transitional zones have been discovered in other geologic environments. At the San Andreas fault, LFEs [Shelly and Hardebeck, 2010; Thomas et al., 2016] and SSEs [Rousset et al., 2019] have been discovered at depth below Parkfield (the region between the locked and creeping portions of the San Andreas Fault), and shallow SSEs have been long been recorded on continental strike-slip faults [Linde et al., 1996].

Above the updip limit of locked subduction zones, a transitional zone exists if the subduction thrust is not locked to the trench [*McGuire et al.*, 2018]. With increasing deployments of ocean bottom pressure gauges, seismometers, and global positioning systems, slow slip phenomena are now being recorded in this shallow transitional environment. Shallow slow slip [*Wallace et al.*, 2016; *Araki et al.*, 2017] and associated (very-)low-frequency earthquakes [*Obana and Kodaira*, 2009; *Todd et al.*, 2018; *Toh et al.*, 2018] have been documented at Nankai (Japan), Costa Rica, Mexico, and Hikurangi (New Zealand) [*Saffer and Wallace*, 2015].

To date, shallow slow slip phenomena do not appear to uniformly occupy the shallow subduction environment like their deeper counterparts. Shallow slow slip phenomena are predominantly recorded along the margins of subducting oceanic ridges and seamounts [Todd et al., 2018; Toh et al., 2018]. Hypotheses to date for the relationship between subducting seamounts and ridges, and the occurrence of shallow slow slip phenomena include compaction of sediment in front to the subducting ridges and seamounts leading to an increase in pore fluid pressure [Saffer and Wallace, 2015; Toh et al., 2018], and changes in stress distributions around the subducting ridge or seamount [Todd et al., 2018].

1.4 Modelling and experimental perspectives on slow slip phenomena

Most models of slow slip phenomena and subduction zone processes use an approach using rate-and-state friction [*Liu and Rice*, 2005, 2007; *Rubin*, 2008; *Ando et al.*, 2010; *Skarbek et al.*, 2012; *Wei et al.*, 2013, 2015]. Rate-and-state friction empirically describes the shear strength of a sliding material using a logarithmic dependence on velocity, and one to several state terms which describe changes in asperity contact areas and strengths with slip [*Dieterich*, 1978; *Ruina*, 1983; *Marone*, 1998; *Scholz*, 1998]. If a material's strength decreases with increasing velocity, it is called a velocity-weakening material, and unstable slip may nucleate within this material [*Scholz*, 1998].

Using the rate-and-state framework, several methods of producing slow slip and tremor in models have been proposed, including mixing velocity-weakening blocks or patches within velocity-strengthening materials [Ando et al., 2010; Skarbek et al., 2012], tuning the length-scale of a velocity-weakening source region to make it conditionally stable [Liu and Rice, 2005, 2007; Rubin, 2008, 2011], using materials that are velocity-weakening at very low slip speeds and transition to velocity-strengthening with increasing slip speed [Hawthorne and Rubin, 2013], having shear induced dilation decrease the pore fluid pressure during slip [Segall et al., 2010], and

introducing layering of velocity-strengthening and weakening materials [Wei et al., 2013, 2015]. From a modelling perspective, the presence of velocity-weakening materials is a necessary component for models of slow slip phenomena.

1.5 Geological perspectives on the source of slow slip phenomena

From a geological perspective, examining exhumed rocks from transitional zones provides insights into common features between the various settings of slow slip phenomena which may match observed geophysical characteristics. To date, most geologic studies have focussed on characterizing features from the downdip limit of the seismogenic zone in subduction zones [Fagereng et al., 2014, 2017; Hayman and Lavier, 2014; Behr et al., 2018; Ujiie et al., 2018; Kotowski and Behr, 2019], while studies from other transitional zones (e.g. the updip limit of the seismogenic zone and creeping to locked segments of strike-slip faults) are largely absent (one exception being Compton et al. [2017], from an exhumed strike-slip shear zone).

Exhumed rocks from the downdip limit of the seismogenic zone have led to two principal hypotheses on the occurrence of slow slip and tremor. One hypothesis is that strong blocks embedded within a weak matrix may lead to localized failure in the blocks (LFEs and VLFEs) [Fagereng, 2011a; Fagereng et al., 2014; Hayman and Lavier, 2014; Kotowski and Behr, 2019], which in turn would cause an increased strain rate in the matrix (SSE) [Fagereng et al., 2014; Hayman and Lavier, 2014; Beall et al., 2019].

A second hypothesis is that local dehydration leads to fluid overpressures within the weak matrix, causing the formation of shear veins within the matrix. Individual crack-seal events in the quartz veins are thought to be due to successive fluid overpressure events during individual tremor sequences [Fagereng et al., 2017; Ujiie et al., 2018]. The mixture of hydrofracturing and shear slip during vein formation is thought to produce the low frequency signal typical of LFEs and

VLFEs. The repeat time of episodic tremor and slow slip may then arise from a combination of fracture healing and fluid release rates [Fagereng et al., 2017; Ujiie et al., 2018].

This thesis examines a shallow subduction interface that has been exhumed to the surface to gain insights into possible mechanisms for slow slip phenomena at the updip limit of subduction zones. By comparing common features from the updip and downdip limit of seismogenic zones, we gain insights into possible ubiquitous processes which may help explain slow slip phenomena.

1.6 What do subduction zones look like?

Most exhumed subduction interfaces described in the literature are composed of tectonic mélanges [Cowan, 1985; Kimura et al., 2012]. Tectonic mélanges are produced by distributed shear within downgoing sediments above the oceanic plate [Fisher and Byrne, 1987; Moore, 1989; Hashimoto and Kimura, 1999; Kitamura et al., 2005; Fagereng, 2011b; Kimura et al., 2012]. Stronger lithologies, including basaltic slabs and sandstone layers, form boudins within a weaker matrix (usually shale or carbonate) due to viscosity contrasts within these zones of distributed shear [Fagereng and Sibson, 2010; Kimura et al., 2012]. At greater depths, these lithologies are metamorphosed to produce mélanges containing blocks of amphibolite, eclogites, and/or blueschists, embedded within matrixes composed of schists, marbles, serpentinites, and/or blueschists, depending on the materials being subducted, the presence or absence of fluid, and the P-T-t path of subduction [Bebout and Barton, 2002; Angiboust et al., 2011; Tsujimori and Ernst, 2014; Bebout and Penniston-Dorland, 2016; Kotowski and Behr, 2019].

Slip within mélanges is known to be partitioned into different lithologies, and thicknesses of deforming zones depending on the imposed rate of slip [*Ujiie et al.*, 2007; *Kitamura and Kimura*, 2012; *Rowe et al.*, 2013]. At the extreme ends of slip rates, earthquakes tend to partition deformation into mm to cm-thick slip zones, while stable fault creep tends to be accommodated in

weak lithologies across a the width of deforming zones [Rowe et al., 2011]. The total width of deforming zones in subduction zones from the surface down to the base of the seismogenic zone is ~150-350 m [Rowe et al., 2013].

1.7 The Mugi mélange: A typical shallow transitional zone

The Mugi mélange is a typical shallow transitional zone, composed of a $\sim 150 - 200$ mthick tectonic mélange, which was active in the Late Cretaceous. This field locality serves as an excellent analogue for subduction along the present day Nankai trough (SW Japan), as both record high geothermal gradients due to subduction of young oceanic crust and a spreading ridge [Sakaguchi, 1996; Kimura et al., 2007; Harris et al., 2013]. Cropping out along the eastern coast of Shikoku, the Mugi mélange is divided into lower and upper sections, with maximum paleotemperatures of 140°C and 190°C respectively [Ikesawa et al., 2005], separated by an out of sequence thrust [Ohmori et al., 1997; Ikesawa et al., 2005; Kitamura et al., 2005]. Deformation occurred at depths between 6 and 7 km [Ikesawa et al., 2005]. The mélange is internally composed of a sequence of thrust imbricates (units 1-6), with thicknesses ranging from 150 to 190 m, which each have a layer of basalt at their base thought to represent underplated oceanic crust [Shibata et al., 2008]. The temperature and pressure conditions of the Mugi mélange correspond well with the environment of shallow slow slip phenomena [Saffer and Wallace, 2015], and this thesis examines discrete slip surfaces and matrix deformation within the mélange to find geologic evidence for slip at various rates (from earthquake to LFEs to fault creep). By examining shallow subduction interfaces we hope to gain insights into common features within transitional zones from various settings, which may help to explain and model slow slip phenomena.

1.8 Thesis outline and contents

This thesis is composed of three chapters examining the mechanics of slip in shallow subduction zones. In Chapter 2, a localized fault cutting through altered basaltic cataclasite is examined from the upper contact of a basaltic slab at the Mugi mélange. The first reported occurrence of pseudotachylyte (quenched frictional melt: an ancient earthquake) is reported from this fault. Dissolution rates of volcanic glasses are used to show how pseudotachylytes can be replaced by frictionally weak phyllosilicates over time intervals shorter than the megathrust earthquake cycle at depth. I then explain why pseudotachylytes are not reported more commonly from basalt (a ubiquitous subduction zone lithology). Chapter 2 has been published in Earth & Planetary Science Letters.

Experiments reported in Chapter 3 were performed to examine the frictional properties of two units (altered basalt and shale) in the mélange. Microstructures from run-products are compared with natural samples to determine the deformation mechanisms which were active in the mélange. We discuss how the frictional properties of these units may control the propagation of earthquakes in the shallow subduction environment, and how mixing of these two lithologies could lead to slow slip phenomena. Chapter 3 is in review at the *Journal of Geophysical Research*: *Solid Earth*.

In Chapter 4, field based and microstructural observations of cataclasites along the margins of basaltic blocks in the mélange are used to constrain numerical models of stress and strain-rate heterogeneity in mélanges. We show how even though altered basalt is frictionally stronger than the shale matrix, that stress concentrations may lead to localized frictional failure in the altered basalt before the shale. We calculate the length scales required for unstable slip using parameters determined from experiments in Chapter 3, and show how our mapped basalts sit close to this

threshold. Their failure is hypothesized to have produce LFEs and VLFEs. Chapter 4 has been submitted to *Geochemistry, Geophysics, Geosystems*.

Together this work provides evidence of how altered basalt, a ubiquitous subduction zone material, plays an important role in the dynamics of the shallow subduction environment. Altered basalt provides a realistic subduction zone material with velocity-weakening material properties in the shallow subduction interface, which may serve as a preferential pathway for earthquake propagation, and a host for shallow slow slip phenomena (VLFEs and LFEs). This work provides better constraints on input parameters for numerical modellers seeking to simulate slow slip phenomena and also demonstrates the importance of experimental investigation of natural, instead of idealized geologic samples, deformed at *in situ* conditions, for understanding the dynamics of subduction plate boundaries.

1.9 References

- Ando, R., R. Nakata, and T. Hori (2010), A slip pulse model with fault heterogeneity for low frequency earthquakes and tremor along plate interfaces, *Geophys. Res. Lett.*, *37*(L10310), 1–5, doi:10.1029/2010GL043056.
- Angiboust, S., P. Agard, H. Raimbourg, P. Yamato, and B. Huet (2011), Subduction interface processes recorded by eclogite-facies shear zones (Monviso, W. Alps), *Lithos*, *127*, 222–238, doi:10.1016/j.lithos.2011.09.004.
- Araki, E., D. M. Saffer, A. J. Kopf, L. M. Wallace, T. Kimura, Y. Machida, S. Ide, E. Davis, and IODP Expedition 365 Shipboard Scientists (2017), Recurring and triggered slow-slip events near the trench at the Nankai Trough subduction megathrust, *Science* (80-.)., 356, 1157–1160.
- Audet, P., and R. Bürgmann (2014), Possible control of subduction zone slow-earthquake periodicity by silica enrichment., *Nature*, *509*, 389–92, doi:10.1038/nature13391.
- Avouac, J. (2015), From Geodetic Imaging of Seismic and Aseismic Fault Slip to Dynamic

- Modeling of the Seismic Cycle, *Annu. Rev. Earth Planet. Sci.*, *43*, 233–271, doi:10.1146/annurev-earth-060614-105302.
- Beall, A., Å. Fagereng, and S. Ellis (2019), Strength of Strained Two Phase Mixtures: Application to Rapid Creep and Stress Ampli fi cation in Subduction Zone Mélange Geophysical Research Letters, *Geophys. Res. Lett.*, 46, 169–178, doi:10.1029/2018GL081252.
- Bebout, G. E., and M. D. Barton (2002), Tectonic and metasomatic mixing in a high-T, subduction-zone mélange—insights into the geochemical evolution of the slab—mantle interface, *Chem. Geol.*, *187*, 79–106.
- Bebout, G. E., and S. C. Penniston-Dorland (2016), Fluid and mass transfer at subduction interfaces—The field metamorphic record, *Lithos*, 240(243), 228–258, doi:10.1016/j.lithos.2015.10.007.
- Behr, W. M., A. J. Kotowski, and K. T. Ashley (2018), Dehydration-induced rheological heterogeneity and the deep tremor source in warm subduction zones, *Geology*, 46(5), 475–478.
- Beroza, G. C., and S. Ide (2011), Slow Earthquakes and Nonvolcanic Tremor, *Annu. Rev. Earth Planet. Sci.*, 39(1), 271–296, doi:10.1146/annurev-earth-040809-152531.
- Bilek, S. L., and T. Lay (2018), Subduction zone megathrust earthquakes, *Geosphere*, *14*(4), 1468–1500.
- Bürgmann, R. (2018), The geophysics, geology and mechanics of slow fault slip, *Earth Planet*. *Sci. Lett.*, 495, 112–134, doi:10.1016/j.epsl.2018.04.062.
- Compton, K. E., J. D. Kirkpatrick, and G. J. Holk (2017), Tectonophysics Cyclical shear fracture and viscous fl ow during transitional ductile-brittle deformation in the Saddlebag Lake Shear Zone, California, *Tectonophysics*, 708, 1–14, doi:10.1016/j.tecto.2017.04.006.
- Cowan, D. S. (1985), Structural styles in Mesozoic and Cenozoic mélanges in the western Cordillera of North America, *Geol. Soc. Am. Bull.*, *96*(4), 451–462, doi:10.1130/0016-7606(1985)96<451:SSIMAC>2.0.CO;2.

- Dieterich, J. H. (1978), Time-Dependent Friction and the Mechanics of Stick-Slip, *Pure Appl. Geophys.*, *116*, 790–806.
- Fagereng, Å. (2011a), Frequency-size distribution of competent lenses in a block-in-matrix mélange: Imposed length scales of brittle deformation?, *J. Geophys. Res.*, 116, doi:10.1029/2010JB007775.
- Fagereng, Å. (2011b), Geology of the seismogenic subduction thrust interface, *Geol. Soc. London, Spec. Publ.*, *359*, 55–76, doi:10.1144/SP359.4.
- Fagereng, Å., and R. H. Sibson (2010), Mélange rheology and seismic style, *Geology*, *38*(8), 751–754, doi:10.1130/G30868.1.
- Fagereng, Å., G. W. B. Hillary, and J. F. a Diener (2014), Brittle-viscous deformation, slow slip, and tremor, *Geophys. Res. Lett.*, 41(May), 4159–4167, doi:10.1002/2014GL060433.1.
- Fagereng, Å., J. F. A. Diener, F. Meneghini, C. Harris, and A. Kvadsheim (2017), Quartz vein formation by local dehydration embrittlement along the deep, tremorgenic subduction thrust interface, , (1), 1–4.
- Fisher, D., and T. Byrne (1987), Structural evolution of underthrusted sediments, *Tectonics*, 6(6), 775–793.
- Gao, X., and K. Wang (2017), Rheological separation of the megathrust seismogenic zone and episodic tremor and slip, *Nat. Publ. Gr.*, doi:10.1038/nature21389.
- Harris, R., M. Yamano, M. Kinoshita, G. Spinelli, H. Hamamoto, and J. Ashi (2013), A synthesis of heat flow determinations and thermal modeling along the Nankai Trough, Japan, *J. Geophys. Res. Solid Earth*, *118*, 2687–2702, doi:10.1002/jgrb.50230.
- Harris, R. N., F. S. Schierhorn, and G. Spinelli (2011), Heat flow along the NanTroSEIZE transect: Results from IODP Expeditions 315 and 316 offshore the Kii Peninsula, Japan, *Geochemistry, Geophys. Geosystems*, 12(8), 1–18, doi:10.1029/2011GC003593.
- Hashimoto, Y., and G. Kimura (1999), Underplating process from melange formation to duplexing: Example from the Cretaceous Shimanto Belt, Kii Peninsula, southwest Japan, *Tectonics*, *18*(1), 92–107, doi:10.1029/1998TC900014.

- Hawthorne, J. C., and A. M. Rubin (2013), Laterally propagating slow slip events in a rate and state friction model with a velocity-weakening to velocity-strengthening transition, *J. Geophys. Res. Solid Earth*, 118(7), 3785–3808, doi:10.1002/jgrb.50261.
- Hayman, N. W., and L. L. Lavier (2014), The geologic record of deep episodic tremor and slip, *Geology*, 42(3), 195–198, doi:10.1130/G34990.1.
- Hyndman, R. D., M. Yamano, and D. A. Oleskevich (1997), The Seismogenic Zone of Subduction Thrust Faults, *Isl. Arc*, 6, 244–260, doi:10.1785/gssrl.79.4.572.
- Ikesawa, E., G. Kimura, K. Sato, K. Ikehara-Ohmori, Y. Kitamura, A. Yamaguchi, K. Ujiie, and Y. Hashimoto (2005), Tectonic incorporation of the upper part of oceanic crust to overriding plate of a convergent margin: An example from the Cretaceous–early Tertiary Mugi Mélange, the Shimanto Belt, Japan, *Tectonophysics*, 401, 217–230, doi:10.1016/j.tecto.2005.01.005.
- Keim, M. (2011), Cyclones, Tsunamis, and Human Health: The Key Role of Preparedness, *Oceanography*, *19*(2), 40–49, doi:10.5670/oceanog.2006.62.
- Kimura, G., Y. Kitamura, Y. Hashimoto, A. Yamaguchi, T. Shibata, K. Ujiie, and S. Okamoto (2007), Transition of accretionary wedge structures around the up-dip limit of the seismogenic subduction zone, *Earth Planet. Sci. Lett.*, 255(3–4), 471–484, doi:10.1016/j.epsl.2007.01.005.
- Kimura, G., A. Yamaguchi, M. Hojo, Y. Kitamura, J. Kameda, K. Ujiie, Y. Hamada, M. Hamahashi, and S. Hina (2012), Tectonic mélange as fault rock of subduction plate boundary, *Tectonophysics*, *568–569*, 25–38, doi:10.1016/j.tecto.2011.08.025.
- Kitamura, Y., and G. Kimura (2012), Dynamic role of tectonic mélange during interseismic process of plate boundary mega earthquakes, *Tectonophysics*, *568*(569), 39–52, doi:10.1016/j.tecto.2011.07.008.
- Kitamura, Y. et al. (2005), Mélange and its seismogenic roof décollement: A plate boundary fault rock in the subduction zone An example from the Shimanto Belt, Japan, *Tectonics*, 24(5), 1–15, doi:10.1029/2004TC001635.
- Koks, E. E., J. Rozenberg, C. Zorn, M. Tariverdi, M. Vousdoukas, S. A. Fraser, J. W. Hall, and

- S. Hallegatte (2019), A global multi-hazard risk analysis of road and railway infrastructure assets, *Nat. Commun.*, *10*(1), 1–11, doi:10.1038/s41467-019-10442-3.
- Kotowski, A. J., and W. M. Behr (2019), Length scales and types of heterogeneities along the deep subduction interface: Insights from exhumed rocks on Syros Island, Greece, *Geosphere*, *15*, 1–28, doi:10.1130/GES02037.1/4782963/ges02037.pdf.
- Lapusta, N., and J. R. Rice (2003), Nucleation and early seismic propagation of small and large events in a crustal earthquake model, *J. Geophys. Res.*, 108(B4), 1–18, doi:10.1029/2001JB000793.
- Linde, A. T., M. T. Gladwin, M. J. S. Johnston, R. L. Gwyther, and R. G. Bilham (1996), A slow earthquake sequence on the San Andreas fault, *Nature*, *383*, 65–68.
- Liu, Y., and J. R. Rice (2005), Aseismic slip transients emerge spontaneously in three-dimensional rate and state modeling of subduction earthquake sequences, *J. Geophys. Res. B Solid Earth*, *110*(8), 1–14, doi:10.1029/2004JB003424.
- Liu, Y., and J. R. Rice (2007), Spontaneous and triggered aseismic deformation transients in a subduction fault model, *J. Geophys. Res. Solid Earth*, 112(9), 1–23, doi:10.1029/2007JB004930.
- Marone, C. (1998), Laboratory-Derived Friction Laws and Their Application To Seismic Faulting, *Annu. Rev. Earth Planet. Sci.*, 26, 643–696, doi:10.1146/annurev.earth.26.1.643.
- McGuire, J. J., J. A. Collins, E. Davis, K. Becker, and M. Heesemann (2018), A Lack of Dynamic Triggering of Slow Slip and Tremor Indicates That the Shallow Cascadia Megathrust Offshore Vancouver Island Is Likely Locked, *Geophys. Res. Lett.*, 45, 11,095-11,103, doi:10.1029/2018GL079519.
- Moore, J. C. (1989), Tectonics and hydrogeology of accretionary prisms: role of the decollement zone, *J. Struct. Geol.*, 11(1/2), 95–106, doi:10.1016/0191-8141(89)90037-0.
- Moore, J. C., and D. Saffer (2001), Updip limit of the seismogenic zone beneath the accretionary prism of southwest Japan: An effect of diagenetic to low-grade metamorphic processes and increasing effective stress, *Geology*, 29(2), 183–186.

- Moore, J. C., C. Rowe, and F. Meneghini (2007), How Accretionary Prisms Elucidate Seismogenesis in Subduction Zones, in *The Seismogenic Zone of Subduction Thrust Faults*, edited by J. C. Moore and T. H. Dixon, pp. 288–315, Columbia University Press, New York, NY.
- Noda, H., and N. Lapusta (2013), Stable creeping fault segments can become destructive as a result of dynamic weakening., *Nature*, 493(7433), 518–21, doi:10.1038/nature11703.
- Obana, K., and S. Kodaira (2009), Low-frequency tremors associated with reverse faults in a shallow accretionary prism, *Earth Planet. Sci. Lett.*, 287(1–2), 168–174, doi:10.1016/j.epsl.2009.08.005.
- Obara, K. (2002), Nonvolcanic Deep Tremor Associated with Subduction in Southwest Japan, *Science* (80-.)., 296, 1679–1682.
- Obara, K., and A. Kato (2016), Connecting slow earthquakes to huge earthquakes, *Science* (80-.)., 353(6296), 253–258.
- Ohmori, K., A. Taira, H. Tokuyama, A. Sakaguchi, M. Okamura, and A. Aihara (1997), Paleothermal structure of the Shimanto accretionary prism, Shikoku, Japan: Role of an out-of-sequence thrust, *Geology*, 25(4), 327–330, doi:10.1130/0091-7613(1997)025<0327:PSOTSA>2.3.CO;2.
- Oleskevich, D. A., R. D. Hyndman, and K. Wang (1999), The updip and downdip limits to great subduction earthquakes: Thermal and structural models of Cascadia, south Alaska, SW Japan, and Chile, *J. Geophys. Res. Solid Earth*, 104(B7), 14965–14991, doi:10.1029/1999JB900060.
- Rogers, G., and H. Dragert (2003), Episodic Tremor and Slip on the Cascadia Subduction Zone: The Chatter of Silent Slip, *Science* (80-.)., 300, 1942–1944.
- Rousset, B., R. Bürgmann, and M. Campillo (2019), Slow slip events in the roots of the San Andreas fault, *Sci. Adv.*, *5*, 1–7.
- Rowe, C. D., F. Meneghini, and J. C. Moore (2011), Textural record of the seismic cycle: strain-rate variation in an ancient subduction thrust, *Geol. Soc. London, Spec. Publ.*, *359*, 77–95, doi:10.1144/SP359.5.

- Rowe, C. D., J. C. Moore, and F. Remitti (2013), The thickness of subduction plate boundary faults from the seafloor into the seismogenic zone, *Geology*, 41(9), 991–994, doi:10.1130/G34556.1.
- Rubin, A. M. (2008), Episodic slow slip events and rate-and-state friction, *J. Geophys. Res.*, *113*(B11414), 1–18, doi:10.1029/2008JB005642.
- Rubin, A. M. (2011), Designer friction laws for bimodal slow slip propagation speeds, *Geochemistry, Geophys. Geosystems*, 12(4), 1–22, doi:10.1029/2010GC003386.
- Ruff, L. J., and B. W. Tichelaar (1996), What Controls The Seismogenic Plate Interface In Subduction Zones?, in *Subduction top to bottom: Geophysical Monograph 96*, pp. 105–111.
- Ruina, A. (1983), Slip instability and state variable friction laws, *J. Geophys. Res.*, 88(B12), 10,310-10,370.
- Saffer, D. M., and L. M. Wallace (2015), The frictional, hydrologic, metamorphic and thermal habitat of shallow slow earthquakes, *Nat. Geosci.*, 8(8), 594–600, doi:10.1038/ngeo2490.
- Sakaguchi, A. (1996), High paleogeothermal gradient with ridge subduction beneath the Cretaceous Shimanto accretionary prism, southwest Japan, *Geology*, 24(9), 795–798, doi:10.1130/0091-7613(1996)024<0795.
- Savage, J. C. (1983), A Dislocation Model of Strain Accumulation and Release at a Subduction Zone, *J. Geophys. Res.*, 88(B6), 4984–4996.
- Savage, J. C., M. Lisowski, and W. H. Prescott (1981), Geodetic strain measurements in Washington, *J. Geophys. Res.*, 86(B6), 4929–4940, doi:10.1029/JB086iB06p04929.
- Scholz, C. H. (1998), Earthquakes and friction laws, *Nature*, 391, 37–42.
- Segall, P., A. M. Rubin, A. M. Bradley, and J. R. Rice (2010), Dilatant strengthening as a mechanism for slow slip events, *J. Geophys. Res. Solid Earth*, 115(12), 1–31, doi:10.1029/2010JB007449.
- Shelly, D. R., and J. L. Hardebeck (2010), Precise tremor source locations and amplitude variations along the lower crustal central San Andreas Fault, *Geophys. Res. Lett.*, 37(L14301), 1–5, doi:10.1029/2010GL043672.

- Shelly, D. R., G. C. Beroza, and S. Ide (2007), Non-volcanic tremor and low-frequency earthquake swarms., *Nature*, 446(7133), 305–307, doi:10.1038/nature05666.
- Shi, P., X. Yang, W. Xu, and J. Wang (2016), Mapping Global Mortality and Affected Population Risks for Multiple Natural Hazards, *Int. J. Disaster Risk Sci.*, 7(1), 54–62, doi:10.1007/s13753-016-0079-4.
- Shibata, T., Y. Orihashi, G. Kimura, and Y. Hashimoto (2008), Underplating of mélange evidenced by the depositional ages: U-Pb dating of zircons from the Shimanto accretionary complex, southwest Japan, *Isl. Arc*, *17*(3), 376–393, doi:10.1111/j.1440-1738.2008.00626.x.
- Skarbek, R. M., A. W. Rempel, and D. A. Schmidt (2012), Geologic heterogeneity can produce aseismic slip transients, *Geophys. Res. Lett.*, *39*(L21306), 1–5, doi:10.1029/2012GL053762.
- Thatcher, W., and J. B. Rundle (1979), A model for the earthquake cycle in underthrust zones, *J. Geophys. Res.*, 84(B10), 5540–5556, doi:10.1029/JB084iB10p05540.
- Thomas, A. M., G. C. Beroza, and D. R. Shelly (2016), Constraints on the source parameters of low-frequency earthquakes on the San Andreas Fault, *Geophys. Res. Lett.*, 43, 1–8, doi:10.1002/2015GL067173.Received.
- Tobin, H. J., and M. Kinoshita (2006), NanTroSEIZE: The IODP Nankai Trough Seismogenic Zone Experiment, *Sci. Drill.*, (2), 23–27, doi:10.2204/iodp.sd.2.06.2006.
- Todd, E. K. et al. (2018), Earthquakes and Tremor Linked to Seamount Subduction During Shallow Slow Slip at the Hikurangi Margin, New Zealand, *J. Geophys. Res. Solid Earth*, 123, 6769–6783, doi:10.1029/2018JB016136.
- Toh, A., K. Obana, and E. Araki (2018), Distribution of very low frequency earthquakes in the Nankai accretionary prism influenced by a subducting-ridge, *Earth Planet. Sci. Lett.*, 482(March 2011), 342–356, doi:10.1016/j.epsl.2017.10.062.
- Trepmann, C. A., and B. Stöckhert (2009), Microfabric of folded quartz veins in metagreywackes: Dislocation creep and subgrain rotation at high stress, *J. Metamorph. Geol.*, 27, 555–570, doi:10.1111/j.1525-1314.2009.00842.x.

- Tsujimori, T., and W. G. Ernst (2014), Lawsonite blueschists and lawsonite eclogites as proxies for paleo-subduction zone processes: A review, *J. Metamorph. Geol.*, *32*, 437–454, doi:10.1111/jmg.12057.
- Uchida, N., T. Iinumi, R. Nadeau, R. Bürgmann, and R. Hino (2016), Periodic slow slip triggers megathrust earthquakes in northeastern Japan, *Science* (80-.)., 351(6272), 488–492.
- Ujiie, K., A. Yamaguchi, G. Kimura, and S. Toh (2007), Fluidization of granular material in a subduction thrust at seismogenic depths, *Earth Planet. Sci. Lett.*, 259, 307–318, doi:10.1016/j.epsl.2007.04.049.
- Ujiie, K., H. Saishu, Å. Fagereng, N. Nishiyama, M. Otsubo, H. Masuyama, and H. Kagi (2018), An Explanation of Episodic Tremor and Slow Slip Constrained by Crack-Seal Veins and Viscous Shear in Subduction Mélange, *Geophys. Res. Lett.*, 45(11), 5371–5379, doi:10.1029/2018GL078374.
- Voss, N., T. H. Dixon, Z. Liu, R. Malservisi, M. Protti, and S. Schwartz (2018), Do slow slip events trigger large and great megathrust earthquakes?, *Sci. Adv.*, 4, 1–6.
- Wallace, L. M., S. C. Webb, Y. Ito, K. Mochizuki, R. Hino, S. Henrys, S. Y. Schwartz, and A. F. Sheehan (2016), Slow slip near the trench at the Hikurangi subduction zone, New Zealand, *Science* (80-.)., 352(6286), 701–704.
- Wang, K., and T. H. Dixon (2004), "Coupling" Semantics and Science in Earthquake Research, *Eos (Washington. DC).*, 85(18), 180–181, doi:10.1029/2001JB001227.
- Wang, K., Y. Hu, and J. He (2012), Deformation cycles of subduction earthquakes in a viscoelastic Earth, *Nature*, 484(7394), 327–332, doi:10.1038/nature11032.
- Wei, M., Y. Kaneko, Y. Liu, and J. J. McGuire (2013), Episodic fault creep events in California controlled by shallow frictional heterogeneity, *Nat. Geosci.*, *6*(7), 566–570, doi:10.1038/ngeo1835.
- Wei, M., Y. Liu, Y. Kaneko, J. J. McGuire, and R. Bilham (2015), Dynamic triggering of creep events in the Salton Trough, Southern California by regional M ≥ 5.4 earthquakes constrained by geodetic observations and numerical simulations, *Earth Planet. Sci. Lett.*, 427, 1–10, doi:10.1016/j.epsl.2015.06.044.

CHAPTER 2

For how long are pseudotachylytes strong? Rapid alteration of basalt-hosted pseudotachylytes from a shallow subduction complex

Phillips, N.J., Rowe, C.D., & Ujiie, K., 2019, For How Long Are Pseudotachylytes Strong? Rapid Alteration of Basalt Hosted Pseudotachylytes from a Shallow Subduction Complex, Earth and Planetary Science Letters, 518, 108-115.

2.1 Abstract

Basalt is one of the main components of megathrust faults in subduction zones where the world's largest earthquakes are generated. Paradoxically, pseudotachylytes have never been reported from basaltic rocks deformed at conditions compatible with the thermally-defined seismogenic zone. We report the first discovery of pseudotachylyte from oceanic crustal basalt, identified by microstructural criteria. The fault is located within a late Cretaceous subduction complex, the Mugi Mélange, and either formed along the plate interface during subduction or within the upper plate during underplating. After solidifying, the pseudotachylytes were fragmented by cataclasis and subsequently partially hydrated to produce phyllosilicates. Previous experiments using dry, felsic lithologies as starting material have shown that pseudotachylytes can be as strong as their host rock, deterring re-activation and favouring their preservation over geologic time. However, we show that where fluid is present, pseudotachylyte can be replaced by phyllosilicate-rich layers with a low frictional strength. The rate of dissolution is dependent on the bulk composition of the pseudotachylyte, with dissolution of mafic glasses occurring at least three orders of magnitude faster than felsic glasses. Under hydrothermal conditions, the replacement of pseudotachylytes by layers of frictionally weak phyllosilicates is predicted to occur over time

intervals shorter than the megathrust earthquake cycle. This process likely reduces fault strength and promotes reactivation.

2.2 Introduction

Pseudotachylyte (i.e. quenched frictionally-generated melt) is one characteristic feature used to locate paleo-seismic slip surfaces [Sibson, 1975; Cowan, 1999; Rowe and Griffith, 2015]; however, identifying pseudotachylyte in the field is challenging, particularly when the pseudotachylyte is the same color as the host lithology, has been altered, and/or has been overprinted by subsequent deformation [Sibson and Toy, 2006; Kirkpatrick et al., 2009; Kirkpatrick and Rowe, 2013]. For this reason, pseudotachylytes are more frequently reported from crystalline rocks, especially felsic intrusives, where the color contrast between pseudotachylyte (dark) and host rock (light) is high [Kirkpatrick and Rowe, 2013]. Experiments in strong crystalline rocks have shown that solidified pseudotachylyte approaches the same strength as intact host rock [Mitchell et al., 2016; Proctor and Lockner, 2016]. In a natural fault this would likely cause other fractures and joints to slip in subsequent earthquakes resulting in preservation of pseudotachylytes formed during a single slip event [Di Toro et al., 2005; Mitchell et al., 2016].

Within the shallow portion of subduction zones (<300° C), a few pseudotachylytes have been reported within subducted sedimentary rocks and are most commonly found along lithologic boundaries [*Ikesawa et al.*, 2003; *Kitamura et al.*, 2005; *Rowe et al.*, 2005; *Ujiie et al.*, 2007b]. In these localities the color contrast is low between pseudotachylyte (black) and host rock (dark grey to black; [*Meneghini et al.*, 2010]), and the pseudotachylytes show evidence of repeated reworking during subsequent slip [*Ujiie et al.*, 2007b; *Rowe et al.*, 2011]. To date, pseudotachylytes have not been found in basaltic rocks from the seismogenic zone, though in theory they should exist. Experimental pseudotachylytes have been produced in high-velocity rotary shear experiments on

mafic lithologies [Spray, 1988]. Additionally, models of temperature rise during seismic slip in water present environments show that melting can occur if permeability is high in the surrounding material, allowing fluid pressure to dissipate, lowering the effectiveness of thermal pressurization [Rempel and Rice, 2006]. This implies that in fluid present subduction zones, pseudotachylyte formation may occur in areas that are locally dry or when surrounding permeability is high. Here we report the first occurrence of basalt-hosted pseudotachylytes. These pseudotachylytes formed within the thermally-defined seismogenic zone, became reworked during subsequent slip, and

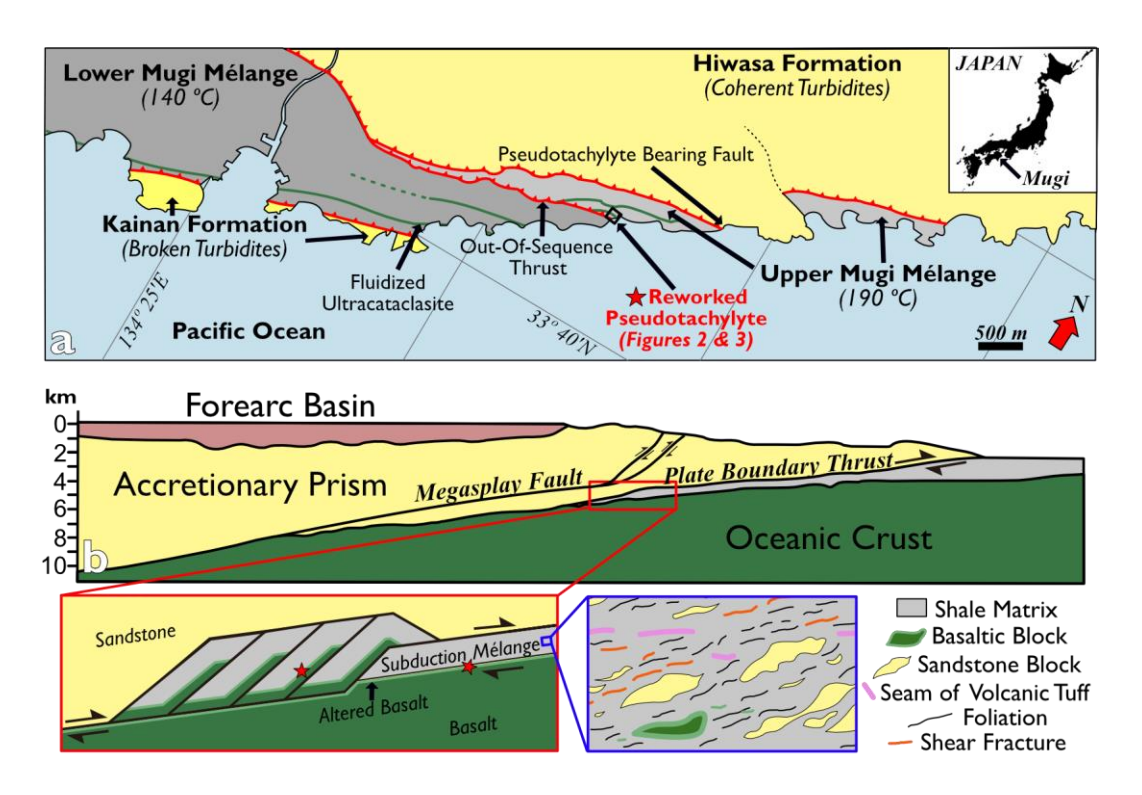


Figure 2-1: a) Location of the reworked pseudotachylytes and other paleo-seismic features within the Mugi Mélange (modified from *Shibata et al.* [2008]). b) Paleo-tectonic setting (with no vertical exaggeration) of the upper Mugi Mélange during pseudotachylyte formation based on present day subduction of the Philippine sea plate beneath the Kii peninsula (Japan) [*Park et al.*, 2002; *Kimura et al.*, 2007]. The reworked pseudotachylyte is hosted in altered basalt along the upper contact of a coherent basaltic layer. The pseudotachylyte could have formed along the subduction interface or during underplating (red stars).

were subsequently altered in the presence of fluids. We estimate the rate of pseudotachylyte alteration and discuss how pseudotachylyte strength should rapidly decrease in faults if water is available.

2.3 Field Locality and Observations

The Mugi mélange is part of a Late Cretaceous subduction complex, and is in fault contact to the north with coherent turbidite sequences, and to the south by broken formation turbidites [Figure 2-1a; *Onishi and Kimura, 1995; Kimura et al., 2012*]. Within the mélange, blocks of sandstone, slivers of tuff, boudinaged blocks of basalt, and 5-60 m thick basaltic layers sit within a shale-dominated tectonic mélange matrix [Figure 2-1; *Shibata et al., 2008*]. The mélange is divided into upper and lower units, with peak paleo-temperatures of 190 °C and 140 °C respectively, separated by an out-of-sequence thrust [Figure 2-1a; *Kitamura et al., 2005*]. Evidence of paleo-seismic slip has previously been reported at two locations in the mélange. Pseudotachylyte occurs at the contact between the mélange and overlying turbidite sequences [*Kitamura et al., 2005*; *Ujiie et al., 2007*b], and a fluidized ultracataclasite with evidence of coseismic heating occurs at the upper edge of a basaltic layer in the lower Mugi mélange [Figure 2-1a; *Ujiie et al., 2007a; Ujiie et al., 2008*]. Evidence for coseismic frictional heating in the fluidized ultracataclasite includes stretched fluid inclusions in fragments of calcite veins [*Ujiie et al., 2008*], and chloritization of smectite within the ultracataclasite [*Kameda et al., 2011*].

We discovered a pseudotachylyte-bearing fault along the upper contact of a 15 m-thick tabular layer of basalt near the base of the upper unit (Figures 2-1, 2-2). The basalt is altered along this contact, with a depth of alteration of 60 cm determined using a field magnetometer (Figure 2-2). Fresh dark grey basalt containing olivine and pyroxene was replaced in the altered margin by chlorite and plagioclase, giving the rock a light green color (Figure 2-3). This alteration

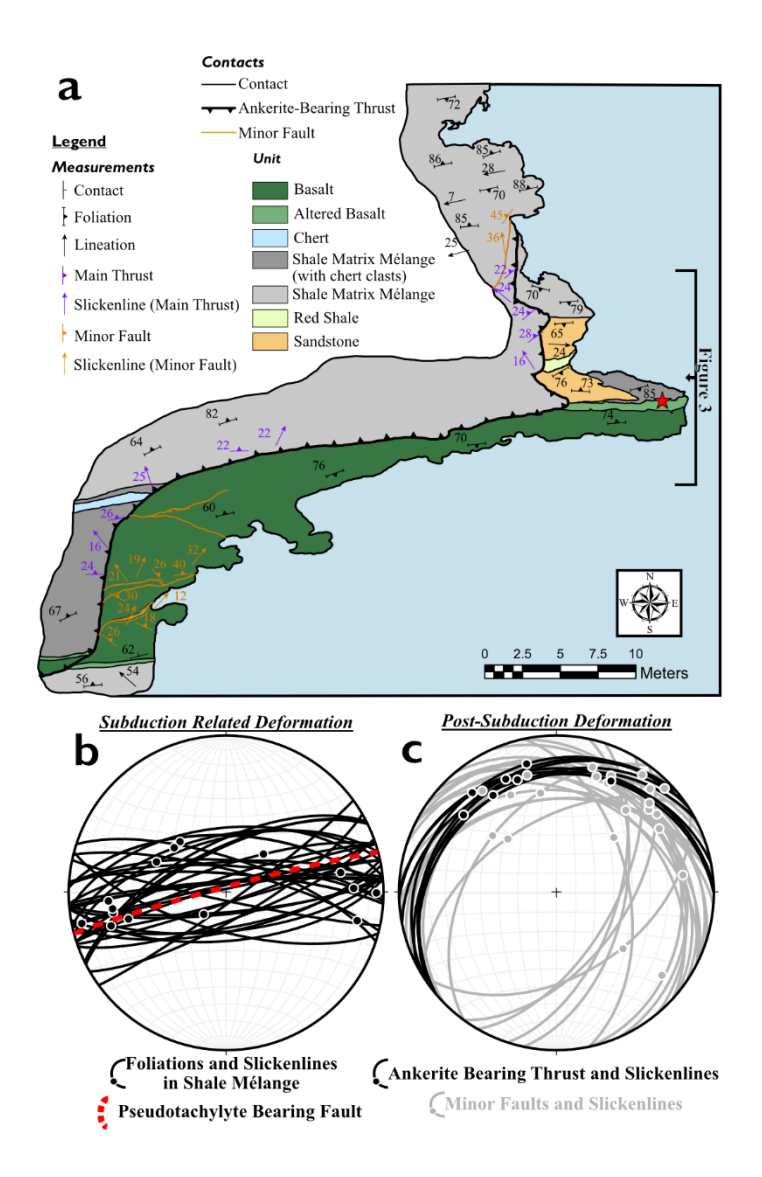


Figure 2-2: a) Map of the basalt layer and location of the reworked pseudotachylytes at the base of the upper Mugi Mélange. East-west striking, steeply dipping foliations in the mélange (consistent with those measured by *Kitamura et al.* [2005]) are indicative of subduction related deformation. These are cross cut by low-angle, ankerite filled faults interpreted to have formed post-subduction (during underplating or within the accretionary prism). b) Lower hemisphere stereonet showing the parallel orientations of the pseudotachylyte-bearing fault and foliations in the shale matrix. c) Lower hemisphere stereonet showing the orientations of the late ankerite-bearing faults.

assemblage is also present along all margins of boudinaged basaltic blocks in the mélange, indicating that alteration of the basalt occurred after development of the block-in-matrix fabric and during distributed deformation in the shale matrix during subduction. Within the altered basalt, plagioclase occurs as sub-rounded crystals on the 100's of microns scale and space between plagioclase crystals is filled by anhedral chlorite, calcite, aggregates of angular Fe-Ti oxides, and minor quartz (Figure 2-4b). No primary basaltic textures or remnants of typical basalt mafic minerals (e.g. pyroxene, olivine) were observed.

An ankerite-bearing thrust fault exists within the field area, and has minor splays into the footwall. These faults cross-cut the fabric of the shale matrix, the altered basalt, and the basaltic layer (Figures 2-2b, 2-3). The ankerite-bearing thrust fault has an orientation of ~320/20N, while minor faults (splays) show a range of orientations (Figure 2-2b, c). The ankerite-bearing thrust fault and splays cross-cut the pseudotachylyte-bearing fault. Cross-cutting relationships indicate that these faults post-date subduction-related distributed deformation in the mélange and the pseudotachylyte-bearing fault. Therefore, they either formed during underplating or during exhumation in the accretionary prism (Figure 2-2).

2.4 Pseudotachylyte-Bearing Fault

The pseudotachylyte-bearing fault was discovered within an altered basaltic sample taken at the contact with the shale matrix (Figures 2-2, 2-3). The pseudotachylyte is found as clasts in the cataclasite and no characteristic field geometries [c.f. Kirkpatrick and Rowe, 2013] were preserved, precluding field identification. The fault is 1 cm thick, has an orientation of 254/87N, and cross-cuts the altered basalt 4 cm from the contact with the shale matrix mélange (e.g. has irregular margins and contains clasts of the altered basalt due to grain plucking at the fault margin; Figures 2-2, 2-4a, A2). No offset markers were observed so offset is unconstrained. The fault is

parallel with the foliation of the shale matrix mélange and the contact between the shale matrix and altered basalt (Figure 2-2c). Given that the fault cross-cuts the altered basalt, has the same orientation as the shale matrix mélange, and is cross cut by the ankerite-bearing faults, we interpret the fault to have formed during subduction- or underplating-related deformation (Figures 2-2, 2-3).

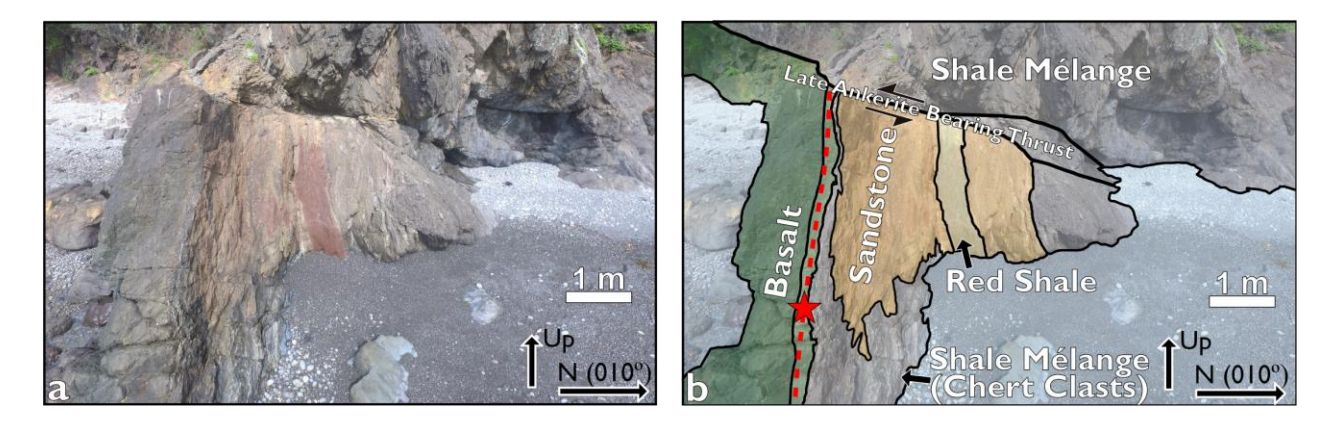


Figure 2-3: Outcrop photo facing west (a) and interpretation (b) showing the distribution of lithologies, inferred projection of the pseudotachylyte-bearing fault based on orientation and sample location (red dashed line), and location of the late ankerite thrust. The red star shows the location of the pseudotachylyte-bearing sample within the altered basalt (Figure 2-4).

The fault contains a light-green, chlorite-rich proto-cataclasite (Figure 2-4b). Clusters of millimeter-scale anhedral chlorite and plagioclase are surrounded by a fine-grained mass of chlorite, with minor pumpellyite. The proto-cataclasite is cut by a cataclasite containing two types of clasts: silicified clasts and sub-rounded dark clasts (pseudotachylyte; Figure 2-4b). Between the sub-rounded dark clasts is an interconnected network of micron-scale chlorite with minor (<5%) corrensite and rutile (Figure A1). The silicified clasts are sub-angular and occur along the boundary with the proto-cataclasite. These clasts are mm-scale, tan in color, and have a weak internal fabric

defined by aligned chlorite. Fabric orientations within the clasts range from sub-parallel to 30° to the fault orientation, indicating rotation during subsequent slip. Energy-dispersive X-ray spectroscopy (EDS) maps (Figure A1) show significant silica enrichment in these clasts compared with other cataclasites, with elemental maps showing up to ~70% quartz. We interpret that these clasts formed during a previous generation of cataclasis, and were subsequently silica-altered and recycled into the cataclasite. The sub-rounded dark clasts (pseudotachylyte) are distributed throughout the cataclasite and range from 10's of microns to 1 mm in diameter. These dark clasts are only found in this cataclasite layer and are described in detail in the next section. A late ultracataclasite injects into the clast-bearing cataclasite (black arrow in Figure 2-4b).

At least three stages of cataclastic deformation (after alteration of the basalt) are identified based on cross cutting relationships. From oldest to youngest these are represented by: 1) the protocataclasite, 2) the clast-bearing cataclasite, and 3) the ultracataclasite. The pseudotachylyte clasts are included in 2), therefore the pseudotachylyte pre-dates the clast-bearing cataclasite.

2.5 Pseudotachylyte Characteristics

The dark rounded clasts of pseudotachylyte have an aphanitic matrix with abundant microcrystallites of various forms. The largest microcrystallites are lath-shaped, zoned plagioclase crystals, 2–20 µm in length with no preferred orientation, and hopper crystals of plagioclase (Figure 2-4c,d). EDS analysis shows that the lath-shaped plagioclase microcrystallites are consistently more calcic (average values 6-7 times greater) than both the aphanitic matrix and plagioclase from the surrounding altered basalt (Figure 2-4d; Table 2-1). The composition of the

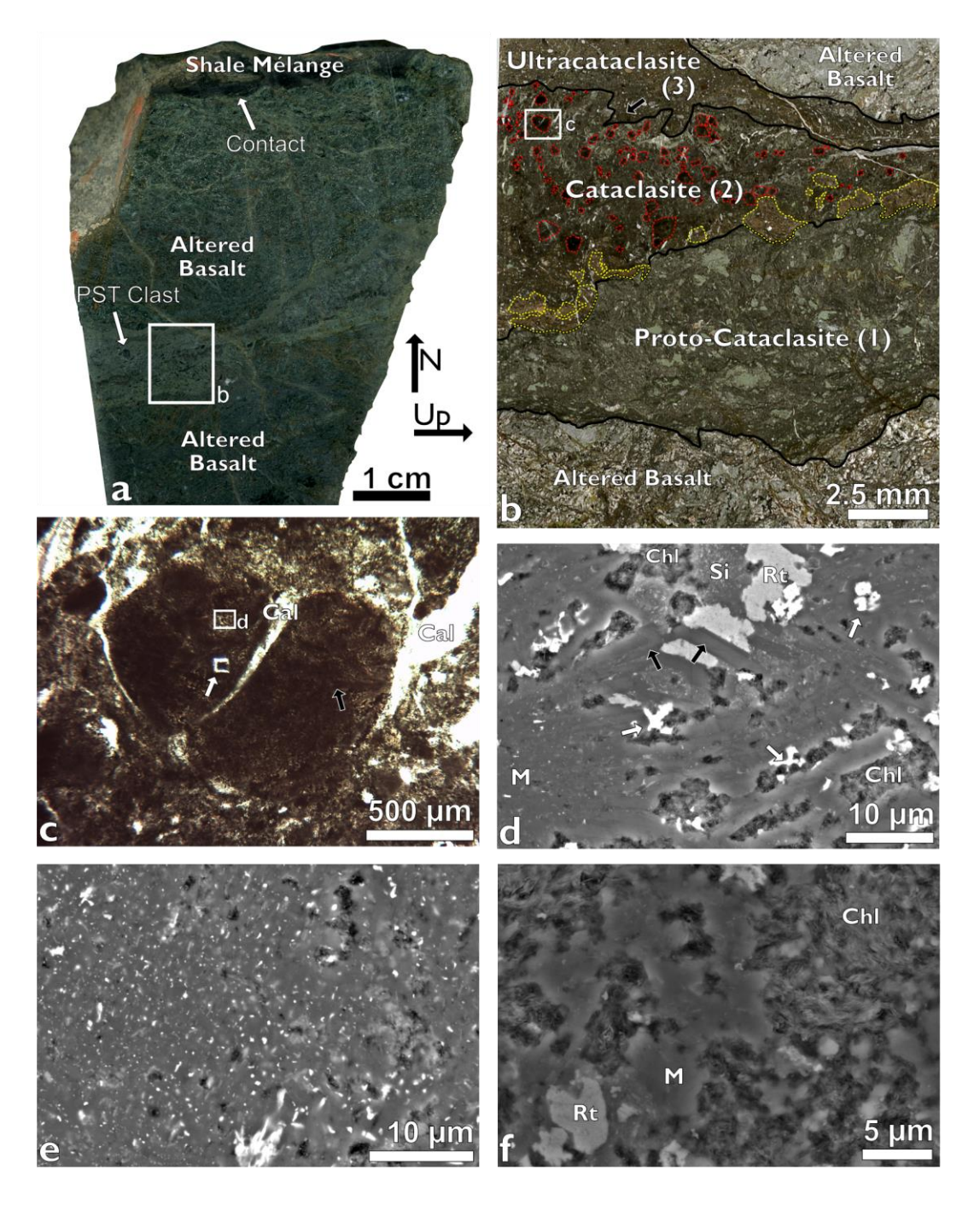


Figure 2-4: Microstructural characteristics of pseudotachylyte and host fault from the upper margin of the basaltic host. a) Hand sample scan showing the pseudotachylyte-bearing fault cutting the altered basalt, and the contact between altered basalt and shale matrix. b) Thin section scan showing dark, sub-rounded clasts (red dashed lines) and silicified clasts (yellow dashed lines) sitting entrained within several generations of cataclasite (see text for details). Numbers indicate generation from oldest (1) to youngest (3). c) The clasts contain lath-shaped

microcrystallites (black arrows) and hopper crystals (white arrow) of plagioclase. d) Backscattered SEM image of the laths reveals zoned crystals of plagioclase with calcic cores (black arrows), cross-shaped oxide phases (white arrows) and rutile with irregular and embayed margins within an aphanitic matrix. e) The aphanitic pseudotachylyte matrix shows evenly spaced oxides (white grains) with no intervening grain boundaries. f) Aphanitic matrix is replaced by micron-scale chlorite platelets along the margins of sub-rounded clasts. (Cal – Calcite; Chl – Chlorite; Rt – Rutile; M – Aphanitic Matrix)

aphanitic matrix approximates the plagioclase in the altered basalt (Tables 2-1, 2-2). Microcrystallites of Fe- and Ti-oxides have anhedral crystal shapes at the nm to µm scale, and when they are greater than 10 µm, either have the cross-shaped habit characteristic of fast quenching from a melt [*Maddock*, 1983; *Lin*, 1994], or irregular and embayed margins indicating marginal melting of survivor grains [rutile in Figure 2-4d; *Ujiie et al.*, 2007b]. Within the aphanitic matrix, smaller (50-200 nm in diameter), evenly spaced microcrystallites of unknown composition are separated by a homogenous groundmass with no visible grain boundaries (Figure 2-4e). The margins of the pseudotachylyte clasts show aphanitic matrix replaced by sub-micron, randomly oriented, platelets of chlorite (Figure 2-4f). This chlorite forms an interconnected matrix between the pseudotachylyte clasts (Figure A1).

Similarly zoned plagioclase microcrystallites in a quenched melt have been observed in melting experiments on greenschist-facies metabasalt (average zoning range of 9% An; Beard and Lofgren, 1991) and pseudotachylytes hosted in plagioclase-rich gneisses [Maddock, 1983]. Plagioclase microcrystallites in natural pseudotachylytes frequently show a wider range in calcite content (compared with plagioclase in the host) due to heterogeneous nucleation during rapid undercooling [Maddock, 1983; Lin, 1994]. Our zoned plagioclases with calcic cores, cross-shaped oxides, hopper crystals of plagioclase, survivor grains with embayed margins, and the evenly

spaced anhedral oxides within an aphanitic groundmass are all characteristic of a melt origin and fast quenching. The pseudotachylyte clasts are distributed within a single layer of a fault that crosscuts the altered basalt, indicating it post-dates alteration of the basalt and did not form during crystallization on the ocean floor. The evidence for rapid undercooling, the planar distribution of clasts, and the cross-cutting relationship with the altered basalt leads us to conclude that the clasts originated as a frictional melt. The composition of the aphanitic matrix (which is nearly identical to albite; Table 2-2) and the presence of plagioclase microcrystallites indicate that albite melted

Table 2-1: EDS analysis of plagioclases from various microstructural domains (Figure 2-4b) and the aphanitic matrix. Analyses were conducted using a Hitachi SEM SU5000 equipped with an Oxford X-MaxN 80 EDS detector for a minimum of 30 s with an accelerating voltage of 15 kV and a working distance of 10 mm. Results were normalized to 8 oxygen per unit formula. Standards are the same as those listed in Table 2-2. Note that calcium contents are low, and equal within error for the altered basalt, aphanitic matrix, and proto-cataclasite, but are always higher and show more variability in the microcrystallites within the pseudotachylytes.

		red Basalt (Host)		rocrystallites Aphanitic ath-shaped) Matrix			<u>Proto-</u> <u>Cataclasite</u>		
		N=13		N=19		N=8		N=16	
	AV	ST DEV	AV	ST DEV	AV	ST DEV	AV	ST DEV	
0	8.00	0.00	8.00	0	8.00	0.00	8.00	0.00	
Na	0.92	0.02	0.62	0.14	0.80	0.02	0.85	0.03	
Al	1.07	0.02	1.20	0.16	1.04	0.01	1.04	0.02	
Si	2.94	0.01	2.81	0.17	2.99	0.01	2.98	0.02	
K	0.01	0.01	0.01	0.01	0.00	0.00	0.00	0.00	
Ca	0.04	0.01	0.26	0.17	0.05	0.01	0.04 0.02		
Total	4.98	0.01	4.91	0.04	4.89	0.01	4.92	0.02	

Table 2-2: EDS compositions of the aphanitic matrix within the rounded pseudotachylyte clasts and albite from the altered basalt (host). Working conditions are the same as described in Table 2-1. Note that the composition of the aphanitic matrix is approximately equivalent to the albite in the host, with slight increases in Fe and Ti (likely due to melting of Fe-Ti oxides).

		Aphanitic	Matrix Wt. %	Albite in A	ltered Basalt
		N=8		N=13	
	STANDARDS	AV	ST DEV	AV	ST DEV
0		48.46	0.49	48.68	0.06
Na	Albite	6.91	0.14	7.98	0.19
Mg	MgO	0.26	0.19	0.01	0.01
Al	Al2O3	10.54	0.10	11.02	0.18
Si	SiO2	31.46	0.48	31.39	0.20
K	KBr	0.07	0.02	0.10	0.09
Ca	Wollastonite	0.79	0.20	0.70	0.20
Ti	Ti	0.43	0.14	0.01	0.01
Fe	Fe	1.10	0.66	0.10	0.03
Total		100.00	0.01	100.00	0.01

during frictional heating, which constrains the peak temperature to be above ~1100°C (Spray, 2010). A minimum temperature increase of ~900 °C above the background temperature of 190 °C is required during slip.

In summary, the basalt was altered during subduction, destroying the primary microstructure and replacing the primary minerals entirely with albite and chlorite. The fault cut through this altered basalt. Pseudotachylyte formed when an earthquake ruptured along the fault, solidifying to form an igneous texture with microcrystallites of plagioclase and oxides whose morphologies are characteristic of fast quenching. The pseudotachylyte was fragmented during subsequent cataclastic deformation. We cannot determine whether this reactivation was caused because the gouge at the pseudotachylyte-wallrock interface was weaker than the altered basalt

host, or whether the margins of the pseudotachylyte were weakened during a previous generation of alteration. In either case the microstructures indicate fracturing of the pseudotachylyte. The fragments were then partially to fully hydrated to form chlorite. The fault was activated again to form the ultracataclasite. In the following sections, we explore approaches for placing constraints on the timescale of hydration of the pseudotachylytes and examine implications for the earthquake cycle.

2.6 Dissolution Rates of Pseudotachylyte

The rounded clasts of pseudotachylyte in our sample are altered along their margins to chlorite due to hydration following crystallization (Fig 4f). Hydration of basaltic glass occurs through congruent silica dissolution, where the glass dissolves, Si is added to the fluid, leaving behind a Si-depleted silicate precipitate on the glass surface [Crovisier et al., 1987; Morin et al., 2015]. Beyond the alteration front, the unaltered glass is homogeneous (e.g. no leaching; Figure 2-4f) and the silicate precipitate is a randomly oriented phyllosilicate or zeolite phase (as observed in both experiments and natural samples; Crovisier et al., 1987; Figure 2-4f). The hydration of pseudotachylyte contributes to fault weakening by facilitating the replacement of strong rocks (basalt) with weaker materials (phyllosilicates). Phyllosilicates have coefficients of friction that are consistently lower than most rocks (Byerlee friction = ~0.7; Byerlee, 1978), including fresh and altered basalt [Zhang et al., 2017], with values of ~0.3 for muscovite, illite and chlorite, and ~0.1 for some smectitic phases [Ikari et al., 2009; Behnsen and Faulkner, 2012]. Replacing pseudotachylyte with phyllosilicates weakens faults by increasing the ratio of phyllosilicate phases to framework silicates [Ikari et al., 2009; Tembe et al., 2010]. Thus, pseudotachylytes replaced by phyllosilicates through hydration may constitute the weak layers in the rock.

The rate of hydration depends on the compositions of the pseudotachylyte and the fluid, the flow rate, and the surface area of contact between the pseudotachylyte and fluid. For basaltic glass in seawater, the rate of dissolution is strongly dependent on temperature and salinity [Morin et al., 2015]. Figure 2-5 shows the minimum time scales for dissolution of basaltic and rhyolitic glasses with thicknesses typical of pseudotachylyte veins assuming dissolution rates follow an Arrhenius relationship with temperature (as seen in experiments) and a fluid composition of sea water [Declercq et al., 2013; Morin et al., 2015]. Dissolution rates are calculated from the experimental data for basaltic glass from Morin et al. (2015) and for rhyolitic glass from Declercq et al. (2013). In both experimental studies forward dissolution rates (r_0) were determined from a series of experiments using a reactor system and crushed glasses where the dissolution rate is defined by

$$r_0 = dNL(Si) / dt$$

where dNL(Si) is a rate of Si loss from the glass, normalized by surface area, and dt is change in time [Morin et al., 2015]. This process is linear unless a precipitate forms on the surface of the glass during dissolution and the precipitate becomes a diffusive barrier which is dependent on the mineralogy of the precipitate [Crovisier et al., 1987]. For phyllosilicates we assume that no diffusive barrier forms given that thin fluid films along phyllosilicate foliae operate as diffusive channels [Renard et al., 1997]. The rate of dissolution of basaltic glass at 90°C is 7.73 x 10⁻⁷ mol m⁻² s⁻¹, while for rhyolitic glass at 80 °C it is 5.01 x 10⁻¹⁰ mol m⁻² s⁻¹ [Declercq et al., 2013; Morin et al., 2015]. Following Morin et al. [2015], we multiply the dissolution rate of rhyolitic glass by 3 to account for the increased concentration of ligands and cations in seawater which promote dissolution [Declercq et al., 2013; Morin et al., 2015], but the outcome is not very sensitive to this assumption. To convert to a thickness over time we use a density and a concentration of Si in the

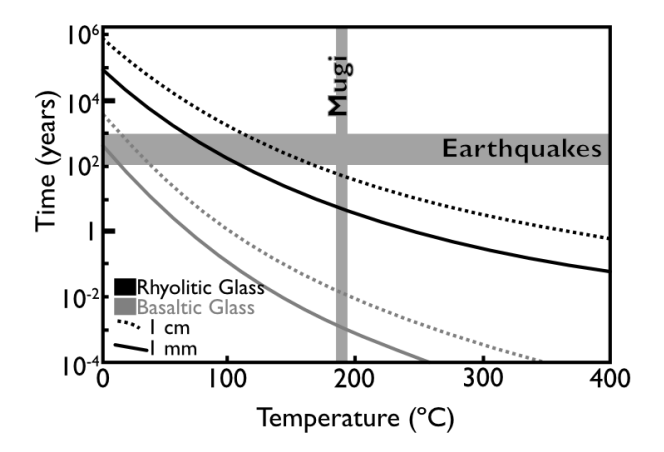


Figure 2-5: Minimum time scales of dissolution for a layer of glass of a given thickness in contact with seawater (see text for details). Glasses with a basaltic composition have dissolution rates at least three orders of magnitude faster than their felsic counterparts. Vertical grey bar shows the temperature conditions of the upper Mugi Mélange, while the horizontal bar shows the range of recurrence intervals for megathrust earthquakes (~M 8) in Japan [Satake, 2015].

glass of 2.7 g cm⁻² and 0.294 g g⁻¹ respectively for basaltic glass, and 2.4 g cm⁻² and 0.35 g g⁻¹ for rhyolitic glass [*Richet et al.*, 2000].

To extrapolate these experimental results to various depths we adopt the assumption of Morin et al. (2015) where there is a dependence on temperature (T) that follows Arrhenius' law, consistent with experimental data, such that

$$\ln(r_0) = \ln(A) - E_a/(RT)$$

where A is a pre-exponential factor, E_a is the activation energy, and R is the gas constant [Morin et al., 2015]. We calculate the pre-exponential factor (a constant) using the above experimental data, and use activation energies of 72 kJ/mol and 55 kJ/mol for basaltic and rhyolitic glasses respectively [Declercq et al., 2013; Morin et al., 2015]. These values are in agreement with previous studies on basaltic [Crovisier et al., 1987; Techer et al., 2001] and rhyolitic glasses [White, 1983].

The timescales presented in Figure 2-5 are minimums, as they assume continual fluid flow of fresh seawater across the pseudotachylyte surface area (removal of exchanged ions through advection). Fluid flux through active faults may be more cyclic due to permeability fluctuations associated with the seismic cycle [e.g. Sibson, 1992], but these rates are probably reasonable in the hours to days after an earthquake when fluid fluxes and permeability are high in faults [Xue et al., 2013]. In the absence of fluid flow, the process would be limited by diffusion which would greatly slow the rate of alteration. Additionally, if fluids at depth are locally enriched in silica the dissolution rate would be reduced. This could occur through dissolution of silica in the shale, which is thought to contribute to distributed deformation in subduction mélanges (i.e. pressure solution; [Kimura et al., 2012] and refs within). However, direct samples of subduction zone fluids have low Si and total dissolved solids no more than 2 times that of seawater above 50 km depth [Manning, 2004], so we consider seawater an appropriate approximation. For a pseudotachylyte with a width of 1 mm at 190 °C, the minimum time to replace a pseudotachylyte of basaltic composition with phyllosilicates under ideal conditions is less than 11 hours, while a rhyolitic composition of the same thickness would take 5 years (Figure 2-5).

These rates are extremely fast when compared with most geologic processes, and may help explain why pseudotachylytes are rarely preserved in subduction zones [Sibson and Toy, 2006], why they are frequently replaced by other minerals [Kirkpatrick and Rowe, 2013 and refs within], and why pseudotachylyte has never before been reported from basalt. However, our pseudotachylyte clasts have aphanitic cores which preserve primary pseudotachylyte microstructures. In order to preserve pseudotachylyte, the pseudotachylyte must be protected from reactive pore water, either by decreasing the permeability of the system following faulting (e.g. through mineral precipitation or formation of a low permeability gouge) or changing to a dry

environment. If pore fluids became silica saturated due to pseudotachylyte dissolution, this might contribute to silica cementation of adjacent cataclasites (as observed in Figure 2-4). We hypothesize that our pseudotachylyte clast cores were protected from hydration through immersion in a low permeability gouge (the ultracataclasite matrix) allowing for their preservation through geologic time.

2.7 Implications for the Strength of Faults

Experiments on fresh natural and experimental pseudotachylytes in granitic rocks and pure quartz sandstones have shown that pseudotachylytes are initially strong after solidification and can weld faults following slip [Mitchell et al., 2016; Proctor and Lockner, 2016; Hayward and Cox, 2017]. In contrast, the basaltic pseudotachylytes in the Mugi mélange have suffered from brittle deformation and alteration following their formation, indicating that the fault continued to accommodate deformation after seismic slip and that reactivation was preferred over the formation of a new fault. This has been observed in other pseudotachylytes from subduction zones [e.g. *Ujiie* et al., 2007b; Meneghini et al., 2010] and major faults [Kirkpatrick and Rowe, 2013 and refs within]. There are several differences between the geologic settings of the faults that show pseudotachylyte welding and the environment of a subduction plate boundary mélange, including lithology and availability of fluids. Hydration of primary pseudotachylyte may occur more readily in a subduction environment where a steady supply of fluids is expected to result from dehydration reactions and compaction along the subducting slab and sediments [Figure 5 from Hyndman and Peacock, 2003; Ujiie and Kimura, 2014]. Fluids are expected to be present in most plate boundary faults as they operate as permeable pathways through the crust. We hypothesize that to maintain fault strength following pseudotachylyte solidification, pseudotachylytes must be protected from hydration and strongly coupled along their interface to the wall rock to prevent reworking during afterslip or interseismic creep. This is probably a typical condition in low permeability granitoids where many well-studied examples of pseudotachylyte are reported [Sibson and Toy, 2006].

We show that pseudotachylytes formed within mafic protoliths are less likely to be preserved than their felsic counterparts due to an increased rate of hydration (Figure 2-5). This may explain the absence of observed pseudotachylytes in mafic lithologies, including from greenstone belts, subduction zones, and transform faults. In order to preserve pseudotachylytes from these environments, permeability must be decreased through mineral precipitation.

At elevated temperatures, pseudotachylytes of both mafic and felsic compositions are hydrated at rates faster than the megathrust earthquake cycle (Figure 2-5). This hydration would lead to a decrease in fault strength by replacing the pseudotachylyte with phyllosilicates, and increase the likelihood of creep and reactivation. In order for pseudotachylyte strength to remain high and to preserve pseudotachylytes in the rock record, a low fluid flux is required, which may be caused by an impermeable host rock, or by reducing permeability through mineral precipitation.

2.8 Conclusions

Pseudotachylyte strength is temporary unless a stringent series of conditions are met. Fault welding and pseudotachylyte preservation are expected to occur where fluid supply is limited: in felsic crystalline host rocks with minimal damage zones and low displacements. In many plate boundary faults, the host rock is dominated by phyllosilicate-rich metasediments or metabasic rocks susceptible to chemical reactions forming weak phyllosilicates. These chemical reactions preferentially remove pseudotachylytes from the rock record. In these faults, pseudotachylyte formation may weaken the fault core following hydration. The long-term effect of frictional melting may be weakening in many fault zones.

2.9 Acknowledgements

N.J.P. is supported by GSA Student Grant 11283-16, the Japan Society for the Promotion of Science KAKENHI grant JP16K21728, and an NSERC PGS-D, C.R. by an NSERC Discovery Grant and Canada Research Chair in Earthquake Geology, and K.U. by the Japan Society for the Promotion of Science KAKENHI grant JP16H06476. The authors would like to thank two anonymous reviewers for constructive comments that improved this manuscript, and editorial handling by Dr. An Yin.

2.10 References

- Beard, J. S., and G. E. Lofgren (1991), Dehydration Melting and Water-Saturated Melting of Basaltic and Andesitic Greenstones and Amphibolites at 1, 3, and 6-9 kb, *J. Petrol.*, 32(2), 365–401.
- Behnsen, J., and D. R. Faulkner (2012), The effect of mineralogy and effective normal stress on frictional strength of sheet silicates, *J. Struct. Geol.*, 42, 49–61, doi:10.1016/j.jsg.2012.06.015.
- Byerlee, J. (1978), Friction of rocks, *Pure Appl. Geophys.*, *116*, 615–626, doi:10.1007/BF00876528.
- Cowan, D. S. (1999), Do faults preserve a record of seismic slip? A field geologist's opinion, *J. Struct. Geol.*, *21*, 995–1001, doi:10.1016/S0191-8141(99)00046-2.
- Crovisier, J. L., J. Honnorez, and J. P. Eberhart (1987), Dissolution of basaltic glass in seawater: Mechanism and rate, *Geochim. Cosmochim. Acta*, *51*, 2977–2990.
- Declercq, J., T. Diedrich, M. Perrot, S. R. Gislason, and E. H. Oelkers (2013), Experimental determination of rhyolitic glass dissolution rates at 40–200 °C and 2 < pH < 10.1, *Geochim. Cosmochim. Acta*, 100, 251–263, doi:10.1016/j.gca.2012.10.006.
- Di Toro, G., S. Nielsen, and G. Pennacchioni (2005), Earthquake rupture dynamics frozen in exhumed ancient faults., *Nature*, *436*(August), 1009–1012, doi:10.1038/nature03910.

- Hayward, K. S., and S. F. Cox (2017), Melt Welding and Its Role in Fault Reactivation and Localization of Fracture Damage in Seismically Active Faults, *J. Geophys. Res. Solid Earth*, 122, 9689–9713, doi:10.1002/2017JB014903.
- Hyndman, R. D., and S. M. Peacock (2003), Serpentinization of the forearc mantle, *Earth Planet. Sci. Lett.*, *212*, 417–432, doi:10.1016/S0012-821X(03)00263-2.
- Ikari, M. J., D. M. Saffer, and C. Marone (2009), Frictional and hydrologic properties of clayrich fault gouge, *J. Geophys. Res. Solid Earth*, *114*, 1–18, doi:10.1029/2008JB006089.
- Ikesawa, E., A. Sakaguchi, and G. Kimura (2003), Pseudotachylyte from an ancient accretionary complex: Evidence for melt generation during seismic slip along a master décollement, *Geology*, *31*(7), 637–640, doi:10.1130/0091-7613.
- Kameda, J., K. Ujiie, A. Yamaguchi, and G. Kimura (2011), Smectite to chlorite conversion by frictional heating along a subduction thrust, *Earth Planet. Sci. Lett.*, 305(1–2), 161–170, doi:10.1016/j.epsl.2011.02.051.
- Kimura, G., Y. Kitamura, Y. Hashimoto, A. Yamaguchi, T. Shibata, K. Ujiie, and S. Okamoto (2007), Transition of accretionary wedge structures around the up-dip limit of the seismogenic subduction zone, *Earth Planet. Sci. Lett.*, 255(3–4), 471–484, doi:10.1016/j.epsl.2007.01.005.
- Kimura, G., A. Yamaguchi, M. Hojo, Y. Kitamura, J. Kameda, K. Ujiie, Y. Hamada, M. Hamahashi, and S. Hina (2012), Tectonic mélange as fault rock of subduction plate boundary, *Tectonophysics*, *568–569*, 25–38, doi:10.1016/j.tecto.2011.08.025.
- Kirkpatrick, J. D., and C. D. Rowe (2013), Disappearing ink: How pseudotachylytes are lost from the rock record, *J. Struct. Geol.*, *52*, 183–198, doi:10.1016/j.jsg.2013.03.003.
- Kirkpatrick, J. D., Z. K. Shipton, and C. Persano (2009), Pseudotachylytes: Rarely generated, rarely preserved, or rarely reported?, *Bull. Seismol. Soc. Am.*, 99(1), 382–388, doi:10.1785/0120080114.
- Kitamura, Y. et al. (2005), Mélange and its seismogenic roof décollement: A plate boundary fault rock in the subduction zone An example from the Shimanto Belt, Japan, *Tectonics*, 24(5), 1–15, doi:10.1029/2004TC001635.

- Lin, A. (1994), Microlite Morphology and Chemistry in Pseudotachylite, from the Fuyun Fault Zone, China, *J. Geol.*, *102*, 317–329.
- Maddock, R. H. (1983), Melt origin of fault-generated pseudotachylytes demonstrated by textures, *Geology*, 11, 105–108.
- Manning, C. E. (2004), The chemistry of subduction-zone fluids, *Earth Planet. Sci. Lett.*, 223, 1–16, doi:10.1016/j.epsl.2004.04.030.
- Meneghini, F., G. Di Toro, C. D. Rowe, J. C. Moore, A. Tsutsumi, and A. Yamaguchi (2010), Record of mega-earthquakes in subduction thrusts: The black fault rocks of pasagshak point (Kodiak Island, Alaska), *Bull. Geol. Soc. Am.*, *122*(7–8), 1280–1297, doi:10.1130/B30049.1.
- Mitchell, T. M., V. Toy, G. Di Toro, J. Renner, and R. H. Sibson (2016), Fault welding by pseudotachylyte formation, *Geology*, 44(12), 1059–1062, doi:10.1130/G38373.1.
- Morin, G. P., N. Vigier, and A. Verney-Carron (2015), Enhanced dissolution of basaltic glass in brackish waters: Impact on biogeochemical cycles, *Earth Planet. Sci. Lett.*, *417*, 1–8, doi:10.1016/j.epsl.2015.02.005.
- Onishi, C. T., and G. Kimura (1995), Change in fabric of melange in the Shimanto Belt, Japan: Change in relative convergence?, *Tectonics*, *14*(5), 1273–1289.
- Park, J., T. Tsuru, T. Hori, S. Kodaira, A. Nakanishi, S. Miura, and Y. Kaneda (2002), A deep strong reflector in the Nankai accretionary wedge from multichannel seismic data: Implications for underplating and interseismic shear stress release, *J. Geophys. Res.*, 107(B4).
- Proctor, B., and D. A. Lockner (2016), Pseudotachylyte increases the post-slip strength of faults, *Geology*, 44(12), 1003–1006, doi:10.1130/G38349.1.
- Rempel, A. W., and J. R. Rice (2006), Thermal pressurization and onset of melting in fault zones, *J. Geophys. Res.*, 111(B09314), 1–18, doi:10.1029/2006JB004314.
- Renard, F., P. Ortoleva, and J. P. Gratier (1997), Pressure solution in sandstones: influence of clays and dependence on temperature and stress, *Tectonophysics*, 280, 257–266,

- doi:10.1016/S0040-1951(97)00039-5.
- Richet, P., A. Whittington, F. Holtz, H. Behrens, S. Ohlhorst, and M. Wilke (2000), Water and the density of silicate glasses, *Contrib. to Mineral. Petrol.*, *138*, 337–347.
- Rowe, C. D., and W. A. Griffith (2015), Do faults preserve a record of seismic slip: A second opinion, *J. Struct. Geol.*, 78, 1–26, doi:10.1016/j.jsg.2015.06.006.
- Rowe, C. D., J. C. Moore, F. Meneghini, and A. W. McKeirnan (2005), Large-scale pseudotachylytes and fluidized cataclasites from an ancient subduction thrust fault, *Geology*, *33*(12), 937–940, doi:10.1130/G21856.1.
- Rowe, C. D., F. Meneghini, and J. C. Moore (2011), Textural record of the seismic cycle: strain-rate variation in an ancient subduction thrust, *Geol. Soc. London, Spec. Publ.*, *359*, 77–95, doi:10.1144/SP359.5.
- Satake, K. (2015), Geological and historical evidence of irregular recurrent earthquakes in Japan, *Philos. Trans. R. Soc. A*, *373*, 1–15.
- Shibata, T., Y. Orihashi, G. Kimura, and Y. Hashimoto (2008), Underplating of mélange evidenced by the depositional ages: U-Pb dating of zircons from the Shimanto accretionary complex, southwest Japan, *Isl. Arc*, *17*(3), 376–393, doi:10.1111/j.1440-1738.2008.00626.x.
- Sibson, R. (1975), Generation of pseudotachylyte by ancient seismic faulting, *Geophys. J. Int.*, 43(3), 775–794, doi:10.1111/j.1365-246X.1975.tb06195.x.
- Sibson, R. H. (1992), Implications of fault-valve behaviour for rupture nucleation and recurrence, *Tectonophysics*, *211*, 283–293, doi:10.1016/0040-1951(92)90065-E.
- Sibson, R. H., and V. G. Toy (2006), The Habitat of Fault-Generated Pseudotachylyte: Presence vs. Absence of Friction-Melt, in *Earthquakes: Radiated energy and the physics of faulting*, edited by R. Abercrombie, A. McGarr, H. Kanamori, and G. Di Toro, pp. 153–166.
- Spray, J. G. (1988), Generation and crystallization of an amphibolite shear melt: an investigation using radial friction welding apparatus, *Contrib. to Mineral. Petrol.*, 99, 464–475.
- Spray, J. G. (2010), Frictional Melting Processes in Planetary Materials: From Hypervelocity

- Impact to Earthquakes, *Annu. Rev. Earth Planet. Sci.*, *38*, 221–254, doi:10.1146/annurev.earth.031208.100045.
- Techer, I., T. Advocat, J. Lancelot, and J.-M. Liotard (2001), Dissolution kinetics of basaltic glasses: control by solution chemistry and protective effect of the alteration film, *Chem. Geol.*, 176, 235–263.
- Tembe, S., D. A. Lockner, and T. F. Wong (2010), Effect of clay content and mineralogy on frictional sliding behavior of simulated gouges: Binary and ternary mixtures of quartz, illite, and montmorillonite, *J. Geophys. Res. Solid Earth*, 115, 1–22, doi:10.1029/2009JB006383.
- Ujiie, K., and G. Kimura (2014), Earthquake faulting in subduction zones: insights from fault rocks in accretionary prisms, *Prog. Earth Planet. Sci.*, *I*(1), 7, doi:10.1186/2197-4284-1-7.
- Ujiie, K., A. Yamaguchi, G. Kimura, and S. Toh (2007a), Fluidization of granular material in a subduction thrust at seismogenic depths, *Earth Planet. Sci. Lett.*, 259, 307–318, doi:10.1016/j.epsl.2007.04.049.
- Ujiie, K., H. Yamaguchi, A. Sakaguchi, and S. Toh (2007b), Pseudotachylytes in an ancient accretionary complex and implications for melt lubrication during subduction zone earthquakes, *J. Struct. Geol.*, 29(4), 599–613, doi:10.1016/j.jsg.2006.10.012.
- Ujiie, K., A. Yamaguchi, and S. Taguchi (2008), Stretching of fluid inclusions in calcite as an indicator of frictional heating on faults, *Geology*, *36*(2), 111–114, doi:10.1130/G24263A.1.
- White, A. (1983), Surface chemistry and dissolution kinetics of glassy rocks at 25°C, *Geochemica Cosmochem. Acta*, 47(1983), 805–815.
- Xue, L. et al. (2013), Continuous Permeability Measurements Record Healing Inside the Wenchuan Earthquake Fault Zone, *Science* (80-.)., 340, 1555–1559.
- Zhang, L., C. He, Y. Liu, and J. Lin (2017), Frictional properties of the South China Sea oceanic basalt and implications for strength of the Manila subduction seismogenic zone, *Mar. Geol.*, 394(December), 16–29, doi:10.1016/j.margeo.2017.05.006.

CHAPTER 3

Frictional Strengths of Subduction Thrust Rocks in the Region of Shallow Slow Earthquakes

Phillips, N.J., Belzer, B., French, M.E., Rowe, C.D. & Ujiie, K., Frictional Strengths of Subduction

Thrust Rocks in the Region of Shallow Slow Earthquakes, In review at the Journal of Geophysical

Research: Solid Earth

3.1 Abstract

Earthquakes are expected to nucleate and propagate within velocity-weakening materials; however, at the updip limit of the seismogenic zone the principal lithologies (shale, basalt, and gabbro) exhibit velocity-strengthening behavior. At an exhumed analogue for present day subduction at Nankai (the Mugi Mélange, Japan) two examples of paleo-seismic features occur within altered basalts at the paleo-plate interface, indicating that altered basalt may be a velocityweakening material. We test the frictional properties of altered basalt and the shale matrix of the mélange through rate-stepping experiments (0.28 to 28 μm/s) in a triaxial deformation apparatus with a saw-cut configuration. Experiments were performed at the in-situ conditions of deformation for the Mugi Mélange (Pc = 120 MPa, T = 150 °C) for two pore fluid factors (Pf = 0.357, 0.7) representing values from present day subduction at Nankai. The shale matrix shows a coefficient of friction between 0.4 and 0.5, and velocity-strengthening behavior as predicted from previous experiments. However, altered basalt exhibits approximately Byerlee friction ($\mu = 0.6$ -0.7) and velocity-weakening behavior, unlike previous experiments on fresh basalt and gabbro which showed velocity-strengthening behavior at these conditions. In most experiments deformation was partitioned into localized Y- and R-Riedel shears, which have higher D values, a lower percentage

of clasts, and shape factors indicating greater roundness of grains than the matrix between shear bands. We hypothesize that the distribution of seismic slip surfaces at Mugi is controlled by the velocity dependence of friction for units in the mélange, with seismic events preferentially nucleating and propagating along the boundaries of velocity-weakening altered basalt and quartz-rich turbidites. More complex forms of deformation (e.g. shallow very low frequency events) may occur by mixing velocity-weakening altered basalt into the velocity-strengthening shale matrix. In subduction zones where the matrix is composed of shale, this complex behavior is limited to shallow depths ($T < \sim 250$ °C), below the transition to velocity-weakening behaviour for the matrix. Altered basalt is an important subduction zone material, and future studies on its behavior through a range of subduction zone conditions is required for a full understanding of the mechanical behavior of subduction zones.

3.2 Introduction

Understanding the mechanics of slip in subduction zones is important for models of the earthquake cycle [Wang et al., 2012]. Depth-related changes in the locked or creeping state of the subduction plate boundary are revealed by seismicity patterns, and geodetic detection of strain and slip [e.g. Bilek and Lay, 1999; Mavrommatis et al., 2014; Avouac, 2015]. Between locked and creeping portions of subduction zones is a transitional zone where slow slip events (SSEs), tremor, and low frequency events (LFEs), collectively known as slow slip phenomena, frequently occur [Obara, 2002; Rogers and Dragert, 2003; Shelly et al., 2007; Beroza and Ide, 2011; Bürgmann, 2018]. Observations of slow slip phenomena are more abundant from the downdip limit of the seismogenic zone where land-based seismic and geodetic networks have better resolution, but advanced processing methods and increasing ocean-bottom instrumentation has revealed similar events at the updip limit, if the subduction thrust is not locked to the trench (Figure 3-1) [e.g.

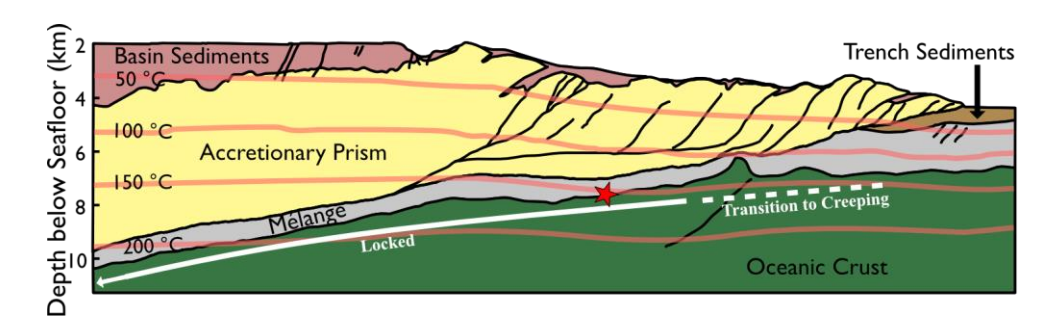


Figure 3-1: Geotectonic setting of the studied samples. Cross-section of the NantroSEIZE site based on seismic reflection data [Moore et al., 2009] with overlain geothermal gradients [Harris et al., 2011; their Model B]. Studied samples come the Mugi Mélange, a Late Cretaceous analogue for the Nankai trough that has been exhumed to the surface. Red star indicates the equivalent position of underplating of the Mugi Mélange samples.

Obana and Kodaira, 2009; Saffer and Wallace, 2015; Araki et al., 2017; Mcguire et al., 2018; Nakano et al., 2018]. The predominant slip behaviour at a given depth (i.e. earthquakes, slow slip, fault creep) is controlled by the frictional properties of subducting materials [Scholz, 1998; Saffer and Marone, 2003; Ikari et al., 2018], particularly in the shallow portion of subduction zones where low temperatures slow down crystal plastic and diffusion-accommodated deformation mechanisms [Kohlstedt et al., 1995]. Understanding the frictional properties of units typical of shallow subduction zones is therefore important for understanding the complex slip behavior of these environments.

Exhumed subduction zone fault rocks preserve information about the composition, structure, and behavior of the subduction plate boundary [Rowe et al., 2005; Fagereng, 2011; Kimura et al., 2012]. Creep, slow slip and seismic propagation in the shallow portion of the subduction thrust are both controlled by, and recorded by, these rocks, which are commonly represented in ancient accretionary complexes as tectonic mélanges [Cowan, 1985; Kimura et al., 2012]. Tectonic mélanges are produced by distributed shear within downgoing sediments above the oceanic plate

[Fisher and Byrne, 1987; Moore, 1989; Hashimoto and Kimura, 1999; Kitamura et al., 2005; Fagereng, 2011; Kimura et al., 2012]. Basaltic slabs (incorporated into the sediments through underplating) and sandstone layers form boudins within a shale dominated matrix due to viscosity contrasts within these zones of distributed shear [Fagereng and Sibson, 2010; Kimura et al., 2012].

Within the Mugi Mélange, Japan, evidence of paleo-seismicity is present along the upper contact of the shale matrix mélange (against coherent offscraped quartz-rich turbidite sequences), and within the center of the mélange along the contacts of incorporated basaltic slabs [Kiminami et al., 1999; Ujiie et al., 2007b; Kameda et al., 2011; Phillips et al., 2019], which have been altered to a mixture of chlorite and albite [Ujiie et al., 2007a; Phillips et al., 2019]. In this paper we examine the frictional properties of the subducting sediment and altered basalt from Mugi, which serves as an on-land analogue for the Nankai trough (Figure 3-1). The experiments in this paper test the frictional properties of these materials to explain why altered basaltic samples host seismic features, and to evaluate potential explanations for some of the more complex styles of slip and seismic behaviors found in shallow subduction zones. Experiments were performed at the in-situ temperatures and pressures of deformation, and explored the range of pore fluid factors observed for the Nankai trough [Kitajima and Saffer, 2012; Tonegawa et al., 2017]. We use microstructural observations to explain the velocity-dependent frictional behavior in experiments and to interpret the deformation history of natural faults in the Mugi Mélange.

3.3 Materials and Methods

3.3.1 Samples

Natural subduction zone samples were collected from the upper Mugi Mélange, part of the Late Cretaceous Shimanto Accretionary Complex in Japan [Kitamura et al., 2005; Kimura et al.,

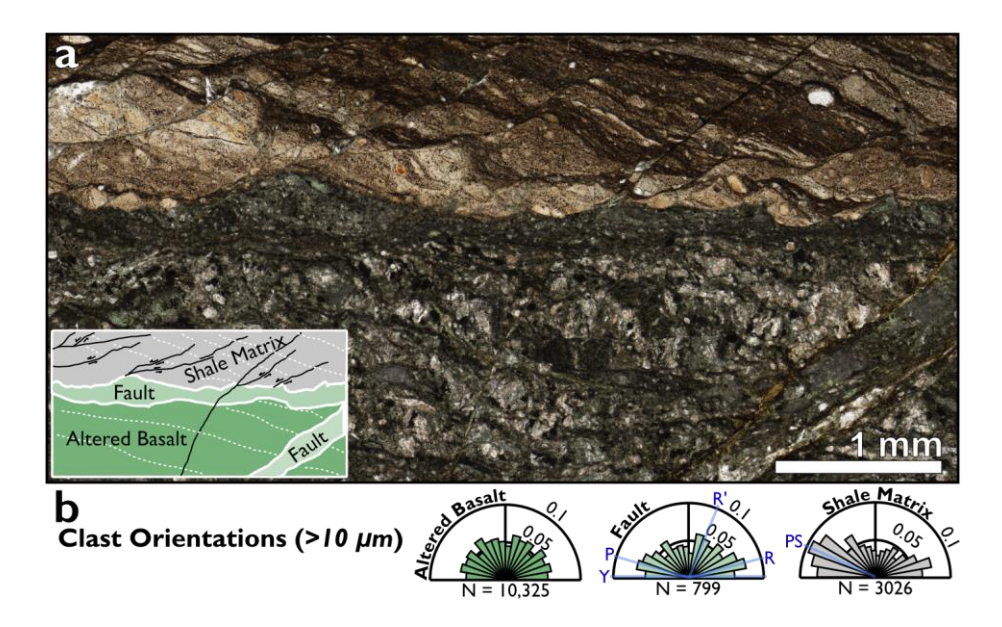


Figure 3-2: a) Typical microstructure from the interface between altered basalt and shale matrix. Shale matrix shows a strong foliation, while localized faults cut the altered basalt along the interface. b) Orientations of clasts (showing the distribution of Feret angles as probability density functions) from each microstructural domain using the grain shape analysis outlined in section 2.5 (note that only the horizontal fault was used for "fault"; reflected light image and images of segregated clasts for each domain are found in Figure B3). Average Riedel shear orientations from Logan [1992] are labelled for the fault, and the orientation of the foliation (PS) is labelled for the shale matrix.

2012]. The mélange is widely recognized as an on-land analogue for present day subduction at Nankai [*Ujiie and Kimura*, 2014], and is composed of a stack of thrust imbricates [*Shibata et al.*, 2008]. Each thrust stack has a similar internal stratigraphy: at the base is a 10-30 m thick layer of basalt (interpreted to be underplated oceanic plate) which is overlain by a mélange with a shale matrix containing blocks of sandstone and basalt, and discontinuous layers of volcanic tuff [*Kitamura et al.*, 2005; *Shibata et al.*, 2008]. The margins of basaltic layers and blocks have been predominantly altered to a mixture of plagioclase and chlorite. Altered basalt occurs as ~60 cm

rims around basaltic blocks and layers [*Phillips et al.*, 2019]. The evidence for localized slip is concentrated within altered basalt, along/near interfaces with shale matrix so the properties of these two lithologies are important for understanding the frictional behavior of these mélanges.

Microstructures of the shale matrix show evidence for distributed deformation, with development of a strong foliation defined by aligned phyllosilicates, clasts of sandstone, and pressure solution seams [Kitamura et al., 2005; Kawabata et al., 2007; Figure 3-2a]. Microstructures in the altered basalt show evidence of localized deformation, with well-developed cataclasites 10's of cm thick and thin through-going faults cutting the altered basaltic unit [Phillips et al., 2019; Figure 3-2a]. The unaltered basalts show little internal deformation. We sampled and performed friction experiments on both the shale from the mélange matrix and the altered basalt from the margin of a basaltic layer to test their frictional properties at in situ conditions. Both samples come from Unit 4. The altered basalt comes from the altered upper surface of the basaltic slab at the base of Unit 4 (Figure 4a), while the shale matrix is a representative sample taken from ~10 m above (stratigraphically) the basaltic slab at the base of Unit 4.

3.3.2 X-Ray Diffraction

The compositions of the starting materials were analyzed using X-Ray Diffraction at McGill University. Samples were crushed by hand in 30s intervals to < 0.5 mm (with sieving between each interval) and were subsequently crushed for 2 minutes using a McCrone Mill. Both random powders and oriented clay separates were prepared [following *Poppe et al.*, 2001] and analyzed. Random powders were back-packed into a sample holder with a glass backing. Random powders were run between 2 and 70 degrees 2θ (Figure 3-3). Oriented clay separates were run dry and glycolated between 2 and 40 degrees 2θ . All runs used a scan speed of 1 degree per minute,

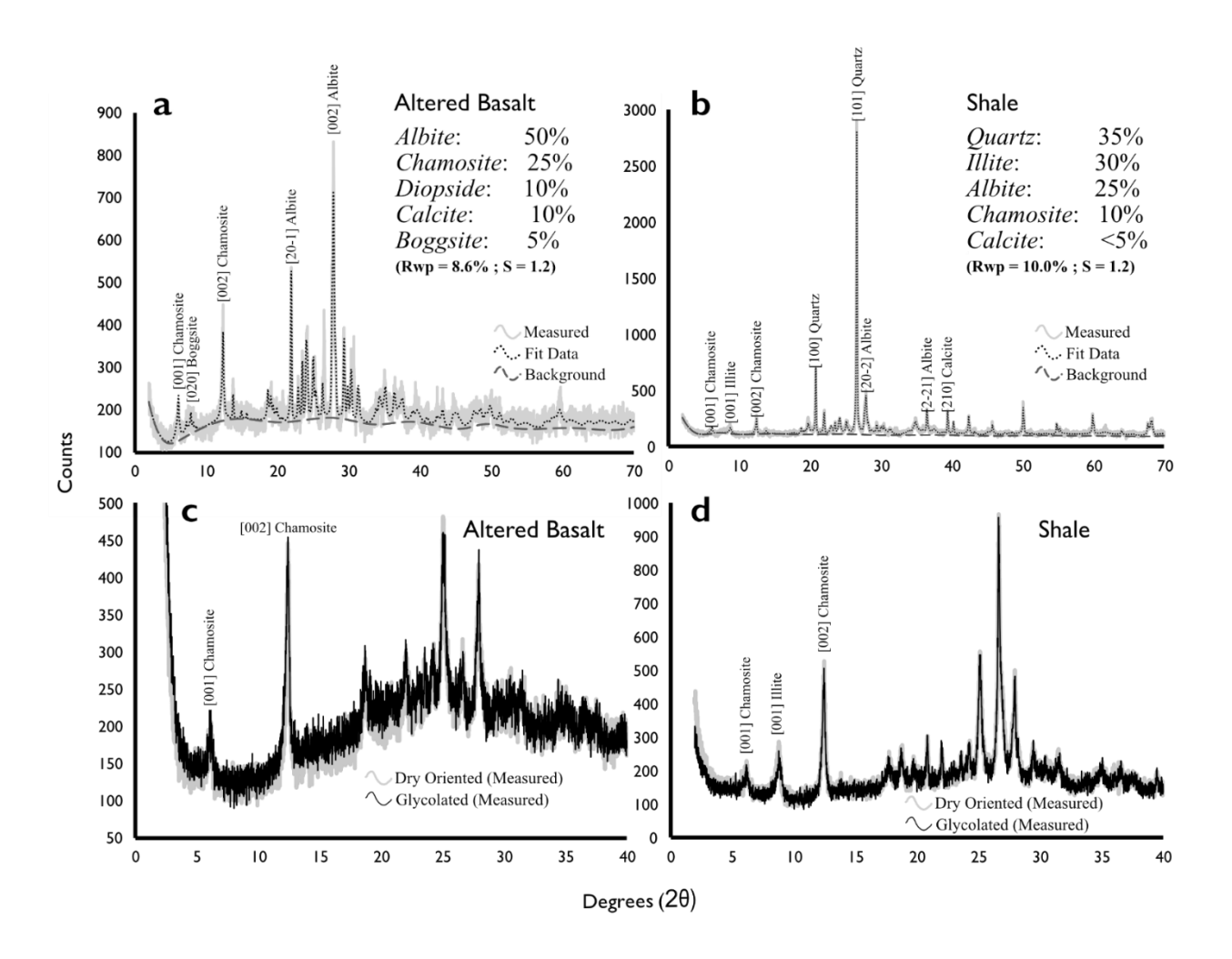


Figure 3-3: X-Ray diffraction patterns of the main lithologies examined in this paper. a & b) Measured, fit, and background obtained from randomly oriented, backpacked mounts. Reitveld results (rounded to the nearest 5%) are shown. c & d) Analysis of dry-oriented and glycolated clay aggregates. No expansion was observed in the clay separates following glycolation. Chamosite was used for chlorite because it provided the best fit to the observed chlorite peaks. and a scan step of 0.01 degrees. Reitveld analysis of the random powder analyses was performed using the software PDXL 2 (Rigaku).

3.3.3 Experimental Setup and Procedure

Experiments were performed using a triaxial rock press housed at Rice University (Figure 3-4a). The rig uses silicon oil as a confining medium and is equipped with servo-controlled

intensifiers to control both confining and pore fluid pressures. External heating coils heat the assembly to a maximum temperature of 150°C, and an internal thermocouple allows the temperature to be measured near the sample. Displacement is measured using a transducer above the upper piston, and an internal load cell measures the force applied to the sample (Figure 3-4a). For these experiments, samples were double jacketed in 0.5 mm thick, heat treated Teflon tubes. Elastic deformation of the rig was corrected using a measured stiffness of 2.5292E8 N/m, and the strength of Teflon was corrected using the data of *Coble et al.* [2014].

Name	P_{f}	Rate Stepping Sequence (µm/s)	P _c (MPa)	T (°C)	Microstructures
ABI	0.357	2.8 - 0.28 - 2.8 - 28 - 2.8 - 0.28	120	150	No
AB2	0.357	2.8 - 0.28 - 2.8	120	150	Yes
AB3	0.7	2.8 - 0.28 - 2.8	120	150	Yes
SMI	0.357	2.8 - 0.28 - 2.8 - 28 - 2.8 - 0.28	120	150	No
SM2	0.357	2.8 - 0.28 - 2.8	120	150	Yes
SM3	0.7	2.8 - 0.28 - 2.8	120	150	Yes

Table 3-1: Experimental conditions. (P_f = Pore Fluid Factor, P_c = Confining pressure, T = Temperature)

Samples of shale and altered basalt were crushed using mortar and pestle for 30 second intervals and were sieved between each interval to remove the <125 μ m fraction. The > 125 μ m fraction was returned to the mortar and pestle and the process was repeated until the sample was completely disaggregated to <125 μ m. Samples were mixed with deionized water to form a thick paste and were applied 2 mm-thick to the forcing blocks. The samples were jacketed, placed in the rig, and had confining and pore fluid pressures applied to them linearly and simultaneously to maintain a constant pore fluid factor. This procedure avoids over-compaction of the sediments.

The experimental setup would then sit at the experimental pore fluid and confining pressures for 8-12 hours while the rig was heated overnight. This time under experimental confining and pore fluid pressures gives the gouge samples time to compact before starting the experiment.

Three sets of experiments were conducted on altered basalt and shale samples (Table 3-1). All experiments were run at a confining pressure of 120 MPa and an internal temperature of 150 °C. These conditions are in the range of estimated deformation temperatures for the Mugi Mélange [*Ikesawa et al.*, 2005] and also reflect the conditions of the plate interface at the NanTroSEIZE Site C0002 [*Harris et al.*, 2011; *Sugihara et al.*, 2014]. All experiments involved rate-stepping between 0.28 and 28 µm/s to evaluate the rate-and-state frictional properties of the samples at *insitu* conditions of deformation (Table 3-1).

Pore fluid factors (0.357 and 0.7) were selected based on estimates of pore fluid pressures from shear wave velocities [*Tonegawa et al.*, 2017] and P-wave velocities [*Kitajima and Saffer*, 2012] from Nankai. Low-velocity zones, which overlap with epicenters for shallow low frequency earthquakes, have estimated pore fluid factors of ~0.7 while elsewhere pore fluid factors range from 0.35 – 0.5 [*Kitajima and Saffer*, 2012; *Tonegawa et al.*, 2017]. Experiments from sets 2 and 3 were used for microstructural analysis (Table 3-1). Experiments are labelled in this paper by sample type and set number (*e.g.* AB2 = Altered basalt, Set 2).

After equilibrating overnight, experiments were initiated with a run-in to a shear displacement between 1.75 and 2.25 mm at a constant rate of 2.8 μ m/s. Once a steady state coefficient of friction was reached, an initial rate-step was applied to the samples, and for experiments from set 1, subsequent rate-steps were applied once the sample appeared to achieve a new steady state (Figure 3-4b). An exception to this was for rate-steps to 28 μ m/s. During these velocity-steps the sample exhibited strain hardening at a faster rate than other rate steps, and did

not achieve a new steady state (Figure 3-4b). As such, rate steps between 2.8 and 28 μ m/s were not used to fit rate-and-state parameters. For experiments from sets 2 and 3, a single set of rate-steps were applied (decrease to 0.28 μ m/s, increase to 28 μ m/s), with 1-2 mm of shear displacement following each step.

3.3.4 Rate-and-State Fitting

Data were fit using an iterative least squares inversion method [Reinen and Weeks, 1993], using a version of the RS3000 code developed for triaxial deformation apparatuses [Skarbek and Savage, 2019]. Individual rate-steps were de-trended using a linear fit to the 300 μ m before the rate-step, and the 400 μ m following each rate-step was used to model the evolution of friction. The evolution of friction (μ) following rate-steps was fit using a single state variable (θ), and both the aging (Dieterich) and slip (Ruina) laws [Dieterich, 1978; Ruina, 1983; Marone, 1998]. Friction is described by

$$\mu = \mu_0 + a \ln \left(\frac{V}{V_0} \right) + b \left(\frac{V_0 \theta}{D_c} \right) \tag{3.1}$$

where V_0 and V are the velocities before and following a rate-step respectively, μ_0 the coefficient of friction before the rate-step, a the magnitude of the instantaneous change in μ following a rate-step, b the magnitude of change in μ during its subsequent evolution back to a new steady state, and D_c the critical slip distance. The state variable (θ) is either described by the aging law [Dieterich, 1978]

$$\frac{d\theta}{dt} = 1 - \frac{V\theta}{D_c} \tag{3.2}$$

or the slip law [Ruina, 1983]

$$\frac{d\theta}{dt} = -\frac{V\theta}{D_c} \ln\left(\frac{V\theta}{D_c}\right). \tag{3.3}$$

Fits for both aging and slip laws were obtained and are reported in Supplementary Table 3-1; however, on plots in this paper only the aging law fits are shown to facilitate comparisons with previous experimental literature on subduction zone materials [e.g. *Saffer and Marone*, 2003; *den Hartog et al.*, 2012a, 2012b; *Zhang et al.*, 2017].

The sawcut geometry of triaxial deformation apparatuses leads to changes in normal stress during velocity steps [Linker and Dieterich, 1992; Perfettini et al., 2001; Hong and Marone, 2005]. These changes in normal stress affect the evolution of friction (the state variable), and can be corrected using the equation derived by [Linker and Dieterich, 1992], where

$$\frac{d\theta}{dt} = -\alpha \frac{\theta}{b\sigma} \frac{d\sigma}{dt} \tag{3.4}$$

and α is a new variable defined by

$$\alpha = \frac{\frac{\Delta \tau}{\sigma}}{\ln\left(\frac{\sigma}{\sigma_0}\right)} \,. \tag{3.5}$$

The right side of equation (4) can be added to the right side of equations (2) or (3) to correct the state variable for the effects of changing normal stress during a velocity test [Hong and Marone, 2005]. The value of α can be determined through normal stress stepping experiments in a biaxial shear apparatus [Linker and Dieterich, 1992; Hong and Marone, 2005], and theoretically may vary from 0 (unaffected by normal stress perturbations) to μ_0 (maximum effect of normal stress perturbations) [Perfettini et al., 2001]. In geologic materials α ranges from ~1/3 to ~1/2 of steady state friction [Hong and Marone, 2005]. We use a value of 0.2 for α , consistent with results for

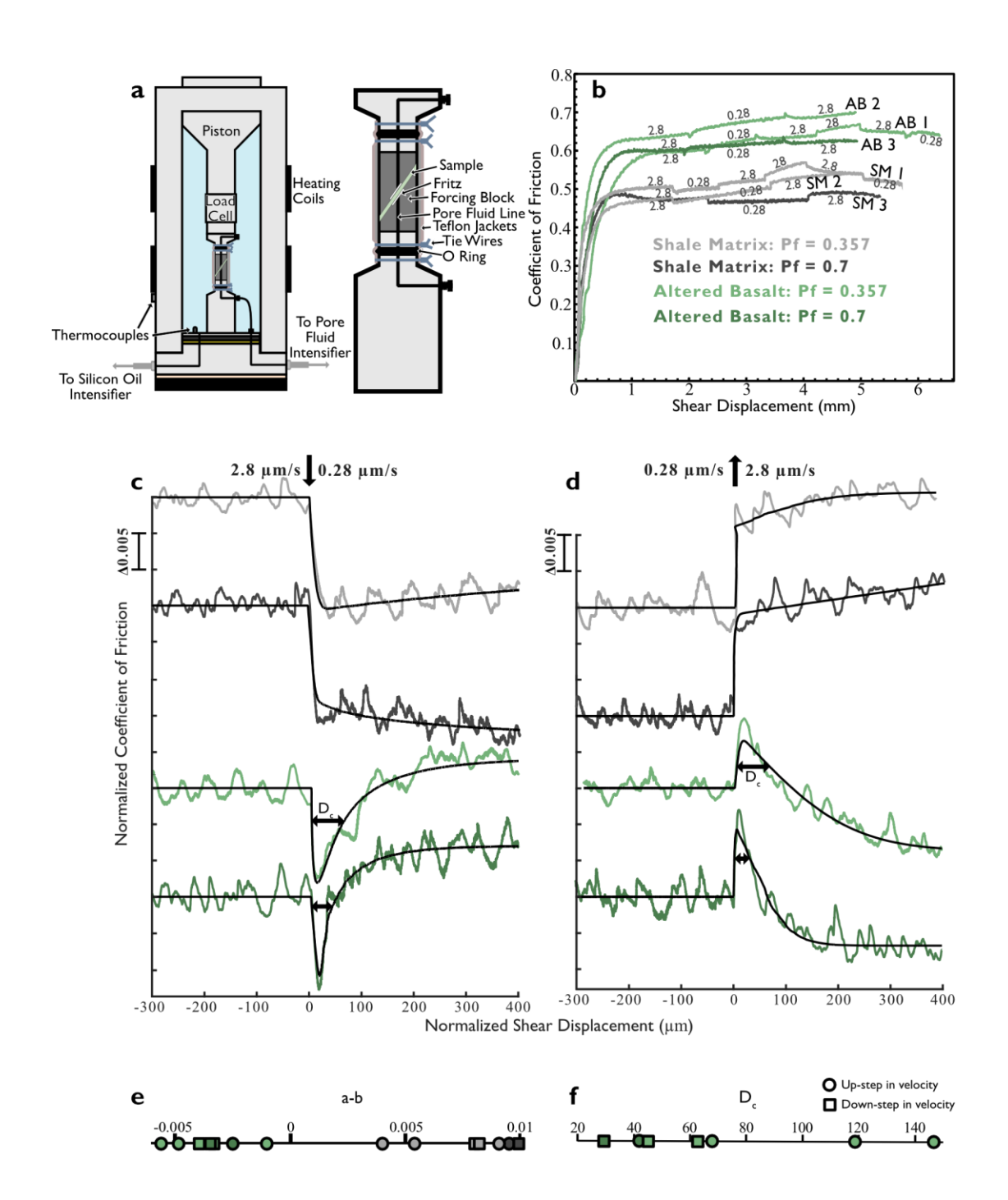


Figure 3-4: Experimental results. a) Schematic of the triaxial apparatus housed at Rice University. b) Results of friction experiments on crushed altered basalt (AB) and shale matrix (SM). Labelled shear velocities are in μ m/s. c) Model results of rate-steps from shear velocities of 0.28 to 2.8 μ m/s and d) for rate-steps from 0.28 to 2.8 μ m/s. Displacements are normalized

so that 0 μm is the location of the rate-steps. Widths of double-headed arrows indicate the modelled critical slip distances (Dc) for altered basalt. e) Fits for a-b from all experiments for rate-steps between 0.28 and 2.8 $\mu m/s$. f) Fits of the critical slip distance for the altered basalt. (Fits for the shale matrix are not included due to the high errors associated with the negligible evolutionary effect).

quartz-phyllosilicate mixtures in biaxial experiments [*Hong and Marone*, 2005], and which is ~1/3-1/2 of our measured friction coefficients.

3.3.5 Microstructures and Grain Size / Shape Analysis

Following shear experiments, the samples were dried, vacuum impregnated with epoxy, cut parallel to the slip direction through the long-axis of the recovered experiment, and drypolished to produce a polished puck. A thin carbon coat was applied to the polished surface for scanning electron microscopy. The SEM was operated in low-vacuum mode to minimize charging effects on the gouges.

Polished thin sections were prepared from the other half of the cut sample for optical microscopy. Using a motorized stage on a petrographic microscope, stitched mosaic photographs of the experimental and natural fault rock samples were produced at 100x magnification using reflected light for grain size and shape analysis. After correcting for shading and stitching, high-quality (resolution of 2.2 pixels / micron) images were exported for image analysis in imageJ. To segregate grains, we applied grey level segmentation (5 levels using the jazy Look-Up-Table macro; [Heilbronner and Keulen, 2006]) to each image based on their histograms. Consistent segmentation was applied to each image. After visually inspecting the segmented images, we thresholded the images, making them binary, and filled holes in individual grains (imageJ "fill holes" command). Cracks and physical holes were manually removed using the fill tool in imageJ.

	EXPERI	MENIA	EXPERIMENTAL SAMPLES	LES									NATUR	NATURAL SAMPLES	MPLES
	AB2-W	AB2-M	AB2-SB	AB3-W	AB3-M	AB3-SB	SM2-W SM2-M	SM2-M	SM2-SB SM3-W SM3-M	SM3-W	SM3-M	SM3-SB	AB-F	AB-B	MS
Area of Grains (%)	17.6	25.5	13.3	20.1	25.7	9.1	10	11	6.8	4.1	5.7	3.8	15.7	25.6	19.2
Area Analyzed (mm^2)	4.01	0.97	2.65	14.51	9.29	4.15	21.09	13.25	6.57	9.99	2.71	6.2	2.23	36.6	11.4
Number of Grains > 10 um	1145	380	602	5024	4019	772	3753	2670	821	800	478	293	799	10325	3026
Number of Grains 3-10 um	4323	1183	2530	16579	12405	3790	16806	12182	4041	3828	2304	1411	4218	41523	18745
D values (Clauset)	1.73	1.86	1.88	1.5	1.46	1.88	2.14	1.95	2.3	2.03	1.91	2.87	3.16	1.55	2.13
xmin	7.9	12.79	8.69	5.23	5.23	5.98	13.24	8.07	9.7	7.19	6.6	19.63	13.15	6	7.67
р	0	0.07	0.08	0	0	0	0	0	0.45	0	0	0.6	0.31	0	0.02
D values with fixed xmin	1.76	1.62	1.89	1.71	1.67	2.07	1.95	1.98	2.07	2.13	2.03	2.18	2.43	1.62	2.16
xmin	9	9	9	9	9	9	9	9	9	9	9	9	9	9	9

Table 3-2: Calculated fractal dimensions (D) of the grain size distributions from the present study for the statistically best lower cutoff (xmin) and for a constant lower cutoff of 9 μ m (see Figure 3-5a). P-values are the results from the goodness-of-fit test. P-values above 0.1 indicate

that a power law distribution is a probable fit to the grain size distributions. Note that only the shear band domains from the shale matrix and the natural altered basalt indicate that the data is well fit by a power law. (M = Matrix, SB = Shear Band, SM = Shale Matrix, AB = Altered Basalt, AB-H = Natural Altered Basalt Host, AB-F = Natural Fault in Altered Basalt).

Examples of pre- and post-processed images are provided in Figure 3-6 (f-g). The Particles8 tool (part of the morphology toolbox) in imageJ was used to analyze particle shapes and orientation [*Landini*, 2008]. Analysis of both whole thin sections of recovered experimental run product and isolated areas of interest (Riedel shears and the matrix between Riedel shears) was performed to compare changes in grain sizes and shapes during deformation. Grain shape analysis was performed on all grains with an equivalent diameter $(2 * \sqrt{area/\pi})$ greater then 10 µm, and for grains between 3 and 10 µm (Table 3-3). Feret angle, solidity, convexity, Paris factor (p-factor), and aspect ratio were analyzed for whole thin sections and isolated areas of interest (for definitions of shape factors see Figure 3-5b) [*Heilbronner and Keulen*, 2006].

Grain size distributions were measured on thin sections cut from each experimentally-deformed sample and for the natural mélange samples (Figure 3-2a). We followed the technique of *Blenkinsop* [1991], where grains are not binned, and the logarithm of total number of grains below a given grain size (divided by area analyzed) is plotted (Figure 3-5a). Fractal dimensions (*D*; the slope of a linear fit to the grain size distributions) were calculated for each grain size distribution. Fits were performed following the methods outlined in *Clauset et al.* [2009] for fitting power laws to empirical data, which uses maximum likelihood rather than least squares regression for establishing the scaling exponent. We used the continuous *Blenkinsop* [1991] method over the other common method where grains are binned [*Sammis et al.*, 1986; *Marone and Scholz*, 1989; *Keulen et al.*, 2007], since binning data has been shown to decrease the accuracy of fits to power law data and to underestimate the value of *D* [*Virkar and Clauset*, 2014]. For each grain size

distribution we determined a lower bound to the fit (x_{min}) using the Kolmogorov-Smirnov goodness-of-fit statistic, outlined in detail in *Clauset et al.* [2009]. However, because of the wide range in values of x_{min} determined for each grain size distribution, we performed a second fit with a constant x_{min} of 9 μ m (the average x_{min} of the samples as determined by the Kolmogorov-Smirnov goodness-of-fit statistic) to facilitate direct comparison of values determined in this study. The D values determined through these methods are larger than those determined through least squares regression. We calculated fits using least squares regression to see the effect (Figure B4 and Table B2), and found that that the fractal dimensions are ~ 0.3 to 0.5 higher for the fits determined using maximum likelihood. Finally, a goodness of fit test (P-value, where synthetic data sets with identical D and x_{min} are compared with the natural data) was used to determine the likelihood that the grain size distributions indeed follow a power-law distribution (Table 3-2) [Clauset et al., 2009]. We note that most of the samples here show a poor likelihood of being best described by a power law, however, we use the power law framework to facilitate comparison with previous studies on grain size distributions.

3.4 Results

3.4.1 X-Ray Diffraction

Analysis of random powders shows that the altered basalt is predominantly composed of albite and chamosite (chlorite), while the shale is composed of quartz, illite, and albite (Figure 3-3). The total proportion of phyllosilicates is ~25 and ~40 % for the altered basalt and shale samples respectively (Figure 3-3a-b). In the oriented clay separates, neither unit shows evidence for expanding clays (i.e. smectites; Figure 3-3c-d).

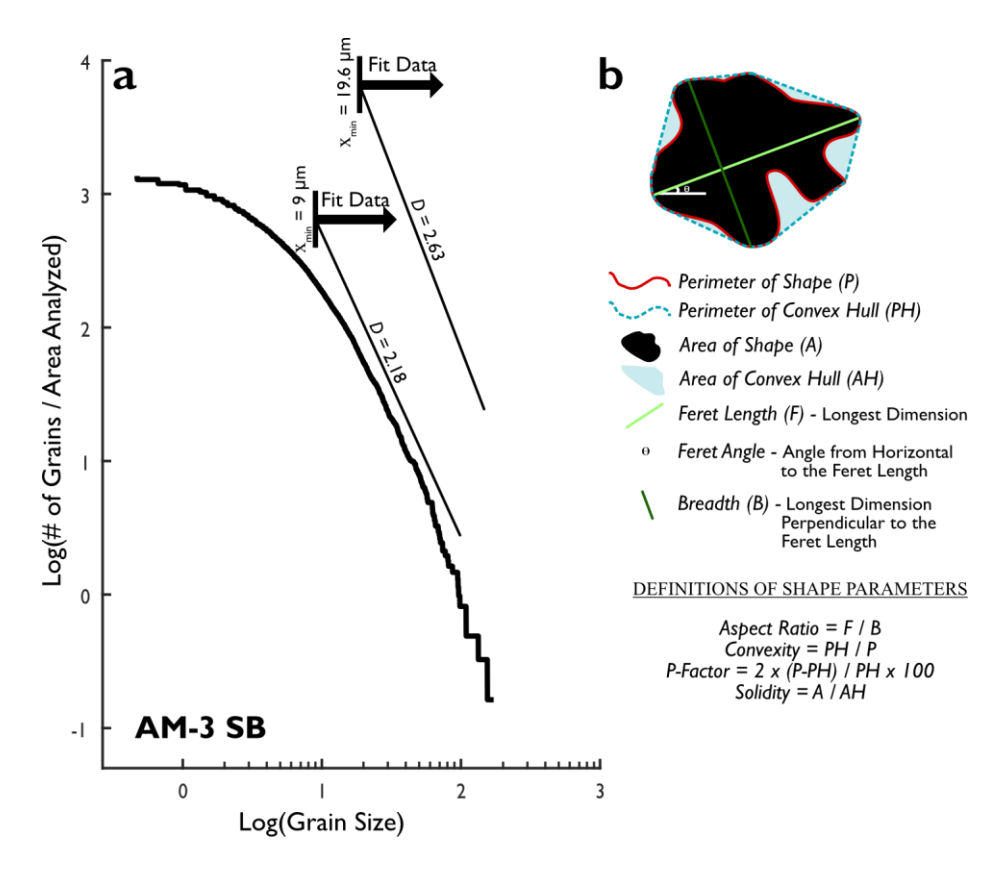


Figure 3-5: a) Methods used for determining grain size distributions, using either a lower cut-off that provides the best fit to the data (in this case xmin = $19.6 \mu m$), or using a consistent lower cut-off of 9 μm . All fits are reported in Table 3-2. b) Definitions of the grain shape parameters used in this study for a given shape (black object).

3.4.2 Rate-and-State Friction Parameters

Shale was frictionally weaker ($\mu o = 0.47\text{-}0.54$) than the altered basalt ($\mu o = 0.60\text{-}0.65$) in all experiments (Figure 3-4b; Table B1). All experiments with a pore fluid factor of 0.357 show strain hardening through the experiment, while those at a pore fluid factor of 0.7 do not (Figure 3-4b). Altering the pore fluid factor had little effect on the coefficient of friction at the start of experiments, though the lower degree of strain hardening through the experiment led to a lower coefficient of friction by the end of experiments with elevated fluid pressures. Fits for a, b, and Dc to each rate-step between 0.28 and 2.8 μ m/s are shown in Figure 3-4e-f and Table B1. The shale

	Convexity		Solidity		Aspect Ratio		P-Value	
>10 microns	Mean	Median	Mean	Median	Mean	Median	Mean	Median
SM	0.66	0.66	0.64	0.63	1.66	1.52	128	101
SM2-M	0.80	0.82	0.77	0.80	1.72	1.58	58	42
SM2-SB	0.82	0.86	0.80	0.83	1.74	1.54	50	33
SM3-M	0.79	0.81	0.74	0.76	1.82	1.66	62	46
SM3-SB	0.80	0.83	0.76	0.79	1.73	1.56	58	40
АВ-Н	0.71	0.72	0.68	0.68	1.63	1.53	100	77
AB-F	0.73	0.74	0.68	0.69	1.59	1.49	86	70
AB2-M	0.76	0.78	0.78	0.78	1.62	1.52	73	56
AB2-SB	0.77	0.80	0.79	0.82	1.58	1.50	68	51
AB3-M	0.77	0.79	0.77	0.79	1.62	1.51	70	53
AB3-SB	0.80	0.83	0.81	0.83	1.52	1.43	57	42
3-10 microns								
SM	0.86	0.88	0.73	0.75	1.68	1.57	35	26
SM2-M	0.92	0.94	0.83	0.88	1.80	1.64	18	12
SM2-SB	0.93	0.95	0.86	0.90	1.76	1.58	16	10
SM3-M	0.92	0.95	0.83	0.87	1.91	1.72	18	12
SM3-SB	0.93	0.95	0.83	0.87	1.88	1.69	17	11
АВ-Н	0.88	0.90	0.75	0.78	1.69	1.58	31	22
AB-F	0.87	0.90	0.75	0.77	1.68	1.56	32	23
AB2-M	0.91	0.94	0.83	0.86	1.71	1.58	21	14
AB2-SB	0.91	0.94	0.83	0.87	1.63	1.50	21	13
AB3-M	0.92	0.94	0.84	0.88	1.66	1.54	19	12
AB3-SB	0.92	0.95	0.85	0.89	1.60	1.48	18	11

Table 3-3: Mean and median values for shape factors. (M = Matrix, SB = Shear Band, SM = Shale Matrix, AB = Altered Basalt, AB-H = Natural Altered Basalt Host, AB-F = Natural Fault in Altered Basalt)

exhibits velocity-strengthening behavior with a negligible evolutionary effect (b), while the altered basalt exhibits velocity-weakening behavior (Figure 3-4c-d). At elevated pore fluid factors, Dc decreases for the altered basalt (Figure 3-4c-e). This change is not observable in the shale due to the negligible evolutionary effect (Figure 3-4c-d).

3.4.3 Microstructures of Experimentally-Deformed Samples

Deformation in the experiments was predominantly accommodated in localized Riedel shears. The shears are a few hundred microns wide (variable) and locally anastomose, but generally occur in a Y-orientation (parallel with the imposed slip direction) [Logan et al., 1979, 1992]. Riedel shears can be identified by a greatly reduced grain size, and appear dark in both cross polarized and reflected light (Figures 6 a,b,h,i and 7 a,b,f,g). The Y-shears occur near the contact with the forcing blocks (Figures 6a, 7f), as is commonly observed in triaxial friction experiments [e.g. Logan et al., 1992; Tembe et al., 2010]. R-shears developed in several experiments and are visible in thin sections from experiments with better recovery (SM2 & AB3). R-shears allowed the principal Y-shear to be transferred from the margin of one forcing block to the forcing block on the other side (Figures 6a, 7f). In shale experiment SM2, Riedel-shears have strongly aligned phyllosilicates, as seen by the uniform color in cross polarized light photomicrographs with the lambda plate inserted (Figure 3-6a,h). In contrast, Riedel-shears in the altered basalt samples show a poor alignment of phyllosilicates (Figure 3-7). The shale experiment at high pore fluid pressure (SM3) is an exception to the above description, and does not show localized shear surfaces in Yand R-orientations. Instead it displays a well-developed P-fabric, and distributed deformation across the width of the sample (Figure 3-6h).

The orientation of clasts (>10 μ m) changes between the matrix and shear band domains (Figures 6g,l and 7e,j). In the matrix of altered basalt samples, clasts have long axes aligned parallel to the principal stress (i.e. parallel to the long axis of the forcing blocks). Backscattered SEM images of the experimentally sheared samples show that tensile fractures in large grains from the altered basalt are predominantly oriented parallel to the maximum principal stress (σ 1) (~35°; Figures S1, S2). In the shale samples, fracturing of large grains occurs parallel with the pre-existing

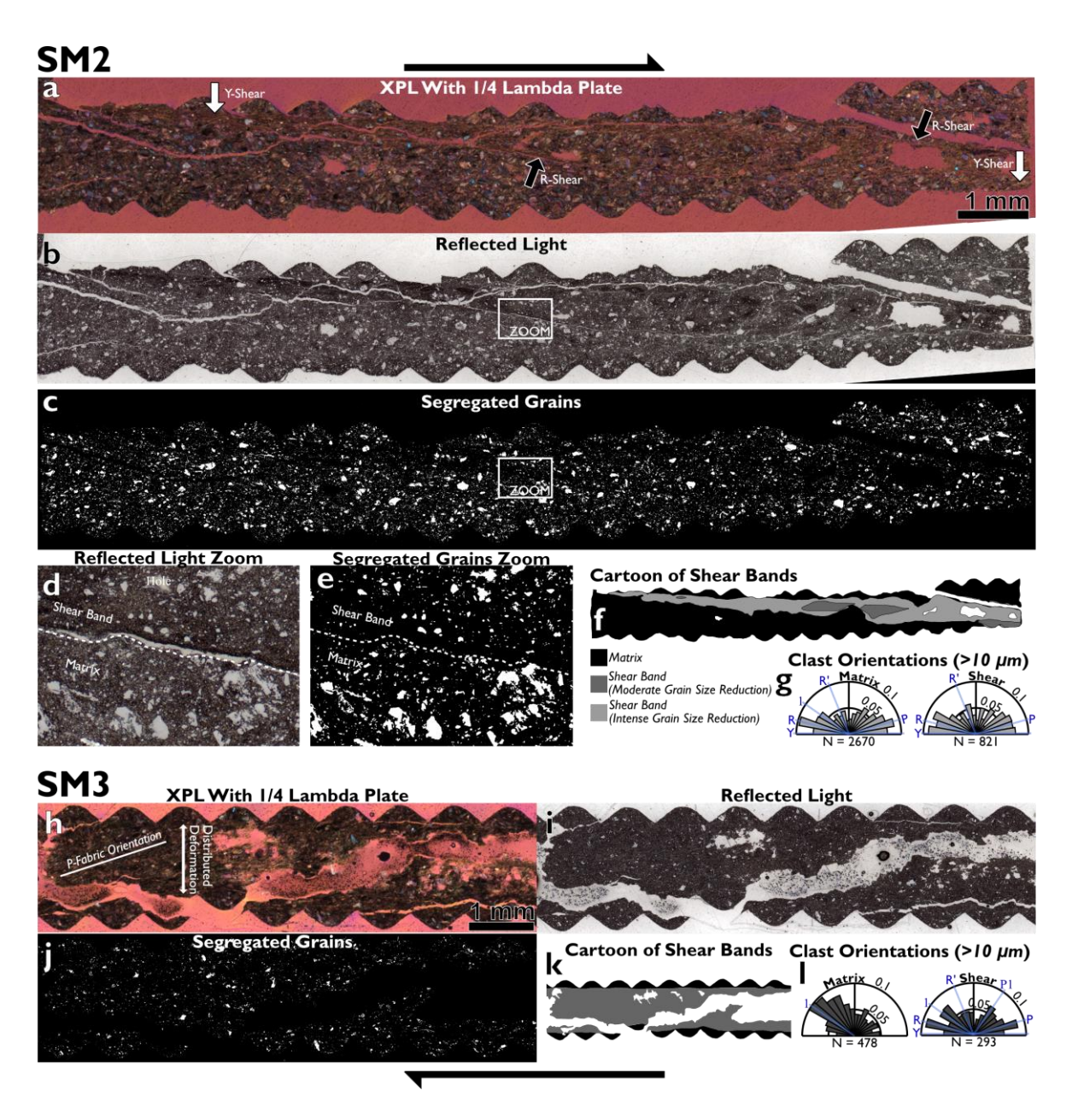


Figure 3-6: a-b & h-i) Photomosaics of the experimentally sheared shale samples in cross-polarized light with a ¼ lambda plate (a,h) and reflected light (b,i). c,j) Segregated grains from the reflected light image used for grain shape and size analysis. d-e) Zoom of the reflected light image (d) and the segregated grains (e). Note the decrease in grain size within the shear band domain. f,k) Cartoons of the microstructural domains. g,l) Clast orientations (Feret angle) of the matrix (black from cartoons) and shear bands (greys from cartoons) for experiments on shale matrix. Clast orientations are plotted as probability density functions. Average Riedel shear

orientations from *Logan* [1992] are labelled (R, P, Y, and R'), as well as the orientation of the principal stress (1) and the orientation perpendicular to it (P1) where appropriate.

foliation within clasts (Figure B1). From these samples the predominant orientation of tensile fractures is ~60° from the shear direction. The majority of tensile fractures from both units are observed in large clasts within the matrix between localized Riedel shears (Figure B1). In the shear band domain, clast orientations are similar to the macroscopic Riedel shears observed in samples. In shear band domains from all experiments, clasts show a strong alignment in R- and P-orientations, and moderate to strong alignment in the Y- orientation (Figures 6g,l and 7e,j). In the sample showing distributed deformation (SM3), there is an alignment of grains perpendicular to the principal stress orientation (Figure 3-6l).

Grain shape factors changed systematically from matrix to shear band domains, with an increase in convexity and solidity, and a decrease in aspect ratio and P-value (Table 3-3). The percent change of each shape factor was greater for grains larger than 10 µm than for those between 3 – 10 µm (Table 3-3). As in previous studies, grain size distributions showed an increase in the value of D between matrix and shear bands, and a direct correlation between D-value and percent-clasts (Figure 3-8b; Table 3-2) [Heilbronner and Keulen, 2006; Keulen et al., 2007]. Altered basalt showed a progression from D-values of ~1.6 in the matrix to D-values of 1.9-2.1 in the shear bands, while all shale matrix D-values fell between 1.9 and 2.1 (Figure 3-8b).

3.4.4 Microstructures of Natural Samples

Grain sizes and shapes were analyzed for the natural shale matrix, the altered basalt, and a fault cutting through the altered basalt from Figure 3-2. The grain size distribution from the natural shale matrix shows a moderate D-value (~2.1) (Figure 3-8b). A strong shape preferred orientation of clasts exists in the shale matrix parallel with the principal foliation observed in thin section

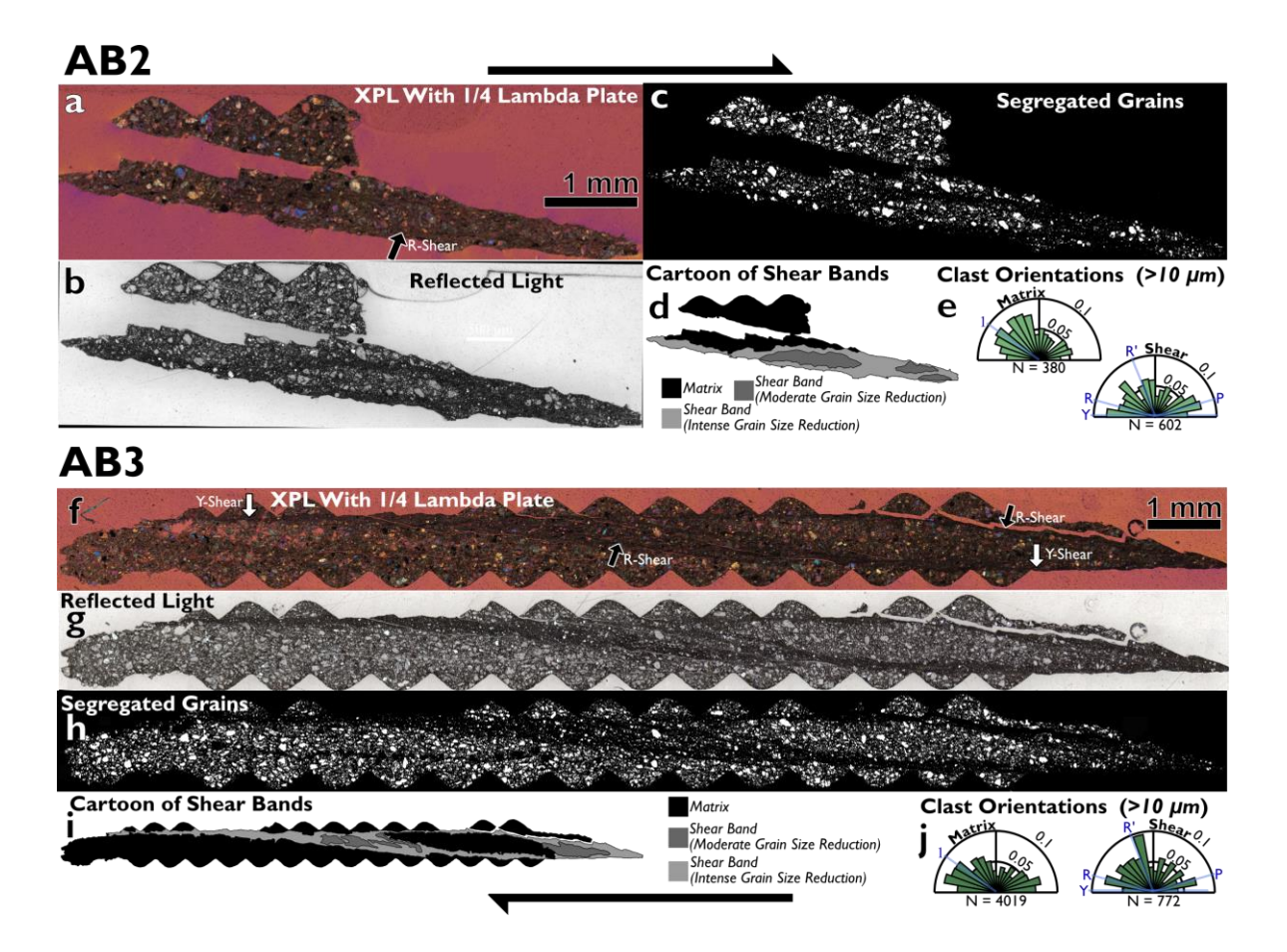


Figure 3-7: a-b & f-g) Photomosaics of experimentally sheared altered basalt in cross-polarized (a,f) and reflected light (b,g). Note that AB2 had poor recovery relative to other experiments. c,h) Segregated grains from the reflected light image used for grain shape and size analysis. d,i) Cartoons of the microstructural domains. e,j) Clast orientations of the matrix (black) and shear bands (greys) for experiments on altered basalt. Clast orientations (Feret angle) are plotted as probability density functions. Average Riedel shear orientations from *Logan* [1992] are labelled (R, P, Y, and R'), as well as the orientation of the principal stress (1) where appropriate.

(Figure 3-2b). The natural shale displays the lowest solidity and convexity values of any sample, the lowest aspect ratio of any shale sample, and a higher P-factor than any experimentally-sheared shale sample (Table 3-3).

The altered basalt shows no shape preferred orientation, while the fault cutting through the altered basalt shows a shape preferred orientation in R- and P-Riedel orientations (Figure 3-2b).

Convexity and solidity values are lower than the experimentally deformed altered basalt, and there is a slight increase in these values from the host altered basalt to the fault cutting through the altered basalt (Table 3-3). The naturally faulted samples show a larger proportion of smaller grains per unit area (<10 µm) than the experimental samples (Figure 3-8a). The D value for the altered basalt host is comparable to the matrix between shear bands in the experimental samples (Figure 3-8b). However, the natural fault cutting through the altered basalt shows a higher fractal dimension (D) than experimental faults, while maintaining a higher percentage of clasts than the experimental shear bands (Figure 3-8b).

3.5 Interpretations

3.5.1 Interpretation of Experimental Results and Microstructures

The difference in coefficient of friction between the altered basalt and shale may be explained by the relative phyllosilicate abundances of the two samples. The shale contains a larger proportion of phyllosilicates (~40%) compared with the altered basalt (~25%). Mixtures of framework silicates and phyllosilicates often show a linear relationship between phyllosilicate content and coefficient of friction at low temperatures [*Tembe et al.*, 2010 and refs within]. Given that the coefficient of friction for both albite and quartz (the dominant framework silicate in each sample) is about ~0.7 [*Chester and Higgs*, 1992; *He et al.*, 2013], and that the coefficient of friction for wet illite and chlorite at low temperatures is ~0.3 [*Behnsen and Faulkner*, 2012], the obtained coefficients of friction (μ = ~0.65 for altered basalt and ~0.5 for shale) are in agreement with the predictions of Tembe *et al.* [2010] for quartz-illite mixtures (Figure 3-4; their figure 4b).

The rate-and-state properties of the shale matrix are comparable to previous experiments on illite-rich shales at low to moderate temperatures [Saffer and Marone, 2003; Ikari et al., 2009; den Hartog et al., 2012b], which all show velocity-strengthening behavior at temperatures below

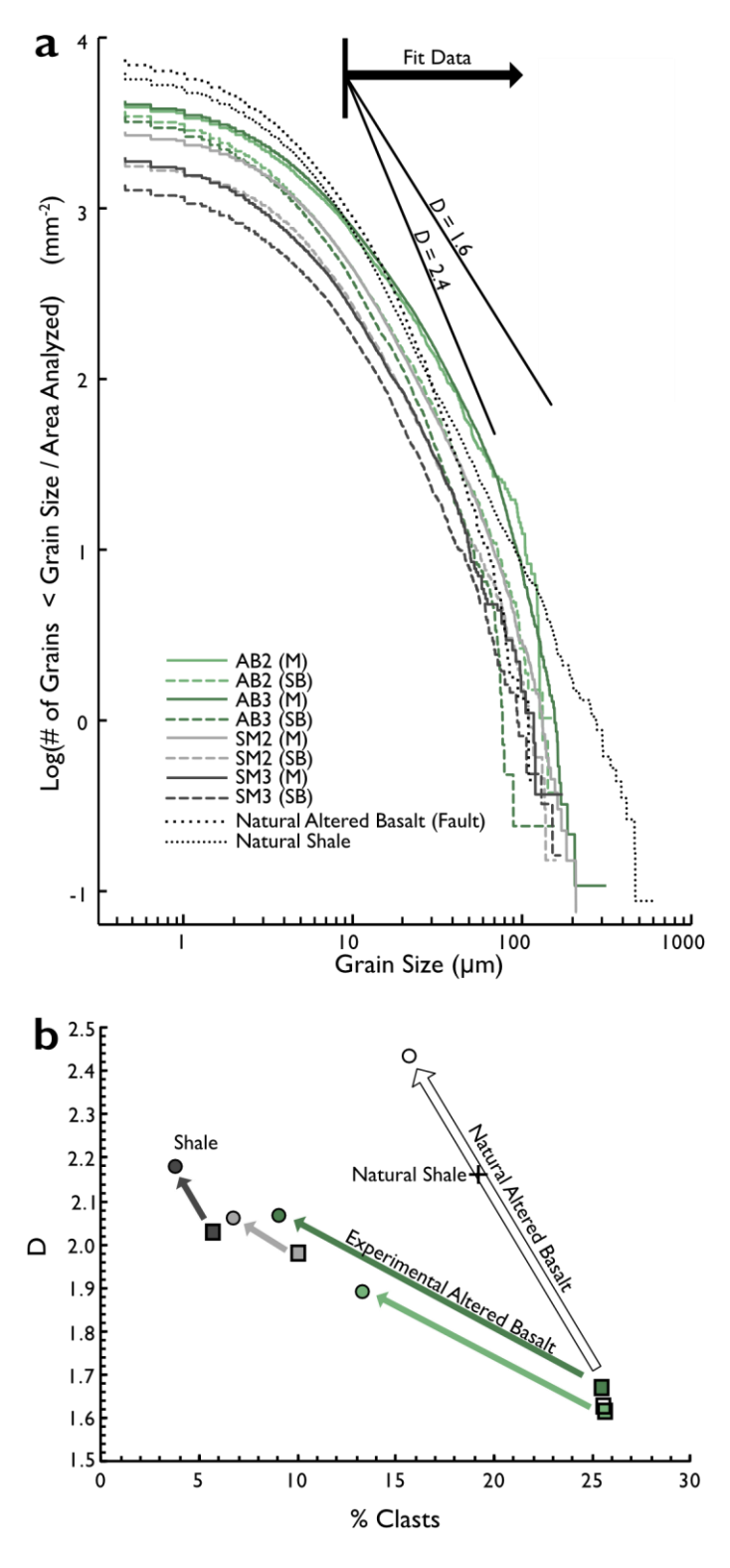


Figure 3-8: a) Grain size distributions for the experimental run products and the natural microstructures using the approach of *Blenkinsop* [1991]. The fit interval (> 9 μ m) is used in the calculation of the fractal dimension, *D*. Solid black lines show the range of slopes for the

calculated values of D. b) Evolution of the grain size distribution from the matrix (squares) to shear bands (circles) for each of the experiments (using a consistent x_{min} of 9 μ m). For the natural altered basalt, the evolution from the host to the fault is shown.

250 °C (Figure 3-9). The velocity-weakening behavior of altered basalt, however, does not follow the observations of frictional behaviour of fresh basalt [*Zhang et al.*, 2017] or fresh gabbro [*He et al.*, 2007], which both show velocity-strengthening behavior at temperatures below 250 °C (Figure 3-9). The alteration of basalt at Mugi led to an increase in albite at the expense of pyroxene (~10% change in each, Figure B5). Pyroxene is approximately velocity neutral while albite is velocity weakening [*He et al.*, 2013]. The replacement of pyroxene by plagioclase may therefore push altered basalt into the velocity-weakening regime [*He et al.*, 2013].

The microstructures from our experimentally sheared samples may provide insights into the rate-and-state properties of the two rock types that are representative of the Mugi Mélange. A major difference between the altered basalt and the shale matrix is in the evolution of friction following a rate-step (*b*), which has long been thought to reflect the evolution of asperity contact areas and strengths (through chemical and physical time-dependent processes) following a rate-step [*Rabinowicz*, 1951, 1958]. The lack of an evolution in friction following a rate-step (i.e. negligible to negative *b* value) in the shale may be due to the aligned phyllosilicates observed in the photomicrographs of the deformed shale (Figure 3-6a,h). Slip parallel to aligned phyllosilicates would not change contact area during slip following a rate-step, and would therefore not show an evolution of friction during subsequent slip [*Ikari et al.*, 2013]. This has been observed previously in biaxial experiments on phyllosilicate-rich rocks, including illite schists, chloritic schists, and montmorillonite-quartz mixtures [*Ikari et al.*, 2009] as well as smectite-rich samples [*Saffer and*

Marone, 2003; *Carpenter et al.*, 2015], and our results show the same behavior at 150° as documented in these earlier room-temperature experiments (Figure 3-4b-d).

Increasing the pore fluid factor was found to decrease the critical slip distance (D_c) for experiments on altered basalts, as has been previously observed in calcareous gouges [Figure 3-4f; *Scuderi and Collettini*, 2016]. This is interpreted to be due to the decreased effective normal stress on the system, which would reduce contact area at the grain junctions for the altered basalt, and allow for faster equilibration of grain contacts following a rate-step [*Scuderi and Collettini*, 2016].

We note that the strengths and velocity dependence of the materials determined in this study may change at plate-rate velocities, where low temperature crystal plasticity of the phyllosilicates [French et al., 2015] and/or pressure solution in quartz [den Hartog and Spiers, 2014; Fagereng and den Hartog, 2016; Phillips and White, 2017] may become important mechanisms that affect the frictional properties. However, the experimental conditions are likely similar to those in subduction plate boundaries, and at these slip rates are expected to be applicable to the slip rates during earthquake nucleation and for slow slip.

3.5.2 Comparison of the Natural and Experimental Microstructures

The shape factors of the natural shale samples from the mélange matrix differentiate it from the experimental samples which were ground to <125 µm grainsize prior to shearing (Table 3-3). Despite a lower aspect ratio than the experimental samples, the shape factors for the natural shale show less rounding than the experimental samples, and a strong shape preferred orientation parallel with the foliation observed in plane polarized light. This contrasts with the shear bands formed during the experiments, which show a greater roundness of grains with lower aspect ratios, and a

shape preferred orientation of grains parallel to R- and P-Riedel shears. This difference reflects the dominance of solution processes in developing the natural shale fabrics, which cannot effectively create fabric on short laboratory time scales. Previous geochemical studies of the Mugi mélange support the importance of solution in the shale matrix [*Kawabata et al.*, 2007, 2009].

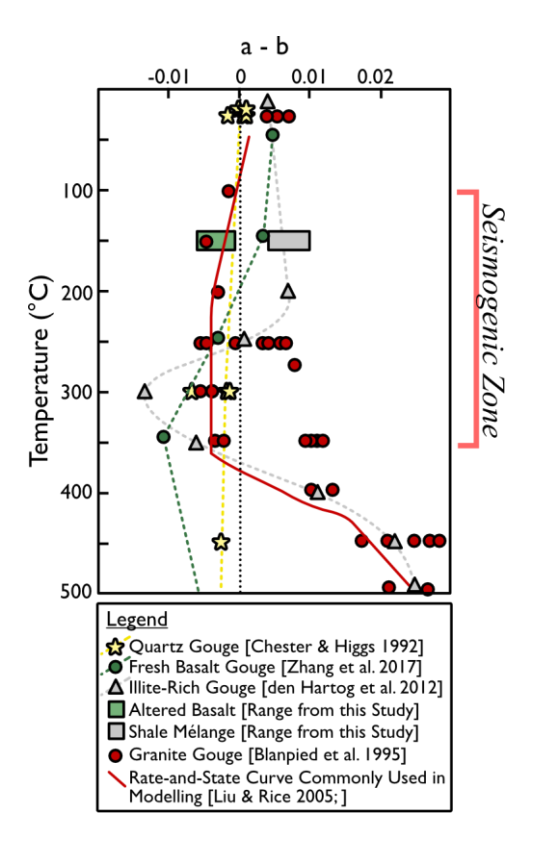


Figure 3-9: Velocity dependence of friction with temperature used in models and for some common subduction zone lithologies. Many modelling studies use the results of *Blanpied et al*. [1995; solid red line], derived from experiments on granite (red circles), while results from more realistic subduction zone materials (illite gouge and basalt) tend to shift velocity-weakening behavior to greater depths than the observed seismogenic zone (demarcation of thermally defined seismogenic zone based on *Hyndman et al*. [1997]). Note that illite-rich gouge, shale mélange from this study, and basalt all show velocity-strengthening behaviour at the updip limit of the seismogenic zone, while the altered basalt from this study exhibits velocity-weakening behavior.

In the natural altered basalt, we see a progression in grain size distributions and shape factors from the host to the fault that are similar to the changes from the matrix to the shear bands in experiments. The fractal dimension of the grain size distribution increases and there is a change in shape factors indicating greater roundness of grains (Tables 3-2, 3-3). Clast orientations show a shape preferred orientation parallel to Riedel shears (Figure 3-2b). These observations indicate that the faults in the altered basalt formed through cataclasis and frictional sliding. One notable difference between the fault in the natural altered basalt and the experimental shear bands is in the proportion of clasts. The natural fault has a higher proportion of clasts compared to the shear bands in experiments. This may be due to post-fracturing grain growth [Sammis and Ben-Zion, 2008], precipitation of minerals from fluids in the fault following slip (e.g. fault healing; [Williams et al., 2015]) and/or agglomeration of grains.

The natural microstructures indicate that distributed deformation in the shale was accommodated through pressure solution-accommodated creep, while the altered basalt deformed through localized cataclasis and frictional sliding. In the experiments, both rock types deformed through cataclasis and frictional sliding.

3.6 Discussion

Unstable slip is expected to occur in materials with velocity-weakening behavior [*Scholz*, 1998]. Seismic features in the Mugi Mélange have been found along the margins of altered basalts [*Ujiie et al.*, 2007a; *Phillips et al.*, 2019] and quartz-rich turbidites [*Ujiie et al.*, 2007b]. Both of these units exhibit velocity-weakening behaviour at moderate slip rates in the lab (~0.1-100 μm/s) [This study; *Chester and Higgs*, 1992], rates which are thought to be important for earthquake nucleation [*Dieterich*, 1992]. Earthquake propagation into velocity-strengthening materials, like the shale matrix, has been shown to be possible in models [*Noda and Lapusta*, 2013] so long as

the frictional resistance to achieve dynamic weakening at earthquake slip rates is overcome [*Ujiie* et al., 2009; Di Toro et al., 2011; French et al., 2014]. However, field evidence for the propagation of large seismic events into velocity-strengthening matrix remains elusive from exhumed subduction zones at shallow depths like the Mugi Mélange. Within mélanges exhumed from slightly greater depths like the Ghost Rocks Mélange (\sim 12-14 km, T = \sim 250 °C) and the Okitsu Mélange ($T = \sim 250$ °C), pseudotachylytes and fluidized cataclasites are found cutting through the shale mélange matrix [Ikesawa et al., 2003; Rowe et al., 2005]. This is consistent with the transition from velocity-strengthening to velocity-weakening behaviour with increasing temperature for illite-rich samples determined in experiments (Figure 3-9) [Moore et al., 1989; den Hartog et al., 2012a, 2012b]. This transition occurs in fresh basalt and illite-rich shales between 200 and 250 °C (Figure 3-9). We have shown that altered basalt is velocity weakening at shallower conditions than this transition, and may serve as a unit where earthquake nucleation and propagation are favored at shallow depths along the subduction interface. At the Ghost Rocks Mélange, pseudotachylytes were searched for extensively through other units, including basalt, but were not found. This may indicate that in deeper environments, where most materials are velocity weakening, basalt is not a unit where preferential nucleation or propagation occurs.

Mixing velocity-weakening and strengthening materials is one proposed mechanism for tremor (composed of very low and low frequency events). Within these models, failure of blocks of velocity-weakening materials embedded within a velocity-strengthening matrix leads to very low frequency earthquakes or low frequency earthquakes, which together make a tremor-like signal [Ando et al., 2010; Skarbek et al., 2012; Hayman and Lavier, 2014]. At the downdip limit of the seismogenic zone, these are often envisaged as strong, competent, blocks sitting within a ductile matrix deforming through crystal plastic creep [Hayman and Lavier, 2014; Kotowski and

Behr, 2019] or pressure solution creep [Fagereng and den Hartog, 2016]. At the updip limit of the seismogenic zone the matrix accommodates distributed deformation through pressure solution creep and/or distributed frictional sliding [Moore and Saffer, 2001]. In either case, a fracture propagating from a velocity-weakening block (of appropriate size, see below) should be quickly arrested by the velocity-strengthening behaviour of the shale, which could lead to a low frequency or very low frequency event. Basaltic blocks, with velocity-weakening altered margins, could serve as nucleation points for very-low frequency and low frequency earthquakes if they are embedded within a velocity-strengthening matrix (Figure 3-10). Given that shale matrix transitions to velocity-weakening behavior at temperatures above ~250°C, this limits the zone of mixed velocity-weakening and strengthening materials to shallow depths along the subduction interface, consistent with the observation that shallow slow earthquakes and associated tremor occur below ~230°C [Saffer and Wallace, 2015]. It is important to note that the temperature of the transition (from velocity-strengthening to weakening) would change depending on the composition of the matrix. For example, at the Hikurangi margin, where fossiliferous, calcareous oozes mixed with silty clays form the dominant subducting sediments above the oceanic plate, the carbonate dominated matrix may exhibit velocity-strengthening behavior to greater depths than an illite-rich shale matrix [Rabinowitz et al., 2018]. In addition, high pore fluid factors are likely required for low frequency events and slow slip. These are observed in regions of tremor and slow slip in shallow subduction zones [Tonegawa et al., 2017], and are often required in models of tremor using mixed lithologies [e.g. Skarbek et al., 2012].

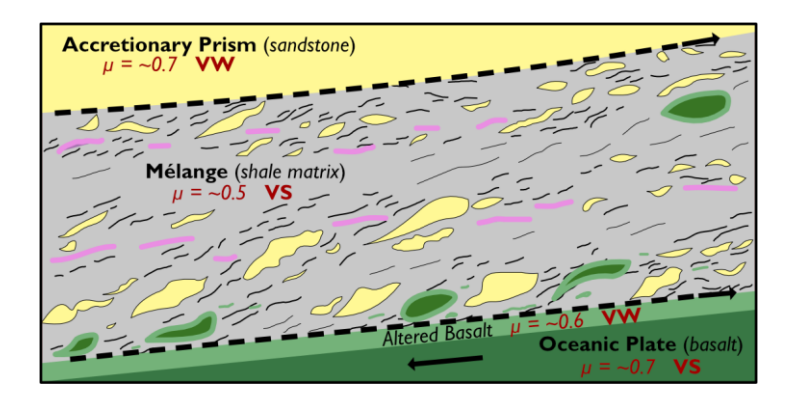


Figure 3-10: Cartoon of the shallow subduction interface based on the geology of the Mugi Mélange (before thrust imbrication). The shale mélange, which shows velocity-strengthening (VS) behaviour is unlikely to nucleate earthquakes, while the altered basalt and sandstone interfaces show velocity-weakening (VW) behavior and may promote localized deformation. Once nucleated, earthquakes may preferentially propagate along the interface between the mélange and altered basalt, or mélange and sandstone layers (dashed black lines). Basaltic blocks with altered margins embedded within the shale matrix may be nucleation sites for (very-)low frequency earthquakes at high pore fluid pressures, or repeating microseismic events at low pore fluid pressures. Thin black lines exhibit the foliation, while pink lines are discontinuous tuffs.

In the experiments presented here, elevating the pore fluid factor had two key effects: 1) it led to a decrease in the critical slip distance in the altered basalt, and 2) it decreased the effective normal stress (σ_n) on the sample. These changes would affect the critical nucleation length required for unstable slip [*Uenishi and Rice*, 2003; *Rubin and Ampuero*, 2005]. The critical nucleation length (L) is described by

$$L = 2 * C * (\mu' * \frac{D_c}{b\sigma_n})$$

where μ' is the shear modulus and C is a numerical constant (with a value between 1 and 1.5). Note that increasing the pore fluid pressure introduces competing effects on the critical nucleation length by decreasing D_c (thereby decreasing L) and also decreasing the effective normal stress (thereby increasing L). The final effect on the critical nucleation length (whether it increases or decreases), would depend on the relative changes of these two properties with increasing pore fluid pressure. If we compare results from the up-steps in velocities from experiments AB2 (Pf = 0.357) and AB3 (Pf = 0.7), we find that increasing the fluid pressure would increase the critical nucleation length for unstable slip by ~1.5 times. The experiments performed here indicate that the reduction in normal stress from increasing the pore fluid pressure has a greater effect on the critical nucleation length than the reduction in critical slip distance.

In models of slow slip, a critical factor controlling slip style (slow slip vs earthquake) is the ratio between the width (W) of the source zone and the critical nucleation length (i.e. W/L) [Liu and Rice, 2007; Rubin, 2008], with large values promoting unstable slip and moderate values promoting aseismic transients with low frequency earthquakes. If we consider blocks of altered basalt as potential nucleation sites (of fixed width) for unstable slip, increasing the pore fluid pressure on the system would decrease the ratio (W/L), promoting aseismic transients with low frequency earthquakes.

Our results extend to the layer of altered basalt along the upper interface of all subducting oceanic plates. The layer of altered basalt at the upper interface of subducting oceanic plates may influence seismicity in two ways. Firstly, it may provide a semi-continuous velocity-weakening interface for seismic events to nucleate from and propagate along. Secondly, while the subducting sediments are velocity-strengthening (at low temperatures), the altered basalt may provide a source of velocity-weakening materials to mix with the subducting sediments, resulting in complex

behavior (tremor, very low frequency events, and low frequency events) at high pore fluid pressure conditions (Figure 3-10).

3.7 Conclusions

The frictional properties of subducting materials likely controls the mode of slip in shallow subduction zones. Altered basalt, a ubiquitous subduction zone material, exhibits velocity-weakening behaviour in the environment of shallow slow slip and tremor, while previous experiments on basalt and gabbro show velocity-strengthening behaviour. This is consistent with field observations of localized faults and paleo-earthquakes hosted in altered basalts from the Mugi mélange. We hypothesize that altered basalt provides a semi-continuous pathway for earthquake nucleation and propagation in subduction zones, and that mixing of altered basalt and velocity-strengthening sediments above the plate interface may lead to complex modes of deformation (tremor, very low frequency events, and low frequency events) at the updip limit of the seismogenic zone.

3.8 Acknowledgements

N.J.P. was supported by a Graduate Mobility Award from McGill University, GSA Student Grant 11283-16, the Japan Society for the Promotion of Science KAKENHI grant JP16K21728, and an NSERC PGS-D, C.R. by an NSERC Discovery Grant and Canada Research Chair in Earthquake Geology, and K.U. by the Japan Society for the Promotion of Science KAKENHI grant JP16H06476.

3.9 References

Ando, R., R. Nakata, and T. Hori (2010), A slip pulse model with fault heterogeneity for low - frequency earthquakes and tremor along plate interfaces, *Geophys. Res. Lett.*, *37*(L10310), 1–5, doi:10.1029/2010GL043056.

- Araki, E., D. M. Saffer, A. J. Kopf, L. M. Wallace, T. Kimura, Y. Machida, S. Ide, E. Davis, and IODP Expedition 365 Shipboard Scientists (2017), Recurring and triggered slow-slip events near the trench at the Nankai Trough subduction megathrust, *Science* (80-.)., 356, 1157–1160.
- Avouac, J. (2015), From Geodetic Imaging of Seismic and Aseismic Fault Slip to Dynamic Modeling of the Seismic Cycle, *Annu. Rev. Earth Planet. Sci.*, 43, 233–271, doi:10.1146/annurey-earth-060614-105302.
- Behnsen, J., and D. R. Faulkner (2012), The effect of mineralogy and effective normal stress on frictional strength of sheet silicates, *J. Struct. Geol.*, 42, 49–61, doi:10.1016/j.jsg.2012.06.015.
- Beroza, G. C., and S. Ide (2011), Slow Earthquakes and Nonvolcanic Tremor, *Annu. Rev. Earth Planet. Sci.*, 39(1), 271–296, doi:10.1146/annurev-earth-040809-152531.
- Bilek, S. L., and T. Lay (1999), Rigidity variations with depth along interplate megathrust faults in subduction zones Rigidity variations with depth along interplate megathrust faults in subduction zones, *Nature*, 400, 443–446, doi:10.1038/22739.
- Blenkinsop, T. G. (1991), Cataclasis and processes of particle size reduction, *Pure Appl. Geophys.*, 136(1), 59–86, doi:10.1007/BF00878888.
- Bürgmann, R. (2018), The geophysics, geology and mechanics of slow fault slip, *Earth Planet*. *Sci. Lett.*, 495, 112–134, doi:10.1016/j.epsl.2018.04.062.
- Carpenter, B. M., D. M. Saffer, and C. Marone (2015), Frictional properties of the active San Andreas Fault at SAFOD: Implications for fault strength and slip behavior, *J. Geophys. Res. Solid Earth*, *120*, 1–17, doi:10.1002/2015JB011963.Received.
- Chester, F. M., and N. G. Higgs (1992), Multimechanism Friction Constitutive Model for Ultrafine Quartz Gouge at Hypocentral Conditions, *J. Geophys. Res.*, 97(B2), 1859–1870.
- Clauset, A., C. R. Shalizi, and M. E. J. Newman (2009), Power-Law Distributions in Empirical Data, *SIAM Rev.*, *51*(4), 661–703.
- Coble, C. G., M. E. French, F. M. Chester, J. S. Chester, and H. Kitajima (2014), In situ

- frictional properties of San Andreas Fault gouge at SAFOD, *Geophys. J. Int.*, 199(2), 956–967, doi:10.1093/gji/ggu306.
- Cowan, D. S. (1985), Structural styles in Mesozoic and Cenozoic mélanges in the western Cordillera of North America, *Geol. Soc. Am. Bull.*, *96*(4), 451–462, doi:10.1130/0016-7606(1985)96<451:SSIMAC>2.0.CO;2.
- den Hartog, S. A. M., and C. J. Spiers (2014), A microphysical model for fault gouge friction applied to subduction megathrusts, *J. Geophys. Res. Solid Earth*, *119*, 1510–1529, doi:10.1002/2014JB011151.Received.
- den Hartog, S. A. M., A. R. Niemeijer, and C. J. Spiers (2012a), New constraints on megathrust slip stability under subduction zone P-T conditions, *Earth Planet. Sci. Lett.*, *353–354*, 240–252, doi:10.1016/j.epsl.2012.08.022.
- den Hartog, S. A. M., C. J. Peach, D. de Winter, C. J. Spiers, and T. Shimamoto (2012b), Frictional properties of megathrust fault gouges at low sliding velocities: New data on effects of normal stress and temperature, *J. Struct. Geol.*, *38*, 156–171, doi:10.1016/j.jsg.2011.12.001.
- Di Toro, G., R. Han, T. Hirose, N. De Paola, S. Nielsen, K. Mizoguchi, F. Ferri, M. Cocco, and T. Shimamoto (2011), Fault lubrication during earthquakes., *Nature*, *471*(7339), 494–498, doi:10.1038/nature09838.
- Dieterich, J. H. (1978), Time-Dependent Friction and the Mechanics of Stick-Slip, *Pure Appl. Geophys.*, *116*, 790–806.
- Dieterich, J. H. (1992), Earthquake nucleation on faults with rate- and state-dependent strength, *Tectonophysics*, *211*, 115–134.
- Fagereng, Å. (2011), Geology of the seismogenic subduction thrust interface, *Geol. Soc. London, Spec. Publ.*, 359, 55–76, doi:10.1144/SP359.4.
- Fagereng, Å., and S. A. M. den Hartog (2016), Subduction megathrust creep governed by pressure solution and frictional–viscous flow, *Nat. Geosci.*, doi:10.1038/ngeo2857.
- Fagereng, Å., and R. H. Sibson (2010), Mélange rheology and seismic style, Geology, 38(8),

- 751–754, doi:10.1130/G30868.1.
- Fisher, D., and T. Byrne (1987), Structural evolution of underthrusted sediments, *Tectonics*, *6*(6), 775–793.
- French, M. E., H. Kitajima, J. S. Chester, F. M. Chester, and T. Hirose (2014), Displacement and dynamic weakening processes in smectite-rich gouge from the Central Deforming Zone of the San Andreas Fault, *J. Geophys. Res. Solid Earth*, 119, 1777–1802, doi:10.1002/2013JB010757.
- French, M. E., F. M. Chester, and J. S. Chester (2015), Micromechanisms of creep in clay-rich gouge from the Central Deforming Zone of the San Andreas Fault, *J. Geophys. Res. B Solid Earth*, 120(2), 827–849, doi:10.1002/2014JB011496.
- Harris, R. N., F. S. Schierhorn, and G. Spinelli (2011), Heat flow along the NanTroSEIZE transect: Results from IODP Expeditions 315 and 316 offshore the Kii Peninsula, Japan, *Geochemistry, Geophys. Geosystems*, 12(8), 1–18, doi:10.1029/2011GC003593.
- Hashimoto, Y., and G. Kimura (1999), Underplating process from melange formation to duplexing: Example from the Cretaceous Shimanto Belt, Kii Peninsula, southwest Japan, *Tectonics*, *18*(1), 92–107, doi:10.1029/1998TC900014.
- Hayman, N. W., and L. L. Lavier (2014), The geologic record of deep episodic tremor and slip, *Geology*, 42(3), 195–198, doi:10.1130/G34990.1.
- He, C., Z. Wang, and W. Yao (2007), Frictional sliding of gabbro gouge under hydrothermal conditions, *Tectonophysics*, 445, 353–362, doi:10.1016/j.tecto.2006.05.023.
- He, C., L. Luo, Q. Hao, and Y. Zhou (2013), Velocity-weakening behavior of plagioclase and pyroxene gouges and stabilizing effect of small amounts of quartz under hydrothermal conditions, *J. Geophys. Res.*, 118, 3408–3430, doi:10.1002/jgrb.50280.
- Heilbronner, R., and N. Keulen (2006), Grain size and grain shape analysis of fault rocks, *Tectonophysics*, 427, 199–216, doi:10.1016/j.tecto.2006.05.020.
- Hong, T., and C. Marone (2005), Effects of normal stress perturbations on the frictional properties of simulated faults, *Geochemistry*, *Geophys. Geosystems*, *6*(3), 1–19,

- doi:10.1029/2004GC000821.
- Hyndman, R. D., M. Yamano, and D. A. Oleskevich (1997), The Seismogenic Zone of Subduction Thrust Faults, *Isl. Arc*, 6, 244–260, doi:10.1785/gssrl.79.4.572.
- Ikari, M. J., D. M. Saffer, and C. Marone (2009), Frictional and hydrologic properties of clayrich fault gouge, *J. Geophys. Res. Solid Earth*, *114*, 1–18, doi:10.1029/2008JB006089.
- Ikari, M. J., C. Marone, D. M. Saffer, and A. J. Kopf (2013), Slip weakening as a mechanism for slow earthquakes, *Nat. Geosci.*, 6(6), 468–472, doi:10.1038/ngeo1818.
- Ikari, M. J., A. J. Kopf, A. Hüpers, and C. Vogt (2018), Lithologic control of frictional strength variations in subduction zone sediment inputs, *Geosphere*, *14*(2), 604–625, doi:10.1130/GES01546.1.
- Ikesawa, E., A. Sakaguchi, and G. Kimura (2003), Pseudotachylyte from an ancient accretionary complex: Evidence for melt generation during seismic slip along a master décollement, *Geology*, *31*(7), 637–640, doi:10.1130/0091-7613.
- Ikesawa, E., G. Kimura, K. Sato, K. Ikehara-Ohmori, Y. Kitamura, A. Yamaguchi, K. Ujiie, and Y. Hashimoto (2005), Tectonic incorporation of the upper part of oceanic crust to overriding plate of a convergent margin: An example from the Cretaceous–early Tertiary Mugi Mélange, the Shimanto Belt, Japan, *Tectonophysics*, 401, 217–230, doi:10.1016/j.tecto.2005.01.005.
- Kameda, J., K. Ujiie, A. Yamaguchi, and G. Kimura (2011), Smectite to chlorite conversion by frictional heating along a subduction thrust, *Earth Planet. Sci. Lett.*, 305(1–2), 161–170, doi:10.1016/j.epsl.2011.02.051.
- Kawabata, K., H. Tanaka, and G. Kimura (2007), Mass transfer and pressure solution in deformed shale of accretionary complex: Examples from the Shimanto Belt, southwestern Japan, *J. Struct. Geol.*, 29(4), 697–711, doi:10.1016/j.jsg.2006.11.009.
- Kawabata, K., H. Tanaka, Y. Kitamura, and K. F. Ma (2009), Apparent activation energy and rate-limiting process estimation from natural shale deformed by pressure solution in shallow subduction zone, *Earth Planet. Sci. Lett.*, 287(1–2), 57–63, doi:10.1016/j.epsl.2009.07.032.

- Keulen, N., R. Heilbronner, H. Stünitz, A.-M. Boullier, and H. Ito (2007), Grain size distributions of fault rocks: A comparison between experimentally and naturally deformed granitoids, *J. Struct. Geol.*, 29, 1282–1300, doi:10.1016/j.jsg.2007.04.003.
- Kiminami, K., A. Hamasaki, and T. Matsuura (1999), Geochemical contrast between the Sanbagawa psammitic schists (Oboke unit) and the Cretaceous Shimanto sandstones in Shikoku, Southwest Japan and its geologic significance, *Isl. Arc*, 8(3), 373–382, doi:10.1046/j.1440-1738.1999.00248.x.
- Kimura, G., A. Yamaguchi, M. Hojo, Y. Kitamura, J. Kameda, K. Ujiie, Y. Hamada, M. Hamahashi, and S. Hina (2012), Tectonic mélange as fault rock of subduction plate boundary, *Tectonophysics*, *568–569*, 25–38, doi:10.1016/j.tecto.2011.08.025.
- Kitajima, H., and D. M. Saffer (2012), Elevated pore pressure and anomalously low stress in regions of low frequency earthquakes along the Nankai Trough subduction megathrust, *Geophys. Res. Lett.*, *39*(L23301), 1–5, doi:10.1029/2012GL053793.
- Kitamura, Y. et al. (2005), Mélange and its seismogenic roof décollement: A plate boundary fault rock in the subduction zone An example from the Shimanto Belt, Japan, *Tectonics*, 24(5), 1–15, doi:10.1029/2004TC001635.
- Kohlstedt, D. L., B. Evans, and S. J. Mackwell (1995), Strength of the lithosphere: Constraints imposed by laboratory experiments, *J. Geophys. Res. Solid Earth*, 100(B9), 17587–17602, doi:10.1029/95JB01460.
- Kotowski, A. J., and W. M. Behr (2019), Length scales and types of heterogeneities along the deep subduction interface: Insights from exhumed rocks on Syros Island, Greece, *Geosphere*, *15*, 1–28, doi:10.1130/GES02037.1/4782963/ges02037.pdf.
- Landini, G. (2008), Advanced Shape Analysis with ImageJ, *Proc. Second ImageJ User Dev. Conf.*, *November*, 116–121.
- Linker, M. F., and J. H. Dieterich (1992), Effects of Variable Normal Stress on Rock Friction: Observations and Constitutive Equations, *J. Geophys. Res.*, *97*(B4), 4923–4940.
- Liu, Y., and J. R. Rice (2007), Spontaneous and triggered aseismic deformation transients in a subduction fault model, *J. Geophys. Res. Solid Earth*, 112(9), 1–23,

- doi:10.1029/2007JB004930.
- Logan, J. M., M. Friedman, N. Higgs, C. Dengo, and T. Shimamoto (1979), Experimental Studies of Simulated Gouge and their Application to Studies of Natural Fault Zones, *U. S. Geol. Surv. Open File Rep.*, (79–1239), 305–343.
- Logan, J. M., C. A. Dengo, N. G. Higgs, and Z. Z. Wang (1992), Fabrics of Experimental Fault Zones: Their Development and Relationship to Mechanical Behavior, in *Fault Mechanics* and *Transport Properties of Rocks*, vol. 51, edited by B. Evans and T. F. Wong, pp. 33–67, International Geophysics.
- Marone, C. (1998), Laboratory-Derived Friction Laws and Their Application To Seismic Faulting, *Annu. Rev. Earth Planet. Sci.*, 26, 643–696, doi:10.1146/annurev.earth.26.1.643.
- Marone, C., and C. H. Scholz (1989), Particle-size distribution and microstructures within simulated fault gouge, *J. Struct. Geol.*, 11(7), 799–814, doi:10.1016/0191-8141(89)90099-0.
- Mavrommatis, A. P., P. Segall, and K. M. Johnson (2014), A decadal-scale deformation transient prior to the 2011 Mw 9.0 Tohoku-oki earthquake, *Geophys. Res. Lett.*, 41, doi:10.1002/2014GL060139.Received.
- Mcguire, J. J., J. A. Collins, E. Davis, K. Becker, and M. Heesemann (2018), A Lack of Dynamic Triggering of Slow Slip and Tremor Indicates That the Shallow Cascadia Megathrust Offshore Vancouver Island Is Likely Locked, *Geophys. Res. Lett.*, 45, 11,095-11,103, doi:10.1029/2018GL079519.
- Moore, D. E., R. Summers, and J. D. Byerlee (1989), Sliding behavior and deformation textures of heated illite gouge, *J. Struct. Geol.*, *11*(3), 329–342.
- Moore, G. F. et al. (2009), Structural and seismic stratigraphic framework of the NanTroSEIZE Stage 1 transect, *Proc. Integr. Ocean Drill. Progr.*, 314/315/31, 1–46, doi:10.2204/iodp.proc.314315316.102.2009.
- Moore, J. C. (1989), Tectonics and hydrogeology of accretionary prisms: role of the decollement zone, *J. Struct. Geol.*, 11(1/2), 95–106, doi:10.1016/0191-8141(89)90037-0.

- Moore, J. C., and D. Saffer (2001), Updip limit of the seismogenic zone beneath the accretionary prism of southwest Japan: An effect of diagenetic to low-grade metamorphic processes and increasing effective stress, *Geology*, 29(2), 183–186.
- Nakano, M., T. Hori, E. Araki, S. Kodaira, and S. Ide (2018), Shallow very-low-frequency earthquakes accompany slow slip events in the Nankai subduction zone, *Nat. Commun.*, *9*(984), 1–8, doi:10.1038/s41467-018-03431-5.
- Noda, H., and N. Lapusta (2013), Stable creeping fault segments can become destructive as a result of dynamic weakening., *Nature*, 493, 518–21, doi:10.1038/nature11703.
- Obana, K., and S. Kodaira (2009), Low-frequency tremors associated with reverse faults in a shallow accretionary prism, *Earth Planet. Sci. Lett.*, 287(1–2), 168–174, doi:10.1016/j.epsl.2009.08.005.
- Obara, K. (2002), Nonvolcanic Deep Tremor Associated with Subduction in Southwest Japan, , 296(May), 1679–1682.
- Perfettini, H., J. Schmittbuhl, J. R. Rice, and M. Cocco (2001), Frictional response induced by time-dependent fluctuations of the normal loading, *J. Geophys. Res.*, 106(B7), 13455–13472.
- Phillips, N. J., and J. C. White (2017), Grain size-dependent strength of phyllosilicate-rich gouges in the shallow crust: Insights from the SAFOD site, *J. Geophys. Res. Solid Earth*, 122, 1–24, doi:10.1002/2016JB013828.
- Phillips, N. J., C. D. Rowe, and K. Ujiie (2019), For how long are pseudotachylytes strong? Rapid alteration of basalt-hosted pseudotachylytes from a shallow subduction complex, *Earth Planet. Sci. Lett.*, *518*, 108–115, doi:10.1016/j.epsl.2019.04.033.
- Poppe, L. J., V. F. Paskevich, J. C. Hathaway, and D. S. Blackwood (2001), A Laboratory Manual for X-Ray Powder Diffraction, *U. S. Geol. Surv. Open-File Rep. 01-041*, 88.
- Rabinowicz, E. (1951), The Nature of the Static and Kinetic Coefficients of Friction, *J. Appl. Phys.*, 22(11), 1373–1379, doi:10.1063/1.1699869.
- Rabinowicz, E. (1958), The Intrinsic Variables affecting the Stick-Slip Process, *Proc. Phys. Soc.*,

- *71*, 668–675.
- Rabinowitz, H. S., H. M. Savage, R. M. Skarbek, M. J. Ikari, B. M. Carpenter, and C. Collettini (2018), Frictional Behavior of Input Sediments to the Hikurangi Trench, New Zealand, *Geochemistry, Geophys. Geosystems*, 19, 1–18, doi:10.1029/2018GC007633.
- Reinen, L. A., and J. D. Weeks (1993), Determination of rock friction constitutive parameters using an iterative least squares inversion method, *J. Geophys. Res.*, 98(B9), 15937–15950.
- Rogers, G., and H. Dragert (2003), Episodic Tremor and Slip on the Cascadia Subduction Zone: The Chatter of Silent Slip, *Science* (80-.)., 300, 1942–1944.
- Rowe, C. D., J. C. Moore, F. Meneghini, and A. W. McKeirnan (2005), Large-scale pseudotachylytes and fluidized cataclasites from an ancient subduction thrust fault, *Geology*, *33*(12), 937–940, doi:10.1130/G21856.1.
- Rubin, A. M. (2008), Episodic slow slip events and rate-and-state friction, *J. Geophys. Res.*, *113*(B11414), 1–18, doi:10.1029/2008JB005642.
- Rubin, A. M., and J. Ampuero (2005), Earthquake nucleation on (aging) rate and state faults, *J. Geophys. Res.*, 110(B11312), 1–24, doi:10.1029/2005JB003686.
- Ruina, A. (1983), Slip instability and state variable friction laws, *J. Geophys. Res.*, 88(B12), 10,310-10,370.
- Saffer, D. M., and C. Marone (2003), Comparison of smectite- and illite-rich gouge frictional properties: application to the updip limit of the seismogenic zone along subduction megathrusts, *Earth Planet. Sci. Lett.*, 215(1–2), 219–235, doi:10.1016/S0012-821X(03)00424-2.
- Saffer, D. M., and L. M. Wallace (2015), The frictional, hydrologic, metamorphic and thermal habitat of shallow slow earthquakes, *Nat. Geosci.*, 8(8), 594–600, doi:10.1038/ngeo2490.
- Sammis, C. G., and Y. Ben-Zion (2008), Mechanics of grain-size reduction in fault zones, *J. Geophys. Res. Solid Earth*, 113(2), 1–12, doi:10.1029/2006JB004892.
- Sammis, C. G., R. H. Osborne, J. L. Anderson, M. Banerdt, and P. White (1986), Self-Similar Cataclasis in the Formation of Fault Gouge, *Pure Appl. Geophys.*, *124*(1/2), 53–78.

- Scholz, C. H. (1998), Earthquakes and friction laws, *Nature*, 391, 37–42.
- Scuderi, M. M., and C. Collettini (2016), The role of fluid pressure in induced vs. triggered seismicity: insights from rock deformation experiments on carbonates, *Sci. Rep.*, 6(24852), 1–9, doi:10.1038/srep24852.
- Shelly, D. R., G. C. Beroza, and S. Ide (2007), Non-volcanic tremor and low-frequency earthquake swarms., *Nature*, 446(7133), 305–307, doi:10.1038/nature05666.
- Shibata, T., Y. Orihashi, G. Kimura, and Y. Hashimoto (2008), Underplating of mélange evidenced by the depositional ages: U-Pb dating of zircons from the Shimanto accretionary complex, southwest Japan, *Isl. Arc*, *17*(3), 376–393, doi:10.1111/j.1440-1738.2008.00626.x.
- Skarbek, R. M., and H. M. Savage (2019), RSFit3000: A MATLAB GUI-Based Program for Determining Rate and State Frictional Parameters from Experimental Data, *EarthArXiv*.
- Skarbek, R. M., A. W. Rempel, and D. A. Schmidt (2012), Geologic heterogeneity can produce aseismic slip transients, *Geophys. Res. Lett.*, *39*(L21306), 1–5, doi:10.1029/2012GL053762.
- Sugihara, T., M. Kinoshita, E. Araki, T. Kimura, M. Kyo, Y. Namba, Y. Kido, Y. Sanada, and M. K. Thu (2014), Re-evaluation of temperature at the updip limit of locked portion of Nankai megasplay inferred from IODP Site C0002 temperature observatory, *Earth, Planets Sp.*, 66(107), 1–14.
- Tembe, S., D. A. Lockner, and T. F. Wong (2010), Effect of clay content and mineralogy on frictional sliding behavior of simulated gouges: Binary and ternary mixtures of quartz, illite, and montmorillonite, *J. Geophys. Res. Solid Earth*, 115, 1–22, doi:10.1029/2009JB006383.
- Tonegawa, T., E. Araki, T. Kimura, T. Nakamura, M. Nakano, and K. Suzuki (2017), Sporadic low-velocity volumes spatially correlate with shallow very low frequency earthquake clusters, *Nat. Commun.*, 8(2048), 1–7, doi:10.1038/s41467-017-02276-8.
- Uenishi, K., and J. R. Rice (2003), Universal nucleation length for slip-weakening rupture instability under nonuniform fault loading, *J. Geophys. Res.*, 108(B1), doi:10.1029/2001JB001681.

- Ujiie, K., and G. Kimura (2014), Earthquake faulting in subduction zones: insights from fault rocks in accretionary prisms, *Prog. Earth Planet. Sci.*, *I*(1), 7, doi:10.1186/2197-4284-1-7.
- Ujiie, K., A. Yamaguchi, G. Kimura, and S. Toh (2007a), Fluidization of granular material in a subduction thrust at seismogenic depths, *Earth Planet. Sci. Lett.*, 259, 307–318, doi:10.1016/j.epsl.2007.04.049.
- Ujiie, K., H. Yamaguchi, A. Sakaguchi, and S. Toh (2007b), Pseudotachylytes in an ancient accretionary complex and implications for melt lubrication during subduction zone earthquakes, *J. Struct. Geol.*, 29(4), 599–613, doi:10.1016/j.jsg.2006.10.012.
- Ujiie, K., A. Tsutsumi, Y. Fialko, and H. Yamaguchi (2009), Experimental investigation of frictional melting of argillite at high slip rates: Implications for seismic slip in subduction-accretion complexes, *J. Geophys. Res. Solid Earth*, 114(4), 1–12, doi:10.1029/2008JB006165.
- Virkar, Y., and A. Clauset (2014), Power-law Distributions in Binned Empirical Data, *Ann. Appl. Stat.*, 8(1), 89–119, doi:10.1214/13-AOAS710.
- Wang, K., Y. Hu, and J. He (2012), Deformation cycles of subduction earthquakes in a viscoelastic Earth, *Nature*, 484, 327–332.
- Williams, R. T., J. R. Farver, C. M. Onasch, D. F. Winslow, and A. Sio (2015), An experimental investigation of the role of microfracture surfaces in controlling quartz precipitation rate: Applications to fault zone diagenesis Au Tube Diffusive Transport St. Peter Sand Reactant Substrate Interface (RSI), *J. Struct. Geol.*, 74, 24–30, doi:10.1016/j.jsg.2015.02.011.
- Zhang, L., C. He, Y. Liu, and J. Lin (2017), Frictional properties of the South China Sea oceanic basalt and implications for strength of the Manila subduction seismogenic zone, *Mar. Geol.*, 394(December), 16–29, doi:10.1016/j.margeo.2017.05.006.

CHAPTER 4

Evidence of Localized Failure Along Altered Basaltic Blocks at the Updip Limit of the Seismogenic Zone: Implications for the Shallow Tremor Source

Phillips, N.J., Motohashi, G., Ujiie, K., & Rowe, C.D. Evidence of Localized Failure Along Altered Basaltic Blocks at the Updip Limit of the Seismogenic Zone: Implications for the Shallow Tremor Source, In Review at Geochemistry, Geophysics, Geosystems

4.1 Abstract

Field-based studies have led to several interpretations on the mechanics behind slow slip phenomena at the downdip limit of the seismogenic zone. To date, few field studies have examined the shallow subduction interface which also hosts slow slip phenomena if the subduction thrust is not locked to the trench. We examine an exhumed subduction mélange from conditions that represent the source of shallow slow slip phenomena to determine commonalities between the source regions of tremor at the downdip and updip limits of seismogenic zones. The mélange consists of a shale matrix with scaly foliation produced by pressure solution accommodated creep and frictional sliding, containing rigid blocks of other lithologies, including altered basalt. Cataclasite-bearing faults attest to localized faulting along the margins of basaltic blocks, concurrent with distributed deformation in the shale matrix. These cataclasite bearing faults link individual blocks. Microstructures show mutually crosscutting tensile and shear veins, consistent with failure having occurred at, or near, lithostatic pore fluid pressures. We model the stress concentrations around the margins of basaltic blocks and show that frictional failure of the basalt is predicted to occur at lower shear stresses than frictional failure of the shale, favoring fault development within and along blocks. Calculations of critical nucleation size for the blocks shows that they would fail dynamically at hydrostatic pore fluid pressures, producing a microearthquake.

At the near lithostatic pore fluid pressures required for slow slip phenomena, block lengths sit below the critical nucleation size for dynamic failure and may produce tremor. Shallow slow slip phenomena occur preferentially near subducting seamounts and ridges which may provide a source for blocks of altered basalt.

4.2 Introduction

The discovery of slow slip and tremor at the downdip limit of the seismogenic zone has revolutionized our conceptual model of subduction zone coupling [Beroza and Ide, 2011; Gao and Wang, 2017; Bürgmann, 2018]. The classic paradigm was that seismogenic subduction interfaces are divided into locked and creeping segments [Hyndman et al., 1997; Oleskevich et al., 1999]. Now, transitional zones between locked and creeping segments are known to accommodate a range of slip behaviors including slow slip events (SSEs), tremor, low-frequency earthquakes (LFEs) and very-low-frequency earthquakes (VLFEs) [Obara, 2002; Rogers and Dragert, 2003; Shelly et al., 2007; Beroza and Ide, 2011; Bürgmann, 2018]. Slow slip events are transient increases in slip rate, which often occur coincidently with tremor, a low-frequency seismic signal thought to be composed of LFEs and VLFEs (small seismic events lacking high frequency signals) [Obara, 2002; Shelly et al., 2006, 2007]. Collectively they are referred to as slow slip phenomena. Slip in transitional zones is thought to load the seismogenic zone, and may precede large magnitude earthquakes [Obara and Kato, 2016; Uchida et al., 2016; Voss et al., 2018]. Understanding the mechanisms of slow slip phenomena is therefore important for characterizing the earthquake cycle.

At the updip limit of the seismogenic zone of subduction thrusts, a transitional zone with associated slow slip phenomena is present if the thrust is not locked to the trench [Saffer and Wallace, 2015; Mcguire et al., 2018]. Due to the limited resolution of on-land arrays for detecting deformation in the near trench environment, recent deployments of ocean bottom seismometers

and pressure gauges have greatly increased observations of SSEs, VLFEs, and LFEs at the updip limit of the seismogenic zone [e.g. *Araki et al.*, 2017; *Nakano et al.*, 2018; *Todd et al.*, 2018; *Toh et al.*, 2018].

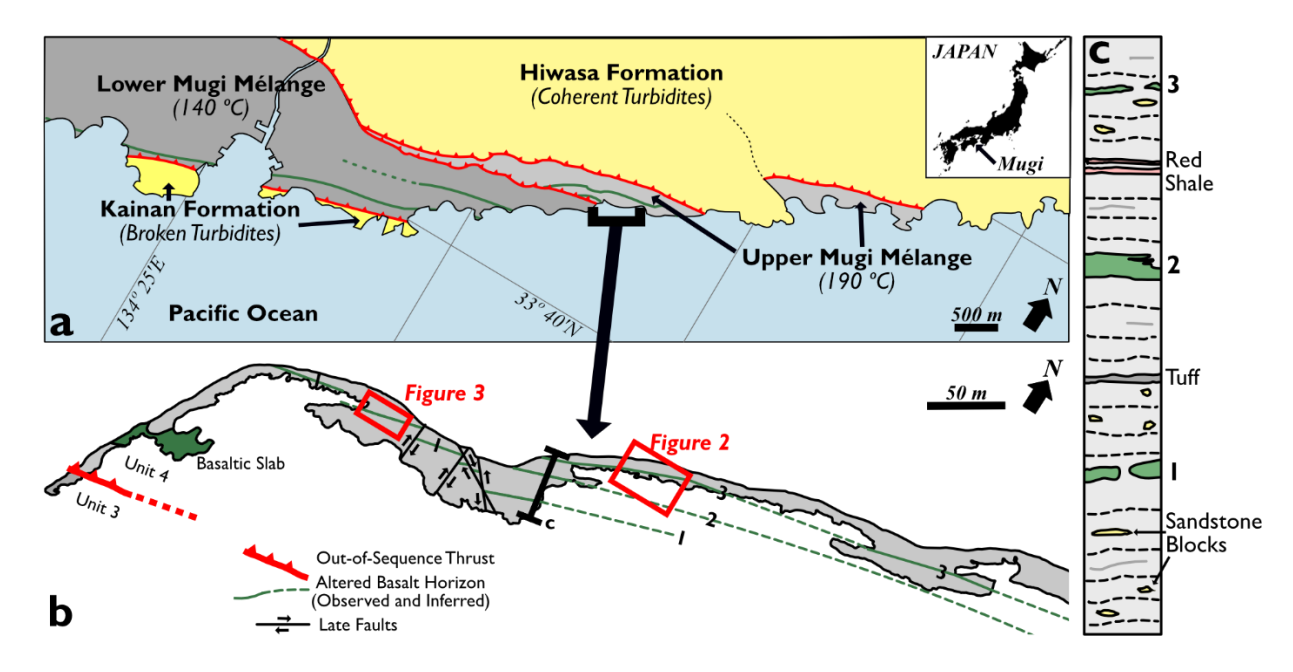


Figure 4-1: a) Schematic of the Mugi Mélange, Japan (after *Shibata et al.* [2008]). Green lines depict basaltic slabs which define the base of each unit. b) Strip map of the coastline in the region of unit 4 showing the three horizons containing basaltic blocks which are the focus of this study. c) Schematic section across the three basaltic block bearing horizons, showing a distinct sequence of units indicating that the repetition of the basalt is not through folding.

Since the discovery of slow slip phenomena, geologists, geophysicists and modellers have attempted to understand their underlying physical mechanisms. From a geological perspective, examining exhumed rocks from transitional zones provides insights into common features between the various settings of slow slip phenomena which may match observed geophysical characteristics. To date, most geologic studies have focussed on characterizing features from the downdip limit of the seismogenic zone [Fagereng et al., 2014; Hayman and Lavier, 2014; Fagereng et al., 2017; Behr et al., 2018; Ujiie et al., 2018; Kotowski and Behr, 2019], while studies

from other transitional zones (e.g. the updip limit of the seismogenic zone and creeping to locked segments of strike-slip faults) are largely absent (an exception being [Compton et al., 2017] from a deep strike-slip fault zone). In this contribution, we examine localized shear surfaces along altered basaltic blocks from the Mugi Mélange, an exhumed shallow subduction interface. We discuss the potential of individual slip surfaces to be related to slow slip phenomenon, calculate necessary characteristics of the source regions using values from experiments on units from the Mugi Mélange, and compare our observations from the updip limit of the seismogenic zone to geologic observations from the downdip limit.

4.3 Geologic Setting

The Mugi mélange is part of the Late Cretaceous to early Tertiary Shimanto Belt: an accretionary complex that stretches the Pacific side of south-east Japan. The Shimanto Belt is an excellent analogue for subduction along the present day Nankai trough, as both record high geothermal gradients due to subduction of young (and hot) oceanic crust [Sakaguchi, 1996; Kimura et al., 2007; Harris et al., 2013]. Located along the eastern coast of Shikoku, the Mugi mélange is divided into lower and upper sections, with maximum paleo-temperatures of 140°C and 190°C respectively [Ikesawa et al., 2005], separated by an out of sequence thrust [Ohmori et al., 1997; Ikesawa et al., 2005; Kitamura et al., 2005]. The upper section is internally composed of a sequence of three thrust imbricates (units 4-6), with thicknesses ranging from 150 to 190 m [Shibata et al., 2008].

At the base of each unit is a 7-67 m thick layer of basalt, interpreted to be underplated oceanic crust. Above the layer of basalt, sandstone and basaltic blocks at a variety of scales (widths of millimetres to tens of metres) sit within a shale matrix [Kimura et al., 2012] which deformed through combined frictional and pressure-solution accommodated processes which were more

effective within the higher temperatures of the upper section [Kawabata et al., 2007, 2009]. Sandstone blocks are distributed through the shale matrix, while basaltic blocks tend to be confined to individual horizons within the shale matrix.

Along the contacts of basaltic slabs and blocks is a ~60 cm thick altered rim where the basalt has been albitized. Evidence of paleoseismic slip within this altered basalt has been recorded along the upper contacts of basaltic slabs from 2 units [units 2 and 4; *Ujiie et al.*, 2007; *Phillips et al.*, 2019]. Experiments have shown that the frictional properties of altered basalt are favorable for localized slip (e.g. it is velocity-weakening; [*Phillips et al.* submitted]). We went to the field to document the lithologies, geometries, and material properties of shallow subduction zones, which could combine to form a tremor genic environment.

4.4 Field Observations

The basaltic blocks occur in three horizons within unit 4 (Figure 4-1b). The three horizons are separated by a distinct stratigraphy (Figure 4-1c), indicating that the repetition of the basalt bearing horizons is not due to folding. The thickness of each horizon is ~3 m, though individual blocks are no more than 2 m in thickness (Figures 4-1 to 4-3). Maximum block length is ~ 6 m. The distance between individual blocks is generally less than the length of the blocks (Figures 4-2 to 4-4). Basaltic blocks show a strong shape preferred orientation parallel with the foliation in the shale matrix (Figures 4-2, 4-3). Aspect ratios of individual blocks range from 1-10, with no clear trend between block length and aspect ratio (Figure C1).

Large blocks (> 30 cm in length) have unaltered cores (similar to the basaltic layer at the base of each unit; [*Phillips et al.*, 2019]) which are enveloped by light green altered basalt (Figure 4-4). Depth of alteration ranges from cm scale to 10's of cm (Figure 4-4). Small blocks (<30 cm in length) have been completely altered (Figure 4-4). A field magnetometer was used to

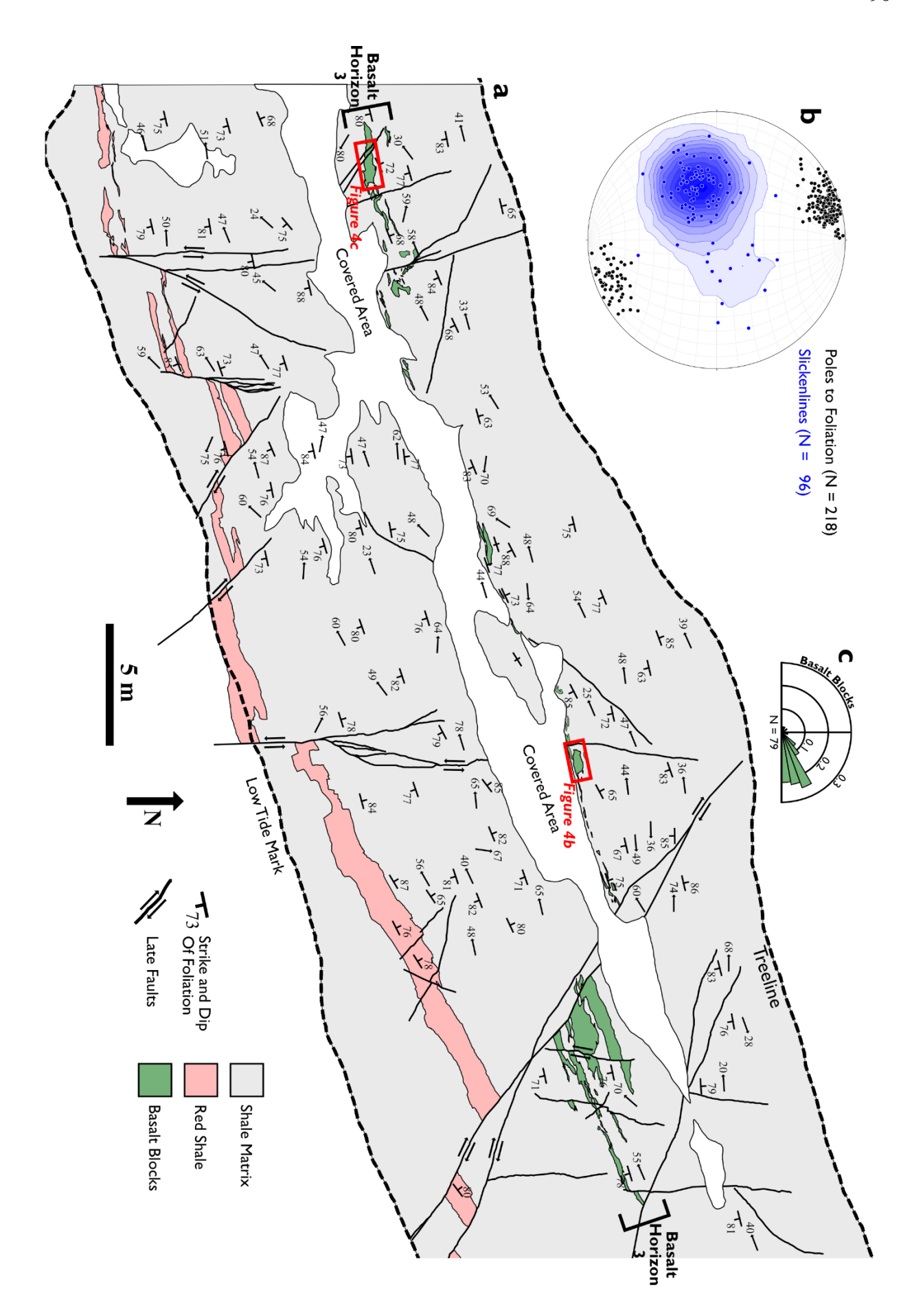


Figure 4-2: a) Geologic map of basalt horizon 3. b) Stereonet showing poles to foliation planes, and slickenlines on shale and basalt margin surfaces. c) Orientation (Feret angle) of long axes of mapped basaltic blocks (as a probability density function).

characterize the depth of alteration. Basaltic cores retained a high magnetic susceptibility (> 5 x 10⁻³ T; Figure 4-4g-h) while in the altered basalt along the margins of blocks, the magnetic susceptibity was approximately an order of magnitude lower. The magnetic susceptibility of the shale was always lower than the altered basalt. Measurements of magnetic susceptibility on the basaltic slab at the base of unit 4 showed a similar progression from shale through to unaltered basalt (Figure C2).

Fault zones containing cataclasites occur within the light green altered basalt along the margins with the shale matrix (Figure 4-4a-f). Faults connect individual blocks, and between blocks are composed of smeared altered basaltic cataclasite mixed with shale (Figure 4-6a). Shear surfaces occur along the outer margins of basaltic blocks (Figure 4-4a-f). In addition to seeing altered basaltic cataclasites along faults, cataclasites are seen mixing with the shale in the regions around basaltic blocks. Isolated regions of altered basalt are found in shale matrix and vice versa (Figure 4-4b).

Two micromaps were produced of basalt bearing horizons. Blocks in micromap 1 (Figure 4-2) show an asymmetry in the distribution of cataclasites and shear surfaces consistent with north side up, south side down, right-lateral shear. This is consistent with the steeply dipping (to the SE) slickenlines (Figure 4-2b). In micromap 2 (Figure 4-3), shear surfaces show a north side up, south side down shear sense, but the strike-slip component of shear is less consistent (Figure 4-3a). Slickenlines show a range of orientations from steeply dipping to the east to steeply dipping to the west, which may explain the less consistent strike-slip component of shear sense indicators in map

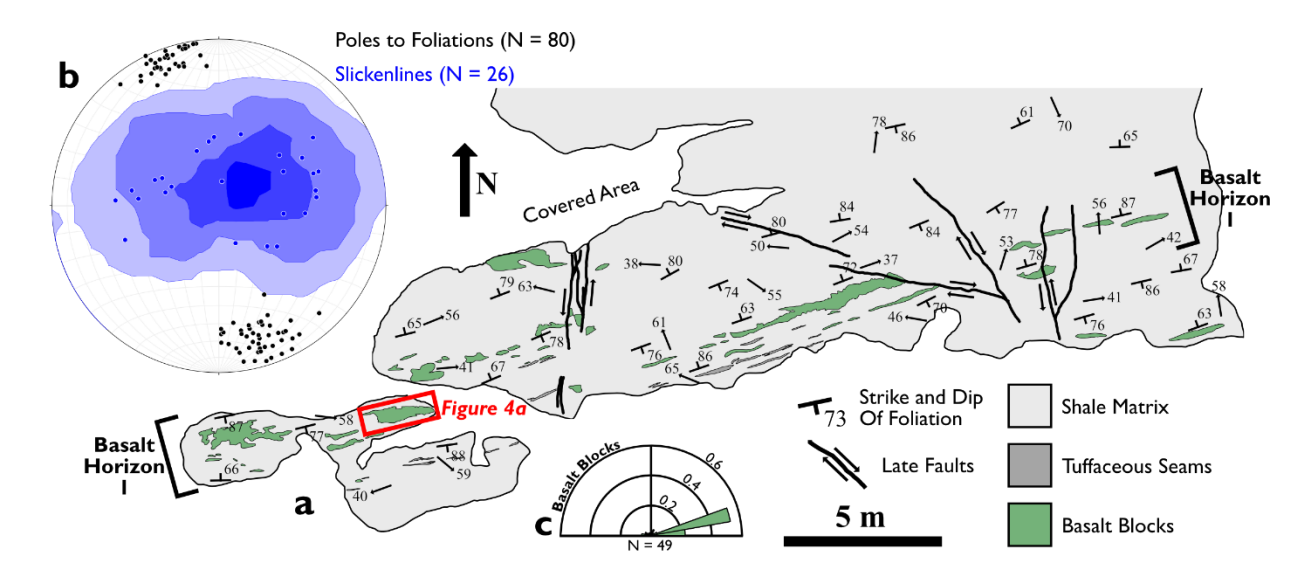


Figure 4-3: a) Geologic map of basalt horizon 1. b) Stereonet showing poles to foliation planes and slickenlines on shale and basalt margin surfaces. Blue contours are calculated using the Kamb method (lowest contour is $2 - 3 \sigma$). c) Orientation (Feret angle) of long axes of mapped basaltic blocks (as a probability density function).

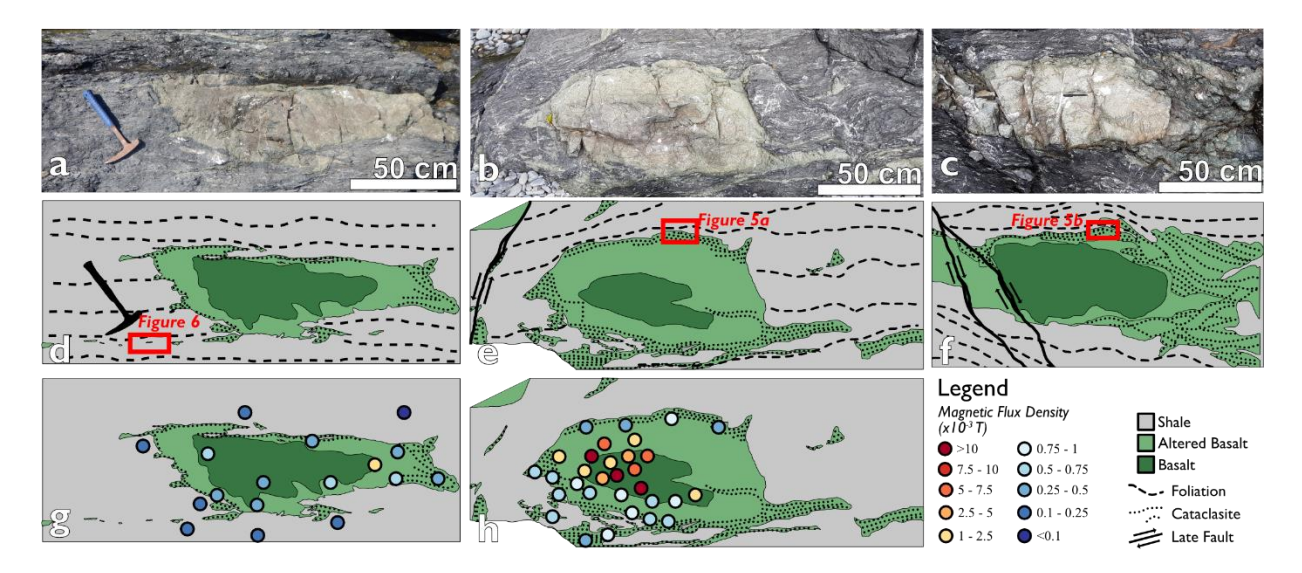


Figure 4-4: a-c) Field photos of basaltic block macrostructures. d-f) Cartoons of macrostructures. Unaltered cores are enveloped by altered basalt. Localized cataclasites occur along block margins. Discontinuous seams of cataclasite coat slip surfaces which link blocks (d, in region around Figure 6 box). g-h) Magnetic flux density measurements from 2 blocks using a field magnetometer. Unaltered blocks show a high flux density compared with altered margins, similar to slabs at the base of each unit (See Figure S1 for magnetic flux density across a slab).

view (Figure 4-3b). The recorded kinematics are consistent with subduction related deformation, and the steepening of the fault fabric represents late-rotation of the Mugi Mélange [Kitamura et al., 2005].

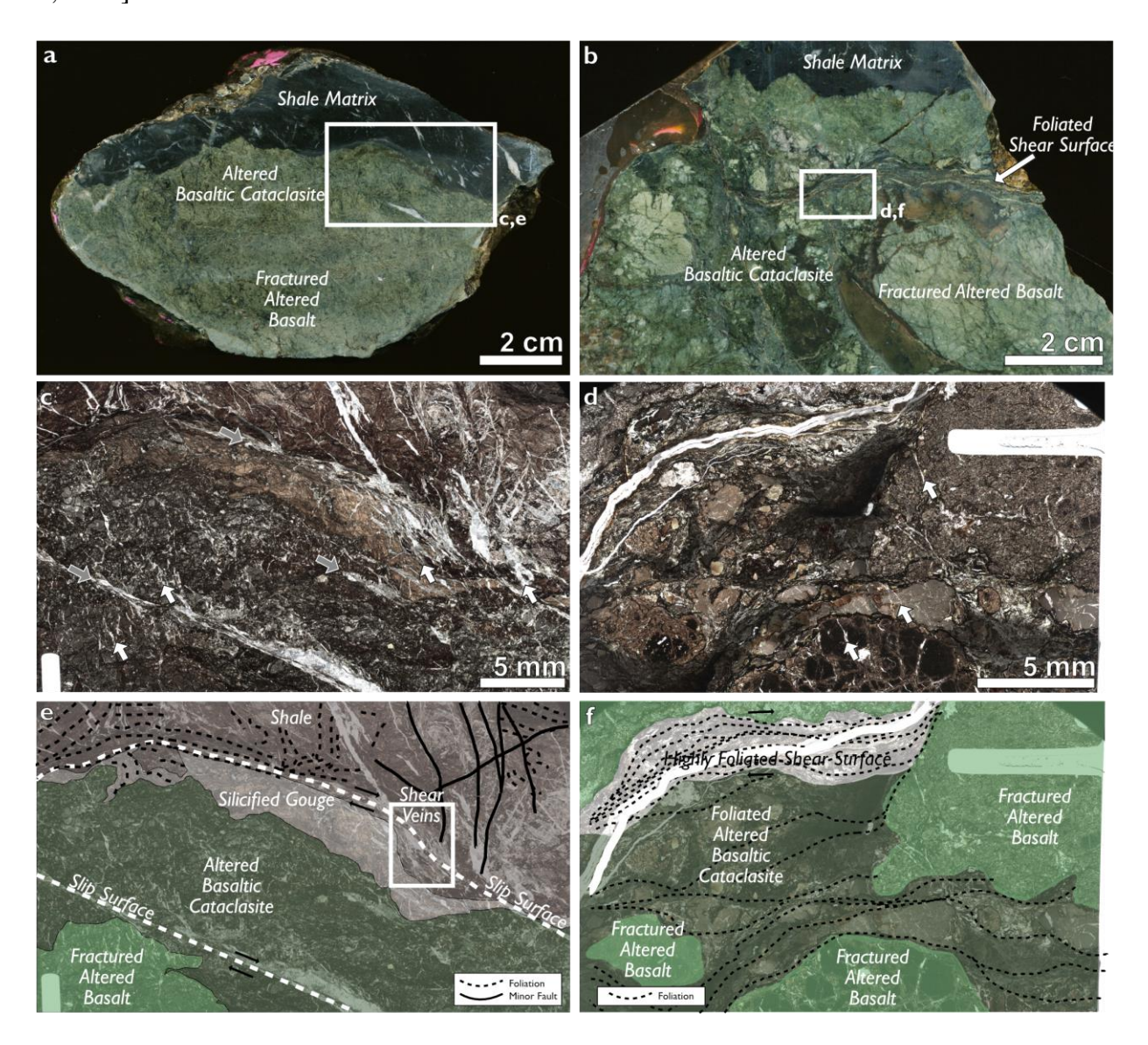


Figure 4-5: Representative examples of well developed cataclasites along the margins of altered basaltic blocks. a,b) Hand sample scans of margins of basaltic blocks. c,d) Plane polarized light photomosaic of margin and e,f) false colored image depicting microstructural domains. In c-d, grey arrows show shear veins, and white arrows show tensile fractures, which mutually crosscut each other. Box in (e) shows a concentration of coeval shear and tensile veins within the shale matrix. All photos show top to the right shear sense.

The mixing of altered basaltic cataclasite with the shale matrix indicates that the mélange was continuing to accommodate distributed simple shear following incorporation of basaltic slabs into the mélange through underplating [Brodsky et al., 2009]. Additionally, slickenlines at the edge of basaltic blocks are parallel to slickenlines in the shale matrix, attesting to coeval deformation of the matrix and the localized shear surfaces on block margins.

4.5 Microstructures

Figures 4-5 and 4-6 show representative examples of cataclasites along the margins of basaltic blocks. Highly fractured altered basalt and altered basalt derived cataclasites occur from the boundary with the shale, and penetrate cm's to 10's of cm into the blocks (Figure 4-5a, d). Along the margins of blocks, cataclasites can be seen injecting into the shale matrix (Figures 4-5a, 4-6b). In the cataclasites a fine matrix separates clasts, and both clast supported and matrix supported cataclasites are observed (Figures 4-5, 4-6). In clast supported cataclasites, clasts are sub-angular, while matrix supported cataclasites exhibit greater rounding of clasts and a stronger foliation defined by dark seams of concentrated phyllosilicates and long axes of clasts (Figure 4-5d).

Through-going slip surfaces occur as either matrix supported cataclasites (Figure 4-5d) or shear veins parallel with the slip direction (Figure 4-5c). Quartz-carbonate filled shear veins and tensile fractures mutually cross-cut each other (Figures 4-5c, 4-6). In the hydrofractures, calcite cores are rimmed by quartz, while shear veins show a more chaotic relationship between the two phases. Calcite in veins exhibit pervasive type-1 twins [*Passchier and Trouw*, 2005].

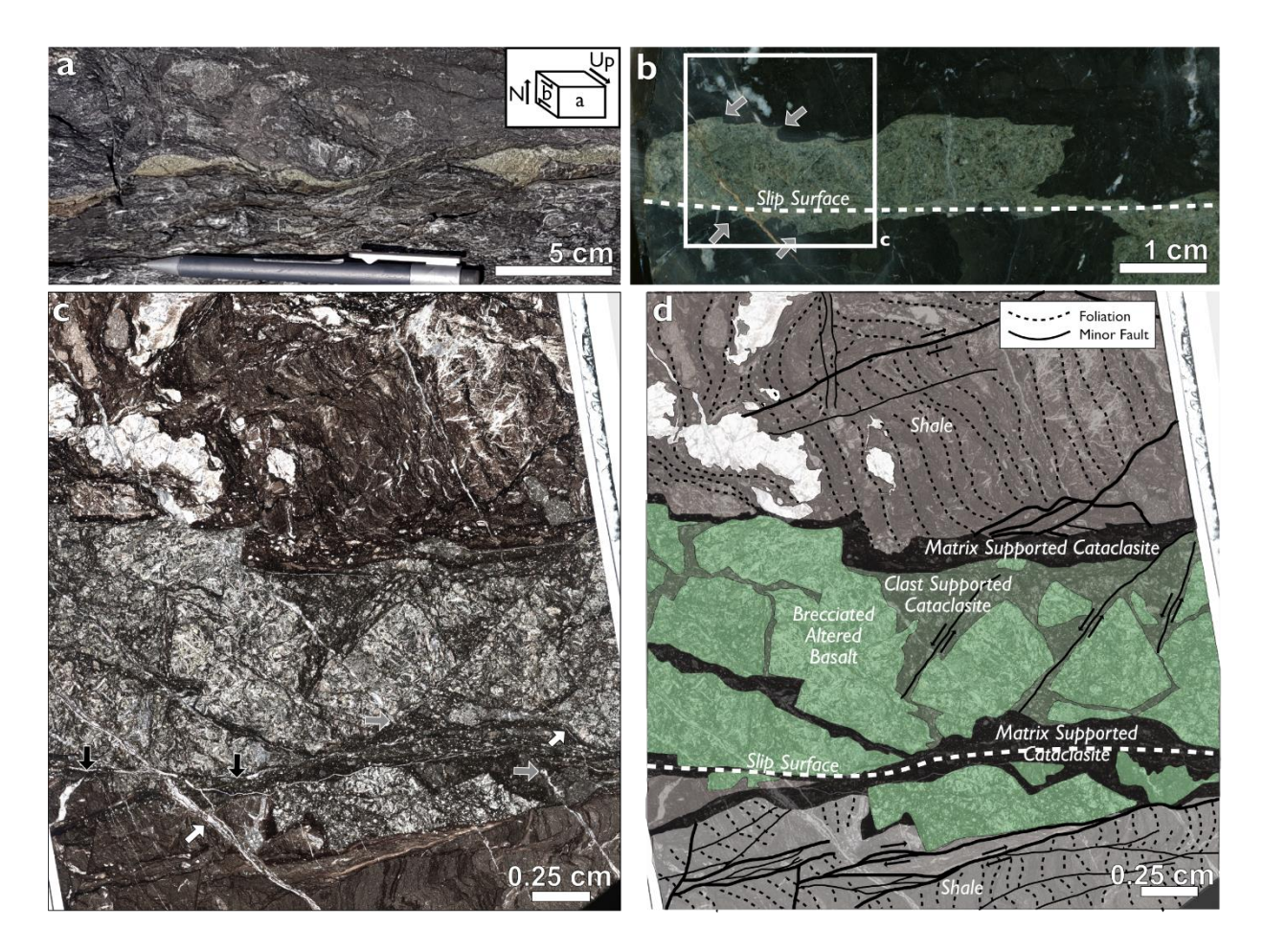


Figure 4-6: a) Close up field photo of a fault (which links two blocks) containing a discontinuous seam of sheared altered basalt. Inset shows structural relationship between the field and microstructural photos. b) Hand sample of the altered basaltic seam. A localized slip surface cuts the altered basalt along its bottom margin. Small asymmetric injections (grey arrows) of basaltic cataclasite into the shale occur along the contacts. c) Thin section stitch in plane polarized light showing faults cutting along both margins of the altered basalt. Veins both crosscut (white arrows) and are cross-cut (black horizontal arrows) by the matrix supported cataclasite filled faults. Shear veins (black vertical arrows) occur within the matrix supported cataclasite. d) False-colored image of c, highlighting structural elements.

Foliations in the shale (near the contact with altered basalt) are frequently disrupted (Figures 4-5e, 4-6d). Small, local faults cut the shale, and shear sense on the small faults is

consistent with the overall sense of shear. Silicification of the shale occurs along the margins of basaltic blocks.

We infer that the matrix supported cataclasites hosted greater shear displacements, and localized slip than clast supported cataclasites. The mutually cross-cutting shear and tensile veins indicate that slip was occurring under near lithostatic pore fluid pressure conditions. We infer that localized slip occurred in the altered basalt, and caused disruption of the foliation in the shale matrix.

4.6 Models of Stress Distributions

4.6.1 Why Model Stress Distributions?

Field and microstructural observations from the Mugi Mélange show discrete fault surfaces cutting along altered basaltic units (Figures 4-4 to 4-6), which are known to be velocity-weakening from triaxial deformation experiments [*Phillips et al.*, submitted]. For the discrete faults to have formed in altered basalt, a stress threshold must have been reached to activate frictional sliding. However, shale is frictionally weaker than altered basalt ($\mu = \sim 0.4$ for shale, ~ 0.6 for altered basalt; [*Phillips et al.*, submitted]), and microstructural/geochemical work has shown that that the shale at the Mugi Mélange deformed through pressure-solution accommodated creep [*Kawabata et al.*, 2007, 2009]. This indicates that the flow stress for pressure-solution accommodated creep was lower than for frictional sliding in the shale. Why then was slip partitioned into localized surfaces, and not accommodated solely through distributed deformation in the shale? We hypothesize that stress concentrations along the altered basaltic blocks during distributed shear in the shale caused local frictional failure in the altered basalt. To test this hypothesis, we modelled stress and strain-rates within basaltic blocks during distributed shear in the shale matrix.

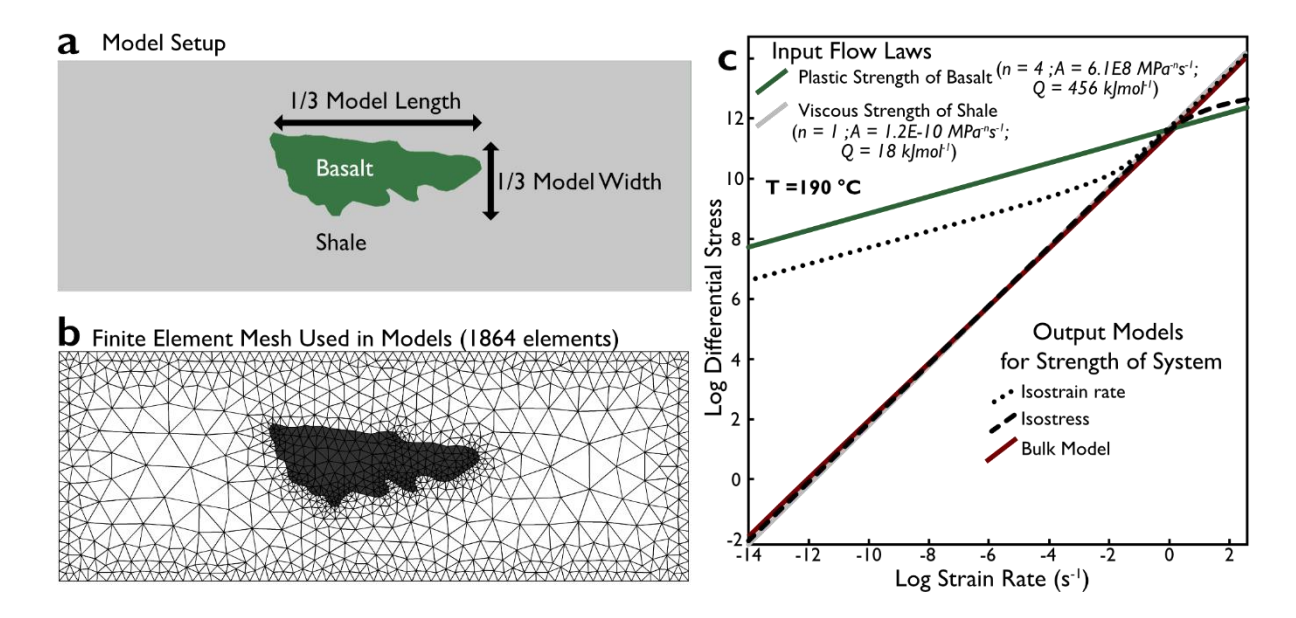


Figure 4-7: a) Typical model setup of stress around a basaltic block. b) Finite element mesh used in models of stress and strain-rate heterogeneity around strong basaltic inclusions. c) Model outputs for mixing laws between basalt and shale matrix. The model closely follows the isostress end-member at low geologic shear strain-rates.

Within subduction zones, shale dominated sequences deform through pressure solution mediated processes at flow stresses lower than a few tens of MPa [Bos and Spiers, 2002; Stockhert, 2002; Mariani et al., 2006; Trepmann and Stöckhert, 2009; den Hartog and Spiers, 2014; Fagereng and den Hartog, 2017]. However, within viscously flowing mediums, stress concentrations an order of magnitude higher may occur along the margins of stronger lithologies or within crosscutting elements such as veins or dikes [Stöckhert et al., 1999; Trepmann and Stöckhert, 2009; Grigull et al., 2012]. Stress within a mixture of power-law materials falls between two end-member models, isostress and isostrain-rate [Tullis et al., 1991]. After Montési [2007] and Gerbi et al. [2015], for j phases, these end-members can be described by

$$\sigma = \sum_{i=1}^{j} (\dot{\varepsilon})^{(\frac{1}{n_i})} \Phi_i B_i^{-(\frac{1}{n_i})} \quad \text{and}$$
 (4.1)

$$\dot{\varepsilon} = \sum_{i=1}^{j} \Phi_i B_i \sigma^{(n_i)} \tag{4.2}$$

respectively, where σ is stress, $\dot{\varepsilon}$ is strain-rate, Φ_i is the modal proportion of each phase, and B_i is a grouping of the other parameters (*i.e.* activation energy, temperature and pressure effects) for each phase. For mixtures of materials with varying power law exponents, there exists an equiviscous point where the strength of one phase becomes greater than the other (Figure 4-7c). Since stress falls between the isostress and isostrain-rate models, there is a limited range of possibilities for stress near the equiviscous point [Tullis et al., 1991; Gerbi et al., 2015]. Moving away from the equiviscous point, there exists a greater range of possible model solutions (Figure 4-7c), and the outcome of the model depends on model assumptions. There are many methods of determining the bulk viscosity of two mixed power law materials [e.g. Tullis et al., 1991; Handy, 1994; Huet et al., 2014], however most do not calculate local stress and strain-rate heterogeneity using observed microstructures. To solve for local stresses and strain-rates during shear, we employ a finite element method which takes the interconnectivity and distribution of phases into account.

4.6.2 *Modelling Methods:*

We modelled stress and strain-rate concentrations around the strong basalt blocks using the PLC (Power Law Creep) toolbox developed at the University of Maine. The PLC toolbox uses Asymptotic Expansion Homogenization (AEH) over a finite element mesh to determine the microscale stress and strain-rate distributions in a multiphase system [Gerbi et al., 2015 and refs within]. The toolbox calculates the bulk properties of a mixture, explicitly taking into account the interconnectivity and distribution of phases. From the bulk viscosity, microscale stress and strain-rate are calculated for each mesh element.

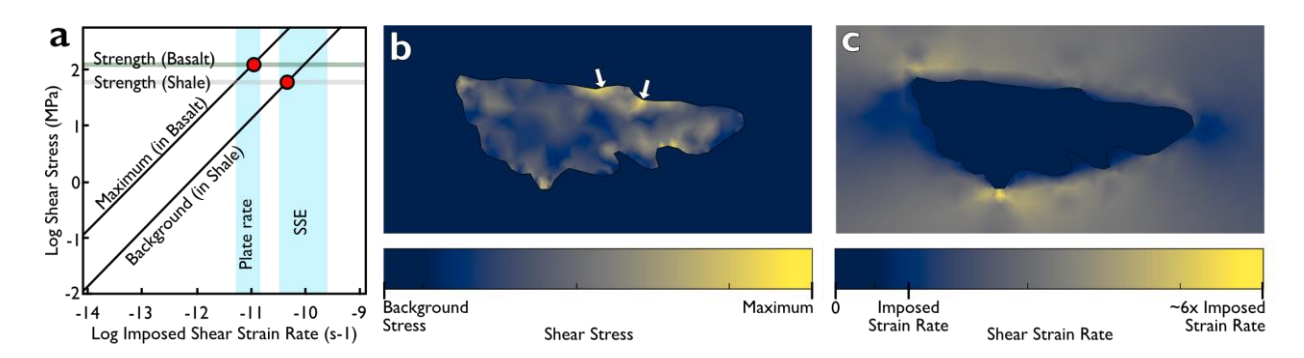


Figure 4-8: a) Evolution of maximum shear stresses in the basalt, and background shear stresses in the shale with increasing imposed shear strain-rate in the models. The frictional strengths of altered basalt and shale (as determined through experiments at in situ conditions; [Phillips et al. submitted]) are plotted as horizontal lines. Red dots show where the frictional strength of altered basalt and shale are reached in the models. Note that the frictional strength of basalt is reached before the shale, indicating that frictional failure will occur along basaltic margins before shale matrix. Vertical blue boxes show ranges of shear strain-rates for plate-rate deformation (3-7 cm / yr) and for slow slip events (10 - 100 cm / yr) accommodated across the shale matrix. b,c) Outputs of shear stresses (b) and shear strain-rates (c) from the models. Note that the maximum and background can be ascertained from (a) for a given imposed shear strain-rate. Model margins have been cropped (compare with Figure 4-7a) to highlight results within the basaltic block.

For the model setup, we centered a single basaltic block, with a characteristic field morphology (Figure 4-4a) within a shale matrix. The block lengths and widths are both ~1/3 of the dimensions of the model to minimise edge effects, and so that the bulk properties of the model follow the shale. A finite element mesh was generated which conformed to the phase boundaries (Figure 4-7b). We modelled the shale matrix to be deforming through a modified flow law for viscous creep ($n_i = 1$) using the activation energy determined by *Kawabata et al.* [2009], where at a strain-rate of 10^{-11} s⁻¹ the axial flow stress is 10 MPa under the temperature conditions of the upper Mugi Mélange ($T = 190^{\circ}$ C; Figure 4-7c). The behaviour of the basaltic blocks is modelled using the power law flow law (crystal plastic) for glass-free basalt derived in *Violay et al.* [2012]

(Figure 4-7c). We applied a constant shear strain-rate to the model boundaries, and ran 60 runs, examining strain-rates from 10^{-14} to 10^3 (Figure 4-7c). The goal was to determine whether the stress threshold for frictional failure in the basalt would be reached before frictional failure in the shale as strain-rate was increased.

4.6.3 Model Results:

Typical model results at geologically reasonable strain-rates are presented in Figure 4-8. An order of magnitude increase in stress from the deforming shale matrix material occurs along the margins of the strong basaltic blocks (Figure 4-8a,b). At a strain-rate of 10^{-11} s⁻¹, shear stresses along the margins of the basaltic blocks reach the threshold for frictional failure in the altered basalt (Figure 4-8a). This is at a slower rate than for the shale matrix ($\sim 5 \times 10^{-11} \text{ s}^{-1}$) indicating that the altered basalt would be more likely to fail frictionally than the shale.

Shear strain-rate heterogeneity is predicted within the shale matrix (Figure 4-8c), with strain-rate highs along the margins with the altered basalt. A negligible shear strain-rate is accommodated in the basalt as the threshold for viscous crystal plastic failure is never reached in the basalt (Figure 4-8c). As the stresses remain below the failure threshold within the blocks, the models predict no internal deformation of the blocks by any brittle or ductile mechanism.

Models show that stress concentrations can occur along altered basaltic blocks which are high enough to promote frictional sliding along the altered basaltic interface, so long as a critical strain-rate of 10⁻¹¹ s⁻¹ is obtained across the mélange. Assuming active deformation across the entire ~150 m of a single thrust imbricate in the upper Mugi mélange, strain rates this high would be expected if the relative plate convergence rate is somewhat high (~7 cm / yr; Figure 4-8a), but would certainly occur during a slow slip event, where slip rates range from 10-100 cm/yr (Figure

4-8a), or during time periods when actual deforming thickness of the mélange is less than the total accumulated thickness of deformed mélange [c.f. *Rowe et al.*, 2013].

Rock Type	Experiment	Т	P _c	P _f	Ь	σ_n	Δσ	D_c
Altered Basalt	AB2	150	120	0.357	0.009	145	1.305	45
Altered Basalt	AB3	150	120	0.7	0.01	63	0.63	29

Table 4-1: Summary of results from friction experiments in a triaxial apparatus on altered basalt (*Phillips et al.* [submitted]).

4.7 Discussion

4.7.1 What happens when the stress threshold is reached?

Our models of stress state with increasing shear strain-rate indicate that the margins of basaltic blocks would fail frictionally before the shale matrix. How would slip occur once this stress threshold was reached? Uenishi and Rice [2003] and Rubin and Ampuero [2005] considered a slowly loaded fault. Slip initiates when the stress state equals the strength of the fault, however, failure is a slow process, so loading continues to increase the stress on the fault until dynamic failure occurs after a "critical nucleation length" is reached. In the framework of our study, we consider our basaltic blocks to be nucleation points for failure. In order for slip to produce a seismic signal, block lengths must be long enough to allow for dynamic failure. If the block length is shorter, than the block fails through slow slip. We note here that block length may not equate a single block, as blocks are linked with through-going faults coated in altered basaltic cataclasite (Figure 4-4a), with well developed matrix supported cataclasites indicative of localized displacement (Figure 4-6). In the framework of tectonic mélanges, where blocks are constantly moving and rearranging themselves with slip [e.g. Tarling and Rowe, 2015; Beall et al., 2019],

and where slip surfaces are frequently disrupted and new surfaces are constantly forming [Rowe et al., 2011], that block lengths themselves are a dynamic feature.

While there are several proposed methods for calculating the critical nucleation length [e.g. Okubo and Dieterich, 1984; Dieterich, 1992; Ohnaka, 2000; Uenishi and Rice, 2003; Rubin and Ampuero, 2005], they have a similarity of form, and we therefore use the recent analyses of Uenishi and Rice [2003] and Rubin and Ampuero [2005]. In their derivations, the critical nucleation length (L) is described by

$$L = 2 * C * (\mu' * \frac{D_c}{b\sigma_n})$$
 (4.3)

where μ' is the shear modulus, C is a numerical constant (with a value between 1 and 1.5), Dc is the critical slip distance determined through experiments, b is the evolution effect determined in rate-and-state experiments, and σ_n is the normal stress on the fault surface. We calculate the critical nucleation lengths for altered basaltic blocks using the experimental parameters determined in triaxial deformation experiments on altered basalt at the in situ conditions of the Mugi mélange [Phillips et al., submitted], which are summarized in Table 4-1. We consider the elasticity of the system (altered basaltic blocks within a shale matrix) to be controlled by the shear modulus of the shale, which has been determined in laboratory velocity measurements on samples collected from the Mugi mélange (Vs = ~2000 m/s corresponding to μ' = ~11.5 GPa) [Hashimoto et al., 2013]. We note that these shear velocities are likely high relative to when the mélange was active, due to a decrease in porosity (consolidation and lithification) in the shale matrix post-deformation. The calculated critical nucleation lengths may therefore be overestimated.

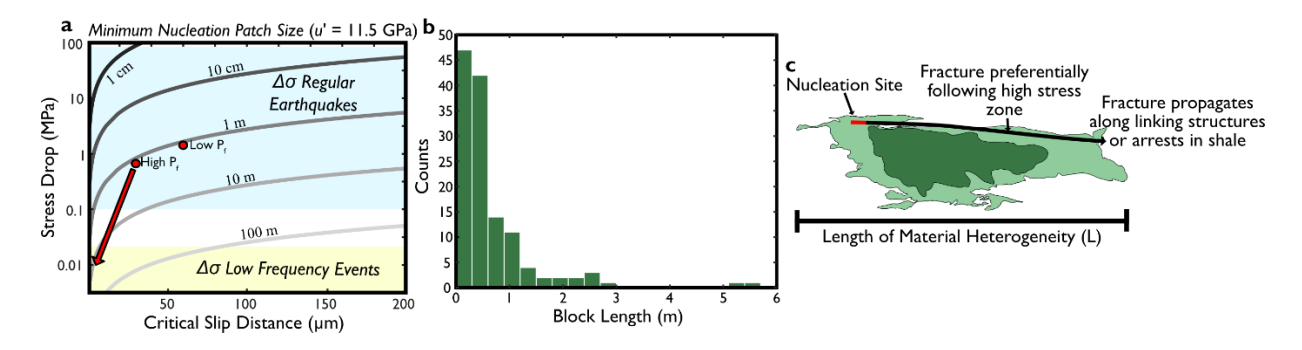


Figure 4-9: Relationship between basalt block sizes and nucleation patch size. a) Diameter of minimum nucleation patch size for unstable slip after Uenishi and Rice [2003] for varying stress drops and critical slip distances. Red dots show results from experiments on altered basalt from Phillips et al. [submitted] at pore fluid factors (Pf) of 0.357 (low) and 0.7 (high). Arrow shows the expected evolution of the critical nucleation length as pore fluid pressures increase to near lithostatic conditions. b) Histogram of block lengths recorded from maps in Figures 4-2 and 4-3. c) Cartoon of a basaltic block with altered margins. We hypothesize that zones of high stress along block margins serve as nucleation points for slip. Slip could either propagate between blocks along faults with smeared basaltic cataclasite (e.g. Figure 4-6), or arrest in the velocity-strengthening shale matrix.

4.7.2 Calculations of block sizes required to nucleate a real earthquake

Calculations of critical nucleation lengths for basaltic blocks from Mugi are presented in Figure 4-9a. At *in situ* conditions, the stress drop associated with velocity steps in experiments ranges from 1.3 to 0.63 MPa for pore fluid factors of 0.357 and 0.7 respectively (Table 4-1). The critical nucleation lengths at these pore fluid pressures is on the order of 1-2 meters, indicating that the larger blocks in our study area would fail dynamically and produce microseismic events (e.g. normal earthquakes in terms of frequency distribution of seismic signals). In order to reach stress-drops similar to (very-)low frequency events (~0.001 - 0.01 MPa; [*Ito and Obara*, 2006b; *Ito et al.*, 2009; *Thomas et al.*, 2016]), a pore fluid factor of ~ 0.99 is required, consistent with observations of dynamic and tidal triggering of VLFEs and LFEs [*Ito and Obara*, 2006a; *Annoura*

et al., 2017; Cruz-Atienza et al., 2018]. The critical slip distance (D_c) decreases as pore fluid pressure increases in experiments [Scuderi and Collettini, 2016; Phillips et al. submitted], so we predict critical nucleation lengths on the order of ten meters under near lithostatic pore fluid pressures (Figure 4-9a). The largest blocks in our study are \sim 6 m, indicating that these blocks may slip through aseismic transients.

We note that our critical block sizes may not equate to the rupture size of a VLFE. At Nankai, very-low frequency events regularly have magnitudes of 3 to 5, corresponding to rupture dimensions of 5 to 10 km [Ito and Obara, 2006b; Toh et al., 2018]. Given the critical nucleation lengths calculated here, it is unclear why individual asperities of this length scale would not produce regular earthquakes. One possible explanation is that sub-patches of velocity-weakening material exist within a larger VLFE patch, rather than the whole VLFE slip surface being controlled by a single velocity weakening asperity. This is a common modelling approach to produce slow slip [Ando et al., 2010; Skarbek et al., 2012] and has been hypothesized to be the case for LFEs from Cascadia [Chestler and Creager, 2017]. We hypothesize that this could also be the case for VLFE events in the shallow portion of subduction zones. We observe faults with smeared altered basaltic cataclasite linking individual block margins, and hypothesize that large magnitude VLFEs may occur through successive failure of many subcritical velocity-weakening blocks. Block horizons in our mapping area extend the length of the mapping area (~ 500m in length; Figure 4-1b), and the failure of interconnected blocks of velocity-weakening material could therefore produce a larger magnitude event.

Observations of coeval slow slip and tremor have shown that the frequency and intensity of LFEs and VLFEs is related to the stressing rate (regulated by slip rate) on the fault [Wech and Bartlow, 2014]. At faster slip rates, tremor is more likely to occur, and occurs more frequently. In

our conceptual model of stressed blocks embedded within a viscously flowing matrix, increasing the flow rate in the zone of distributed shear (during a slow slip event) causes increases in stress along block margins. This would make more blocks prone to failure, and would cause blocks to fail more frequently as the elastic stresses would rebuild more quickly.

4.7.3 Comparison with geological models from the downdip limit of the seismogenic zone

Exhumed rocks from the downdip limit of the seismogenic zone have led to two principal hypotheses on the occurrence of slow slip and tremor. One hypothesis is that strong blocks embedded within a weak matrix leads to localized failure in the blocks (LFEs and VLFEs) during distributed deformation in the shale [Fagereng, 2011; Fagereng et al., 2014; Hayman and Lavier, 2014; Kotowski and Behr, 2019]. Failure of blocks could either be caused by, or cause increased strain-rates in the matrix [Fagereng et al., 2014; Hayman and Lavier, 2014; Beall et al., 2019].

A second hypothesis is that local dehydration leads to fluid overpressures within the weak matrix, causing the formation of coeval shear veins and hydrofractures within the matrix. Individual crack-seal events in quartz shear veins are thought to be due to successive fluid overpressure events during individual tremor sequences [Fagereng et al., 2017; Ujiie et al., 2018]. The mixture of hydrofracturing and shear slip during vein formation is thought to produce the low frequency signal typical of LFEs and VLFEs. Slip occurs within the shear veins and the recurrence interval of episodic tremor and slow slip may then arise from a combination of fracture healing and fluid release rates [Fagereng et al., 2017; Ujiie et al., 2018].

We favor the failure of blocks model over the shear veins model. Within the shear vein model it is difficult to reconcile the increased rate of LFEs and VLFEs with increasing slip rate [Wech and Bartlow, 2014]. If healing times for individual veins controls the recurrence rate of tremor, why then would increasing slipping rate allow tremor to occur more frequently? Within

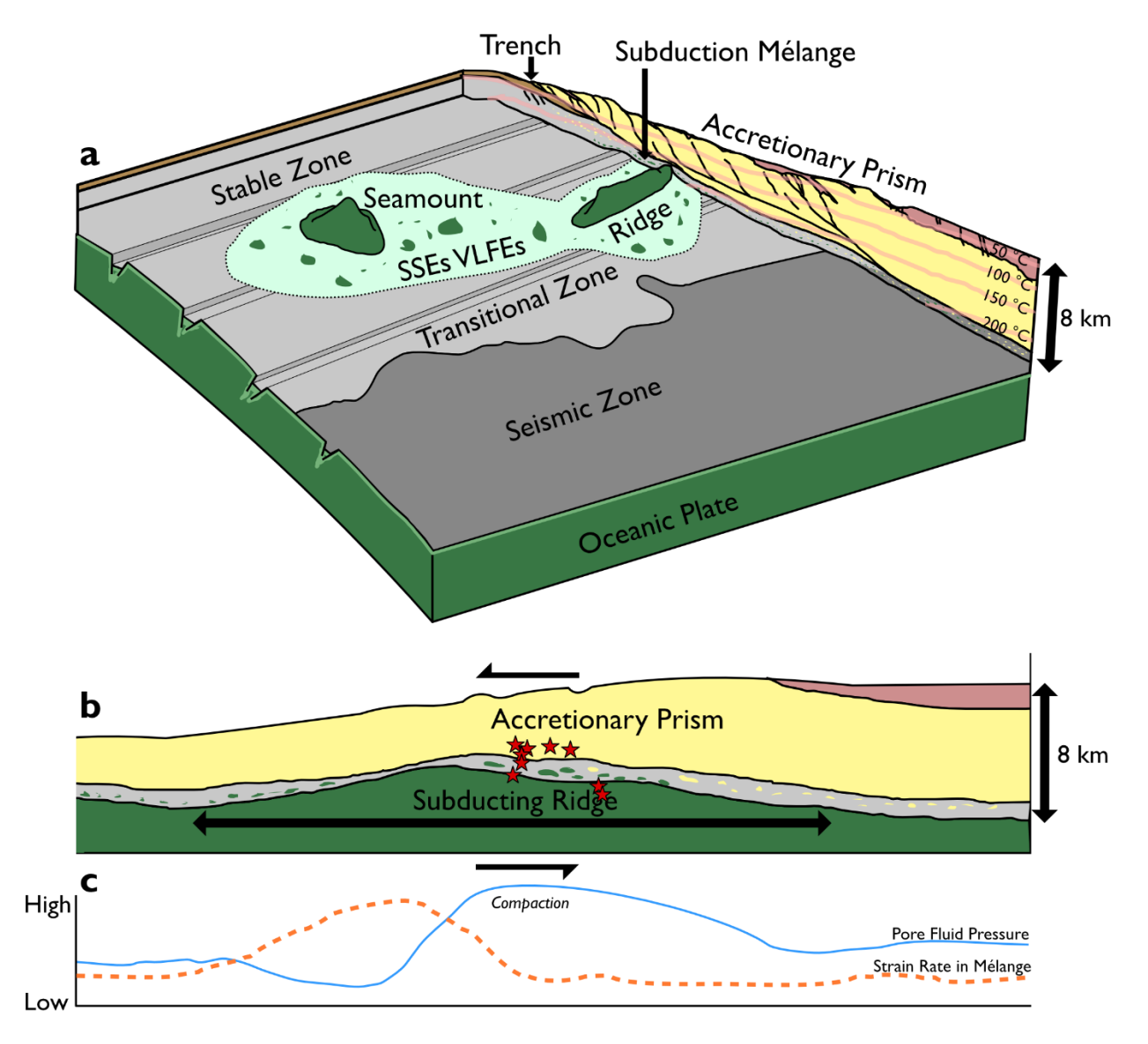


Figure 4-10: a) Schematic cartoon of the subduction interface (design after *Bilek and Lay* [2002], structure of accretionary prism after *Moore et al.* [2009], thermal structure after *Harris et al.* [2013]). Subducting seamounts and ridges are closely associated with shallow slow slip phenomena. The transition from stable to unstable likely reflects the change from velocity strengthening to velocity-weakening behavior in the shale with depth. b) Cross section of a subducting ridge in Nankai with no vertical exaggeration (after *Toh et al.* [2018] and *Park et al.* [2003]). Stars show localities of VLFEs. c) Schematic distribution of pore fluid pressures and strain-rates (assuming deformation is partitioned into the mélange) around the subducting ridge. Note that the zone of VLFEs occurs in a region with high pore fluid pressures (due to compaction on front of the downgoing ridge) and elevated strain rates in the matrix. The subducting ridge is

likely a source of basaltic blocks within the shale matrix of the mélange, which may promote slow slip phenomena.

the block model stress and strain-rate are directly linked. Slow slip events which propagate more slowly are less likely to cause failure of blocks, while faster slow slip events may raise the intensity of the tremor signal. We add complexity to the model through field observations of linked blocks, where smeared altered basalt along through going faults allows individual blocks to be connected. Horizons of basaltic blocks may then serve as a source for larger magnitude slow slip phenomena.

4.7.4 Relationship of Seamounts and Ridges to LFEs and VLFEs

In the shallow slow slip and tremor environment, slow slip and (V)LFEs are closely related to the margins of subducting seamounts and ridges [Saffer and Wallace, 2015; Todd et al., 2018; Toh et al., 2018; Shaddox and Schwartz, 2019]. It has previously been shown that subducting seamounts and ridges cause increases in fluid pressure and change the local stress state. These two factors promote slow slip phenomena. We hypothesize that subducting ridges and seamounts would also promote slow slip phenomena due to two additional effects. First, they would cause a strain-rate increase in the viscously deforming matrix along the edges of the subducting seamounts and ridges, therefore promoting more localized deformation (Figure 4-10b). Second, erosion of seamounts and ridges during subduction would produce blocks of velocity-weakening altered basalt which could be incorporated into the shale matrix (Figure 4-10). These eroded blocks could serve as nucleation points for slow slip phenomena in the shallow subduction environment.

4.8 Conclusions

Altered basaltic blocks from the Mugi mélange show evidence for localized frictional failure and cataclasis along their margins, with faults containing sheared basaltic cataclasite connecting individual blocks. We modeled stress concentrations produced by distributed shear in

the shale matrix and show that the resulting stress distribution predicts localized failure along block margins. Calculations of critical nucleation lengths for dynamic failure show that mapped basaltic blocks sit above the threshold for dynamic failure when pore fluid pressures are low, and below the threshold when pore fluid pressures are high. This indicates that block failure would transition from producing microseismic events to slow slip phenomena with increasing pore fluid pressure. Linked blocks may allow for larger magnitude slow slip phenomena to occur. Shallow slow slip phenomena occur preferentially along the margins of subducting ridges and seamounts, where slip rates and pore fluid pressures are expected to be elevated, and where altered basaltic blocks are more likely to be eroded into the shale matrix.

4.9 Acknowledgements

N.J.P. is supported by GSA Student Grant 11283-16, the Japan Society for the Promotion of Science KAKENHI grant JP16K21728, and an NSERC PGS-D, C.R. by an NSERC Discovery Grant and Canada Research Chair in Earthquake Geology, and K.U. by the Japan Society for the Promotion of Science KAKENHI grant JP16H06476.

4.10 References

- Ando, R., R. Nakata, and T. Hori (2010), A slip pulse model with fault heterogeneity for low-frequency earthquakes and tremor along plate interfaces, Geophys. Res. Lett., 37(L10310), 1–5, doi:10.1029/2010GL043056.
- Annoura, S., T. Hashimoto, N. Kamaya, and A. Katsumata (2017), Shallow episodic tremor near the Nankai Trough axis off southeast Mie prefecture, Japan, Geophys. Res. Lett., 44(8), 3564–3571, doi:10.1002/2017GL073006.
- Araki, E., D. M. Saffer, A. J. Kopf, L. M. Wallace, T. Kimura, Y. Machida, S. Ide, E. Davis, and IODP Expedition 365 Shipboard Scientists (2017), Recurring and triggered slow-slip events near the trench at the Nankai Trough subduction megathrust, Science (80-.)., 356, 1157–1160.

- Beall, A., Å. Fagereng, and S. Ellis (2019), Strength of Strained Two Phase Mixtures: Application to Rapid Creep and Stress Ampli fi cation in Subduction Zone Mélange Geophysical Research Letters, Geophys. Res. Lett., 46, 169–178, doi:10.1029/2018GL081252.
- Behr, W. M., A. J. Kotowski, and K. T. Ashley (2018), Dehydration-induced rheological heterogeneity and the deep tremor source in warm subduction zones, Geology, 46(5), 475–478.
- Beroza, G. C., and S. Ide (2011), Slow Earthquakes and Nonvolcanic Tremor, Annu. Rev. Earth Planet. Sci., 39(1), 271–296, doi:10.1146/annurev-earth-040809-152531.
- Bilek, S. L., and T. Lay (2002), Tsunami earthquakes possibly widespread manifestations of frictional conditional stability, Geophys. Res. Lett., 29(14), 18-1-18-4, doi:10.1029/2002gl015215.
- Bos, B., and C. J. Spiers (2002), Frictional-viscous flow of phyllosilicate-bearing fault rock: Microphysical model and implications for crustal strength profiles, J. Geophys. Res., 107, doi:10.1029/2001JB000301.
- Brodsky, E. E., C. D. Rowe, F. Meneghini, and J. C. Moore (2009), A geological fingerprint of low-viscosity fault fluids mobilized during an earthquake, J. Geophys. Res. Solid Earth, 114(1), 1–14, doi:10.1029/2008JB005633.
- Bürgmann, R. (2018), The geophysics, geology and mechanics of slow fault slip, Earth Planet. Sci. Lett., 495, 112–134, doi:10.1016/j.epsl.2018.04.062.
- Chestler, S. R., and K. C. Creager (2017), Evidence for a scale-limited low-frequency earthquake source process, J. Geophys. Res. Solid Earth, 122, 3099–3114, doi:10.1002/2016JB013717.
- Compton, K. E., J. D. Kirkpatrick, and G. J. Holk (2017), Tectonophysics Cyclical shear fracture and viscous fl ow during transitional ductile-brittle deformation in the Saddlebag Lake Shear Zone, California, Tectonophysics, 708, 1–14, doi:10.1016/j.tecto.2017.04.006.
- Cruz-Atienza, V. M., C. Villafuerte, and H. S. Bhat (2018), Rapid tremor migration and pore-pressure waves in subduction zones, Nat. Commun., 9(1), doi:10.1038/s41467-018-05150-3.

- den Hartog, S. A. M., and C. J. Spiers (2014), A microphysical model for fault gouge friction applied to subduction megathrusts, J. Geophys. Res. Solid Earth, 119, 1510–1529, doi:10.1002/2014JB011151.
- Dieterich, J. H. (1992), Earthquake nucleation on faults with rate- and state-dependent strength, Tectonophysics, 211, 115–134.
- Fagereng, Å. (2011), Frequency-size distribution of competent lenses in a block-in-matrix mélange: Imposed length scales of brittle deformation?, J. Geophys. Res., 116, doi:10.1029/2010JB007775.
- Fagereng, Å., and S. A. M. den Hartog (2017), Subduction megathrust creep governed by pressure solution and frictional-viscous flow, Nat. Geosci., 10, 51–57, doi:10.1038/NGEO2857.
- Fagereng, Å., G. W. B. Hillary, and J. F. a Diener (2014), Brittle-viscous deformation, slow slip, and tremor, Geophys. Res. Lett., 41(May), 4159–4167, doi:10.1002/2014GL060433.1.
- Fagereng, Å., J. F. A. Diener, F. Meneghini, C. Harris, and A. Kvadsheim (2017), Quartz vein formation by local dehydration embrittlement along the deep, tremorgenic subduction thrust interface, Geology, (1), 1–4.
- Gao, X., and K. Wang (2017), Rheological separation of the megathrust seismogenic zone and episodic tremor and slip, Nat. Publ. Gr., doi:10.1038/nature21389.
- Gerbi, C., S. E. Johnson, A. Cook, and S. S. Vel (2015), Effect of phase morphology on bulk strength for power-law materials, Geophys. J. Int., 200(1), 374–389, doi:10.1093/gji/ggu388.
- Grigull, S., A. Krohe, C. Moos, S. Wassmann, and B. Stöckhert (2012), "Order from chaos": A field-based estimate on bulk rheology of tectonic mélanges formed in subduction zones, Tectonophysics, 568–569, 86–101, doi:10.1016/j.tecto.2011.11.004.
- Handy, M. R. (1994), Flow laws for rocks containing two non-linear viscous phases: A phenomenological approach, J. Struct. Geol., 16(3), 287–301, doi:10.1016/0191-8141(94)90035-3.

- Harris, R., M. Yamano, M. Kinoshita, G. Spinelli, H. Hamamoto, and J. Ashi (2013), A synthesis of heat flow determinations and thermal modeling along the Nankai Trough, Japan, J. Geophys. Res. Solid Earth, 118, 2687–2702, doi:10.1002/jgrb.50230.
- Hashimoto, Y., N. Doi, and T. Tsuji (2013), Difference in acoustic properties at seismogenic fault along a subduction interface: Application to estimation of effective pressure and fluid pressure ratio, Tectonophysics, 600, 134–141, doi:10.1016/j.tecto.2013.03.016.
- Hayman, N. W., and L. L. Lavier (2014), The geologic record of deep episodic tremor and slip, Geology, 42(3), 195–198, doi:10.1130/G34990.1.
- Huet, B., P. Yamato, and B. Grasemann (2014), The Minimized Power Geometric model: An analytical mixing model for calculating polyphase rock viscosities consistent, J. Geophys. Res. Solid Earth, 119, 3897–3924, doi:10.1002/2013JB010453.
- Hyndman, R. D., M. Yamano, and D. A. Oleskevich (1997), The Seismogenic Zone of Subduction Thrust Faults, Isl. Arc, 6, 244–260, doi:10.1785/gssrl.79.4.572.
- Ikesawa, E., G. Kimura, K. Sato, K. Ikehara-Ohmori, Y. Kitamura, A. Yamaguchi, K. Ujiie, and Y. Hashimoto (2005), Tectonic incorporation of the upper part of oceanic crust to overriding plate of a convergent margin: An example from the Cretaceous–early Tertiary Mugi Mélange, the Shimanto Belt, Japan, Tectonophysics, 401, 217–230, doi:10.1016/j.tecto.2005.01.005.
- Ito, Y., and K. Obara (2006a), Dynamic deformation of the accretionary prism excites very low frequency earthquakes, Geophys. Res. Lett., 33, doi:10.1029/2005GL025270.
- Ito, Y., and K. Obara (2006b), Very low frequency earthquakes within accretionary prisms are very low stress-drop earthquakes, Geophys. Res. Lett., 33(9), 1–4, doi:10.1029/2006GL025883.
- Ito, Y., K. Obara, T. Matsuzawa, and T. Maeda (2009), Very low frequency earthquakes related to small asperities on the plate boundary interface at the locked to aseismic transition, J. Geophys. Res., 114(B00A13), 1–16, doi:10.1029/2008JB006036.
- Kawabata, K., H. Tanaka, and G. Kimura (2007), Mass transfer and pressure solution in deformed shale of accretionary complex: Examples from the Shimanto Belt, southwestern Japan, J. Struct. Geol., 29(4), 697–711, doi:10.1016/j.jsg.2006.11.009.

- Kawabata, K., H. Tanaka, Y. Kitamura, and K. F. Ma (2009), Apparent activation energy and rate-limiting process estimation from natural shale deformed by pressure solution in shallow subduction zone, Earth Planet. Sci. Lett., 287(1–2), 57–63, doi:10.1016/j.epsl.2009.07.032.
- Kimura, G., Y. Kitamura, Y. Hashimoto, A. Yamaguchi, T. Shibata, K. Ujiie, and S. Okamoto (2007), Transition of accretionary wedge structures around the up-dip limit of the seismogenic subduction zone, Earth Planet. Sci. Lett., 255(3–4), 471–484, doi:10.1016/j.epsl.2007.01.005.
- Kimura, G., A. Yamaguchi, M. Hojo, Y. Kitamura, J. Kameda, K. Ujiie, Y. Hamada, M. Hamahashi, and S. Hina (2012), Tectonic mélange as fault rock of subduction plate boundary, Tectonophysics, 568–569, 25–38, doi:10.1016/j.tecto.2011.08.025.
- Kitamura, Y. et al. (2005), Mélange and its seismogenic roof décollement: A plate boundary fault rock in the subduction zone An example from the Shimanto Belt, Japan, Tectonics, 24(5), 1–15, doi:10.1029/2004TC001635.
- Kotowski, A. J., and W. M. Behr (2019), Length scales and types of heterogeneities along the deep subduction interface: Insights from exhumed rocks on Syros Island, Greece, Geosphere, 15, 1–28, doi:10.1130/GES02037.1/4782963/ges02037.pdf.
- Mariani, E., K. H. Brodie, and E. H. Rutter (2006), Experimental deformation of muscovite shear zones at high temperatures under hydrothermal conditions and the strength of phyllosilicate-bearing faults in nature, J. Struct. Geol., 28(9), 1569–1587, doi:10.1016/j.jsg.2006.06.009.
- Mcguire, J. J., J. A. Collins, E. Davis, K. Becker, and M. Heesemann (2018), A Lack of Dynamic Triggering of Slow Slip and Tremor Indicates That the Shallow Cascadia Megathrust Offshore Vancouver Island Is Likely Locked, Geophys. Res. Lett., 45, 11,095-11,103, doi:10.1029/2018GL079519.
- Montési, L. G. J. (2007), A constitutive model for layer development in shear zones near the brittle-ductile transition, Geophys. Res. Lett., 34(8), 1–5, doi:10.1029/2007GL029250.
- Moore, G. F. et al. (2009), Structural and seismic stratigraphic framework of the NanTroSEIZE Stage 1 transect, Proc. Integr. Ocean Drill. Progr., 314/315/31, 1–46, doi:10.2204/iodp.proc.314315316.102.2009.

- Nakano, M., T. Hori, E. Araki, S. Kodaira, and S. Ide (2018), Shallow very-low-frequency earthquakes accompany slow slip events in the Nankai subduction zone, Nat. Commun., 9(984), 1–8, doi:10.1038/s41467-018-03431-5.
- Obara, K. (2002), Nonvolcanic Deep Tremor Associated with Subduction in Southwest Japan, Science (80-.)., 296, 1679–1682.
- Obara, K., and A. Kato (2016), Connecting slow earthquakes to huge earthquakes, Science (80-.)., 353(6296), 253–258.
- Ohmori, K., A. Taira, H. Tokuyama, A. Sakaguchi, M. Okamura, and A. Aihara (1997), Paleothermal structure of the Shimanto accretionary prism, Shikoku, Japan: Role of an out-of-sequence thrust, Geology, 25(4), 327–330, doi:10.1130/0091-7613(1997)025<0327:PSOTSA>2.3.CO;2.
- Ohnaka, M. (2000), A Physical Scaling Relation Between the Size of an Earthquake and its Nucleation Zone Size, Pure Appl. Geophys., 157, 2259–2282.
- Okubo, P. G., and J. H. Dieterich (1984), Effects of physical fault properties on frictional instabilities produced on simulated faults, J. Geophys. Res., 89(B7), 5817–5827, doi:10.1029/JB089iB07p05817.
- Oleskevich, D. a., R. D. Hyndman, and K. Wang (1999), The updip and downdip limits to great subduction earthquakes: Thermal and structural models of Cascadia, south Alaska, SW Japan, and Chile, J. Geophys. Res. Solid Earth, 104(B7), 14965–14991, doi:10.1029/1999JB900060.
- Park, J. O., G. F. Moore, T. Tsuru, S. Kodaira, and Y. Kaneda (2003), A subducted oceanic ridge influencing the Nankai megathrust earthquake rupture, Earth Planet. Sci. Lett., 217, 77–84, doi:10.1016/S0012-821X(03)00553-3.
- Passchier, C. W., and R. A. J. Trouw (2005), Microtectonics, 2nd ed., Springer, Berlin.
- Phillips, N. J., C. D. Rowe, and K. Ujiie (2019), For how long are pseudotachylytes strong? Rapid alteration of basalt-hosted pseudotachylytes from a shallow subduction complex, Earth Planet. Sci. Lett., 518, 108–115, doi:10.1016/j.epsl.2019.04.033.

- Rogers, G., and H. Dragert (2003), Episodic Tremor and Slip on the Cascadia Subduction Zone: The Chatter of Silent Slip, Science (80-.)., 300, 1942–1944.
- Rowe, C. D., F. Meneghini, and J. C. Moore (2011), Textural record of the seismic cycle: strain-rate variation in an ancient subduction thrust, Geol. Soc. London, Spec. Publ., 359, 77–95, doi:10.1144/SP359.5.
- Rowe, C. D., J. C. Moore, and F. Remitti (2013), The thickness of subduction plate boundary faults from the seafloor into the seismogenic zone, Geology, 41(9), 991–994, doi:10.1130/G34556.1.
- Rubin, A. M., and J. Ampuero (2005), Earthquake nucleation on (aging) rate and state faults, J. Geophys. Res., 110(B11312), 1–24, doi:10.1029/2005JB003686.
- Saffer, D. M., and L. M. Wallace (2015), The frictional, hydrologic, metamorphic and thermal habitat of shallow slow earthquakes, Nat. Geosci., 8(8), 594–600, doi:10.1038/ngeo2490.
- Sakaguchi, A. (1996), High paleogeothermal gradient with ridge subduction beneath the Cretaceous Shimanto accretionary prism, southwest Japan, Geology, 24(9), 795–798, doi:10.1130/0091-7613(1996)024<0795.
- Scuderi, M. M., and C. Collettini (2016), The role of fluid pressure in induced vs. triggered seismicity: insights from rock deformation experiments on carbonates, Sci. Rep., 6(24852), 1–9, doi:10.1038/srep24852.
- Shaddox, H. R., and S. Y. Schwartz (2019), Subducted seamount diverts shallow slow slip to the forearc of the northern Hikurangi subduction zone, New Zealand, Geology, 47(5), 415–418.
- Shelly, D. R., G. C. Beroza, S. Ide, and S. Nakamula (2006), Low-frequency earthquakes in Shikoku, Japan, and their relationship to episodic tremor and slip., Nature, 442(7099), 188–191, doi:10.1038/nature04931.
- Shelly, D. R., G. C. Beroza, and S. Ide (2007), Non-volcanic tremor and low-frequency earthquake swarms., Nature, 446(7133), 305–307, doi:10.1038/nature05666.

- Shibata, T., Y. Orihashi, G. Kimura, and Y. Hashimoto (2008), Underplating of mélange evidenced by the depositional ages: U-Pb dating of zircons from the Shimanto accretionary complex, southwest Japan, Isl. Arc, 17(3), 376–393, doi:10.1111/j.1440-1738.2008.00626.x.
- Skarbek, R. M., A. W. Rempel, and D. A. Schmidt (2012), Geologic heterogeneity can produce aseismic slip transients, Geophys. Res. Lett., 39(L21306), 1–5, doi:10.1029/2012GL053762.
- Stockhert, B. (2002), Stress and deformation in subduction zones: insight from the record of exhumed metamorphic rocks, Geol. Soc. London Spec. Publ., 200, 255–274.
- Stöckhert, B., M. Wachmann, M. Küster, and S. Bimmermann (1999), Low effective viscosity during high pressure metamorphism due to dissolution precipitation creep: The record of HP-LT metamorphic carbonates and siliciclastic rocks from Crete, Tectonophysics, 303(1–4), 299–319, doi:10.1016/S0040-1951(98)00262-5.
- Tarling, M. S., and C. D. Rowe (2015), Shear strain distribution in scaly fabrics, Submitted.
- Thomas, A. M., G. C. Beroza, and D. R. Shelly (2016), Constraints on the source parameters of low-frequency earthquakes on the San Andreas Fault, Geophys. Res. Lett., 43, 1–8, doi:10.1002/2015GL067173.
- Todd, E. K. et al. (2018), Earthquakes and Tremor Linked to Seamount Subduction During Shallow Slow Slip at the Hikurangi Margin, New Zealand, J. Geophys. Res. Solid Earth, 123, 6769–6783, doi:10.1029/2018JB016136.
- Toh, A., K. Obana, and E. Araki (2018), Distribution of very low frequency earthquakes in the Nankai accretionary prism influenced by a subducting-ridge, Earth Planet. Sci. Lett., 482(March 2011), 342–356, doi:10.1016/j.epsl.2017.10.062.
- Trepmann, C. A., and B. Stöckhert (2009), Microfabric of folded quartz veins in metagreywackes: Dislocation creep and subgrain rotation at high stress, J. Metamorph. Geol., 27, 555–570, doi:10.1111/j.1525-1314.2009.00842.x.
- Tullis, T. E., F. G. Horowitz, and J. Tullis (1991), Flow Laws of Polyphase Aggregates from End-Member Flow Laws, J. Geophys. Res., 96(B5), 8081–8096.

- Uchida, N., T. Iinumi, R. Nadeau, R. Bürgmann, and R. Hino (2016), Periodic slow slip triggers megathrust earthquakes in northeastern Japan, Science (80-.)., 351(6272), 488–492.
- Uenishi, K., and J. R. Rice (2003), Universal nucleation length for slip-weakening rupture instability under nonuniform fault loading, J. Geophys. Res., 108(B1), doi:10.1029/2001JB001681.
- Ujiie, K., A. Yamaguchi, G. Kimura, and S. Toh (2007), Fluidization of granular material in a subduction thrust at seismogenic depths, Earth Planet. Sci. Lett., 259, 307–318, doi:10.1016/j.epsl.2007.04.049.
- Ujiie, K., H. Saishu, Å. Fagereng, N. Nishiyama, M. Otsubo, H. Masuyama, and H. Kagi (2018), An Explanation of Episodic Tremor and Slow Slip Constrained by Crack-Seal Veins and Viscous Shear in Subduction Mélange, Geophys. Res. Lett., 45(11), 5371–5379, doi:10.1029/2018GL078374.
- Violay, M., B. Gibert, D. Mainprice, B. Evans, J. M. Dautria, P. Azais, and P. Pezard (2012), An experimental study of the brittle-ductile transition of basalt at oceanic crust pressure and temperature conditions, J. Geophys. Res. Solid Earth, 117(3), 1–23, doi:10.1029/2011JB008884.
- Voss, N., T. H. Dixon, Z. Liu, R. Malservisi, M. Protti, and S. Schwartz (2018), Do slow slip events trigger large and great megathrust earthquakes?, Sci. Adv., 4, 1–6.
- Wech, A. G., and N. M. Bartlow (2014), Slip rate and tremor genesis in Cascadia, Geophys. Res. Lett., 41, 392–398, doi:10.1002/2014GL061184.

CONCLUSIONS

Active subduction zones were frequently divided into locked and creeping zones, thought to be controlled by the changes in rheologies of subducting lithologies with increasing metamorphic grade. In the past 15 years, increasingly dense deployments of seismometers, pressure gauges, and global positioning systems on continents and ocean floors has led to the discovery of transitional zones, where slow earthquakes and tremor accommodate deformation. At the updip limit of seismogenic zones, seismic events propagating to the trench, slow slip events, and tremor all frequently occur.

This thesis addresses two fundamental questions on shallow subduction zones. First, earthquake nucleation and propagation requires velocity weakening materials (for both regular and slow earthquakes); however, deformation experiments to date on common subducting lithologies (shale, carbonate, gabbro, basalt) record velocity-strengthening behavior at the updip limit of the seismogenic zone. I performed triaxial friction experiments on natural samples from the Mugi melange to test the frictional properties of natural subducting materials at the updip limit of the seismogenic zone.

Second, models of slow slip phenomena in transitional zones requires either mixing of velocity-weakening and velocity-strengthening materials, or finely tuned length scales of velocity-weakening materials. Detailed mapping of exhumed subduction fault rocks in this study has led to the first reported discovery of a basaltic pseudotachylyte (an ancient earthquake), which occurred along the upper margin of an altered basaltic slab. Additionally, well developed cataclasites and slip surfaces are documented along the margins of altered basaltic blocks. These observations led to the hypothesis that altered basalt may be a velocity weakening material which could host unstable slip.

Deformation experiments on natural altered basalt and shale, at the *in situ* conditions of deformation for the updip limit of seismogenic zones, has shown that altered basalt, a ubiquitous material along the subduction interface, is velocity-weakening and will preferentially host localized deformation, consistent with the field observations. Calculations of critical nucleation lengths for dynamic slip have shown that mapped basaltic blocks would produce microseismic earthquakes at low pore fluid pressures, while at near-lithostatic pore fluid pressures, the blocks sit near the condition for stability and may produce LFEs or VLFEs. Faults containing discontinuous seams of basaltic cataclasite link blocks together, and may allow for large magnitude VLFEs by increasing the source region. Stress concentrations around basaltic blocks cause frictional failure in the blocks during distributed deformation in the shale matrix. Together these observations provide a new field based framework for linking nucleation length scales to rupture patch size along the subduction interface.

Together this work presents altered basalt as an important velocity-weakening lithology at the updip limit of the seismogenic zone. Future experiments on frictional behavior need to account for metasomatic and metamorphic reactions during subduction, which may change the rate-and-state properties of subducting lithologies. These reactions can be constrained by field observations of exhumed subduction zones from varying depths and from metamorphic modelling.

APPENDIX A

Supplementary Materials for Chapter 2

This supplement contains 2 additional figures (A1 & A2), which were used as part of the microstructural analysis in Chapter 2.

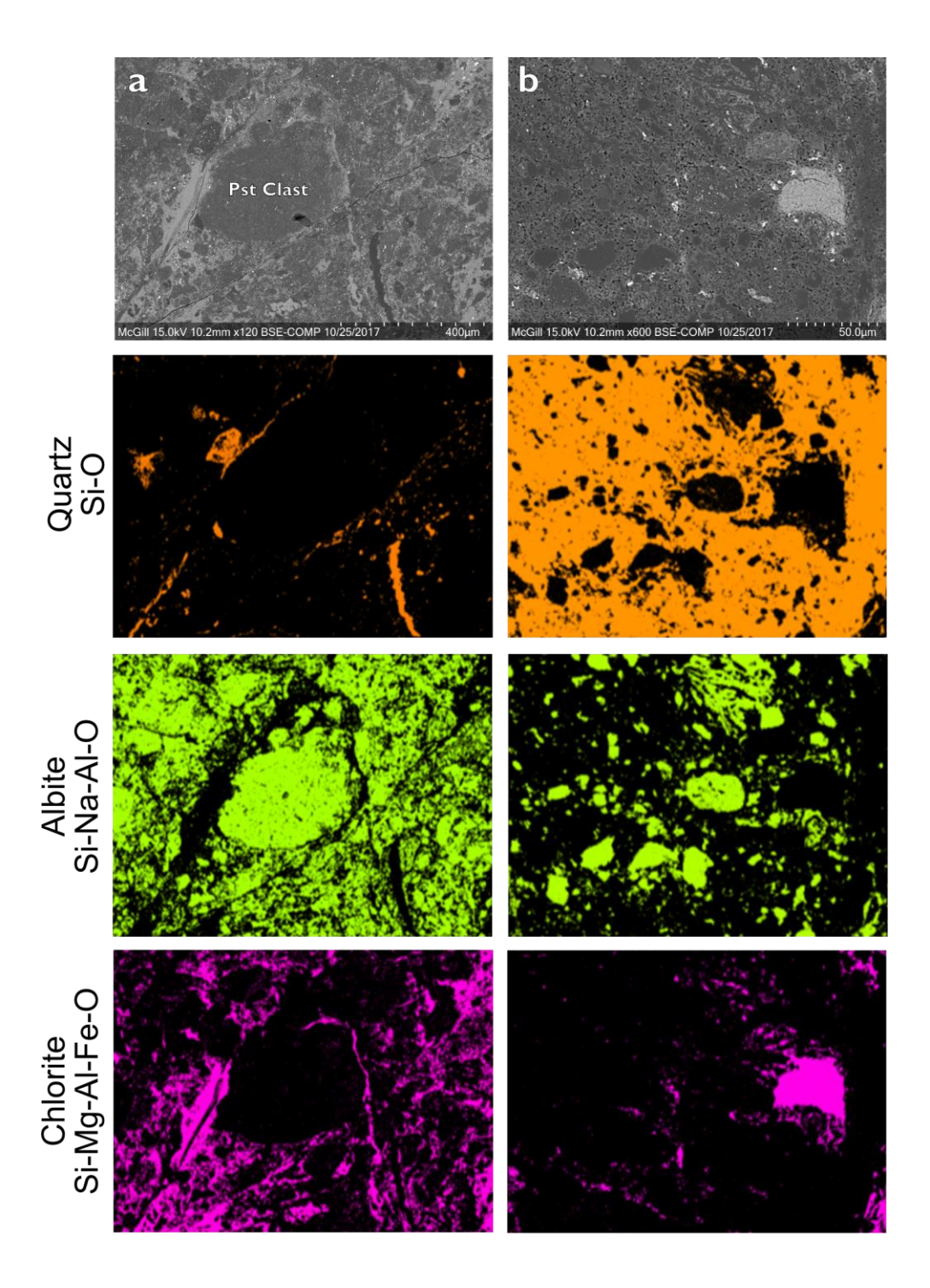


Figure A1: Phase maps from EDS maps of the clast-bearing cataclasite (note that these are based on major element data, and "albite" may be a glass with an albitic composition or crystals of albite).

a) Fractured pseudotachylyte clasts with an albitic composition surrounded by a chlorite gouge. b) Interior of a silicified-clast showing 72% silica. Clasts of chlorite and albite preserved within the

silicified gouge demonstrate that gouge formation and silicification occurred near peak metamorphic conditions during subduction.

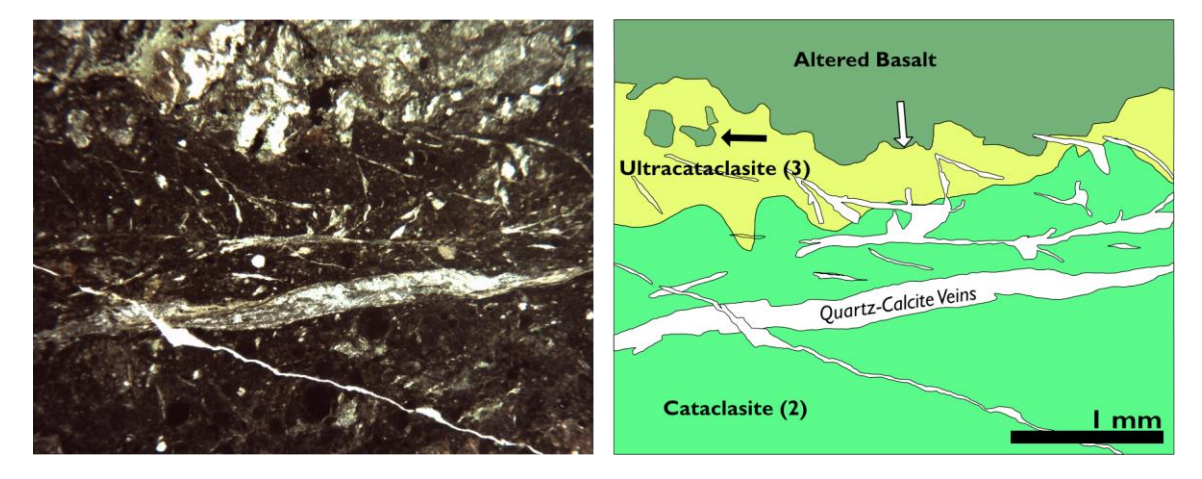


Figure A2: Photomicrograph and interpretation of the pseudotachylyte bearing fault. Veins cutting through the pseudotachylyte bearing fault are evidence for late fluid flow. Early veins form parallel with the slip direction while late veins cross-cut all phases of deformation indicating that they formed after the fault. The contact between the altered basalt and ultracataclasite (white arrow) has eroded and embayed margins, and fragments of altered basalt are found in the ultracataclasite (black arrow) indicating that faulting postdates alteration of the basalt.

APPENDIX B

Supplementary Materials for Chapter 3

Contents of Supplement B

This appendix contains 3 additional figures (B1-B3) depicting microstructural information, 1 figure (B4) showing a comparison between different fits of grain size distributions to accompany Table B2, and 1 figure (B5) showing comparing Reitveld results between fresh and altered basalt. All fits (using both aging and slip laws) to rate-steps between 0.28 and 2.8 μ m/s are included in Table B1. Table B2 compares power law fits using least squares regression and maximum likelihood methods.

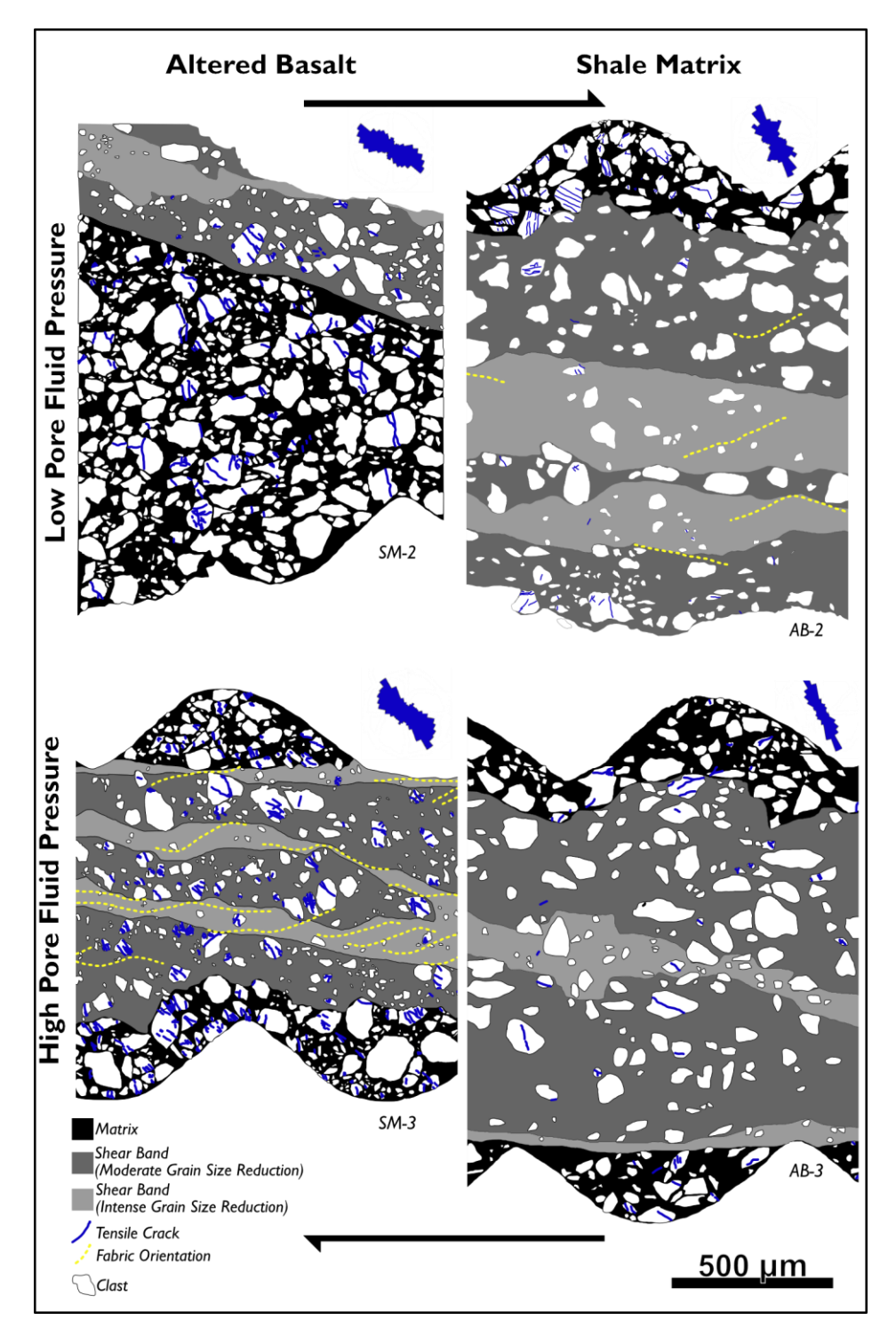


Figure B1: Fabrics observed in polished pucks using backscattered electron microscopy. Blue rose diagrams show the preferred orientation of tensile fractures (blue lines) determined using the directionality tool in imageJ, which uses fourier component analysis to analyze the directionality of each pixel in the tensile fractures..

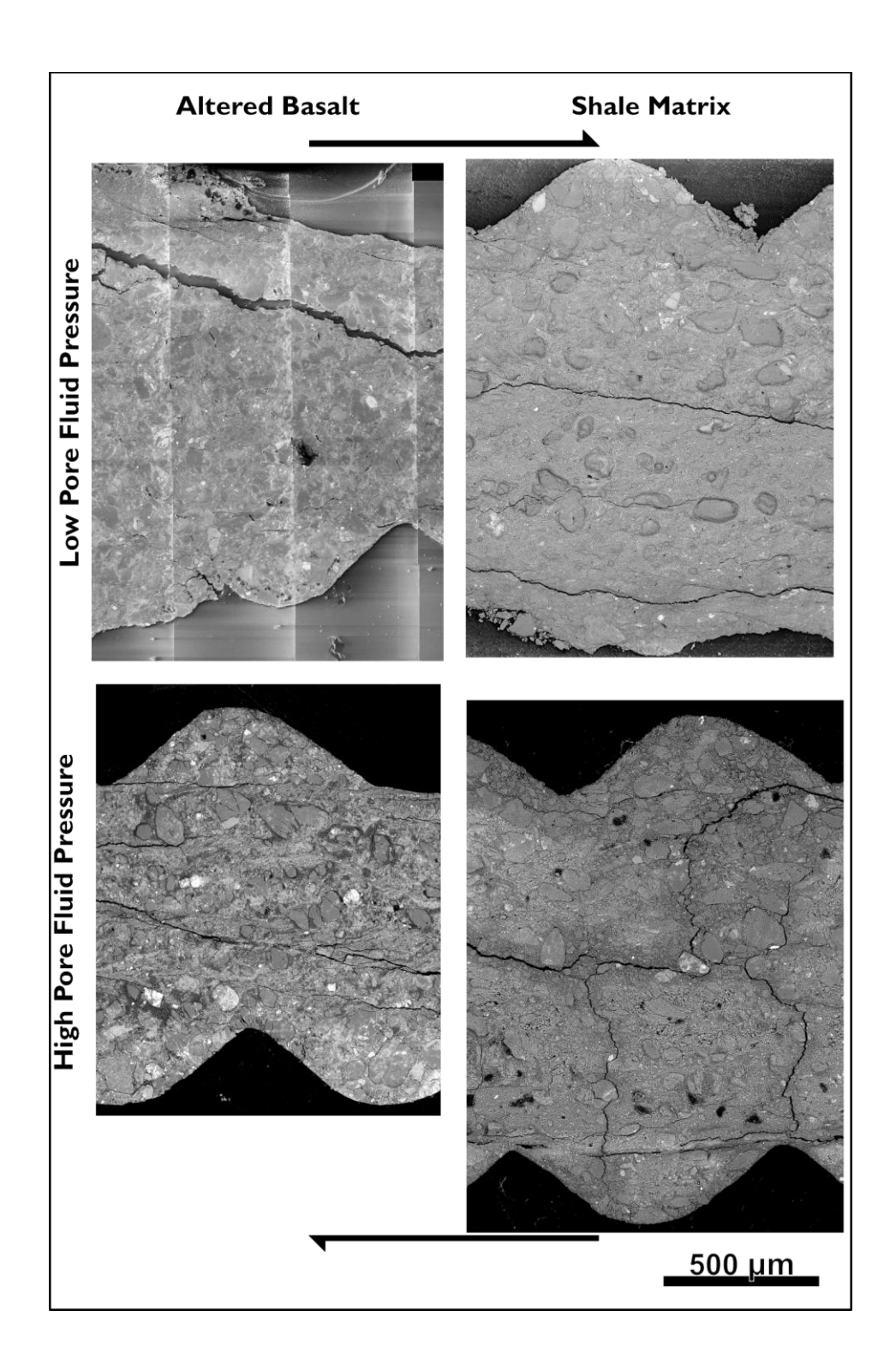


Figure B2: Un-annotated SEM photomicrographs used in the determination of fabrics and tensile cracks for Figure B1.

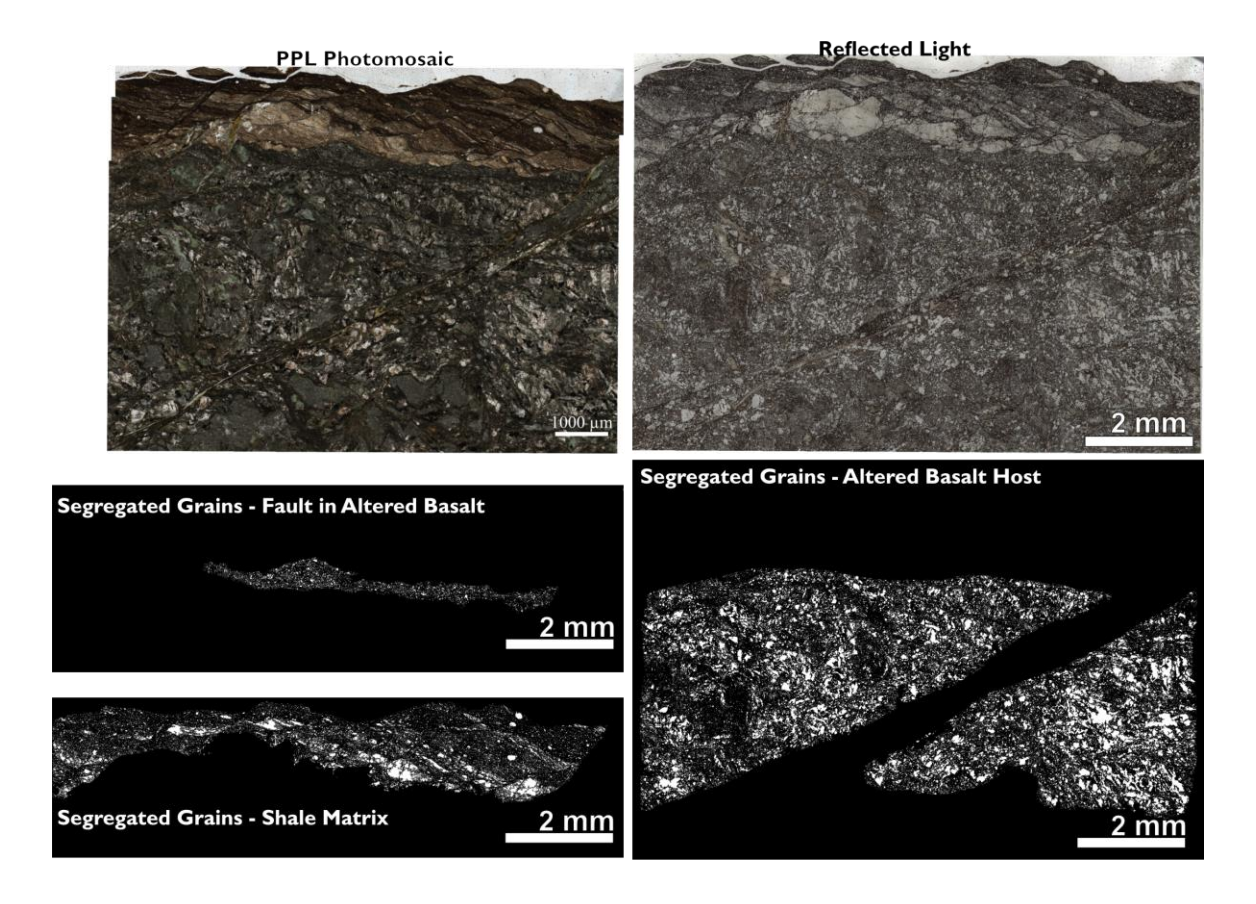


Figure B3: Plane polarized light and reflected light photomosaics of the natural microstructures analyzed in this study (from Figure 3-1b). Segregated grains for the natural fault in altered basalt, the shale matrix, and the altered basalt (host) are all sources from the reflected light image.

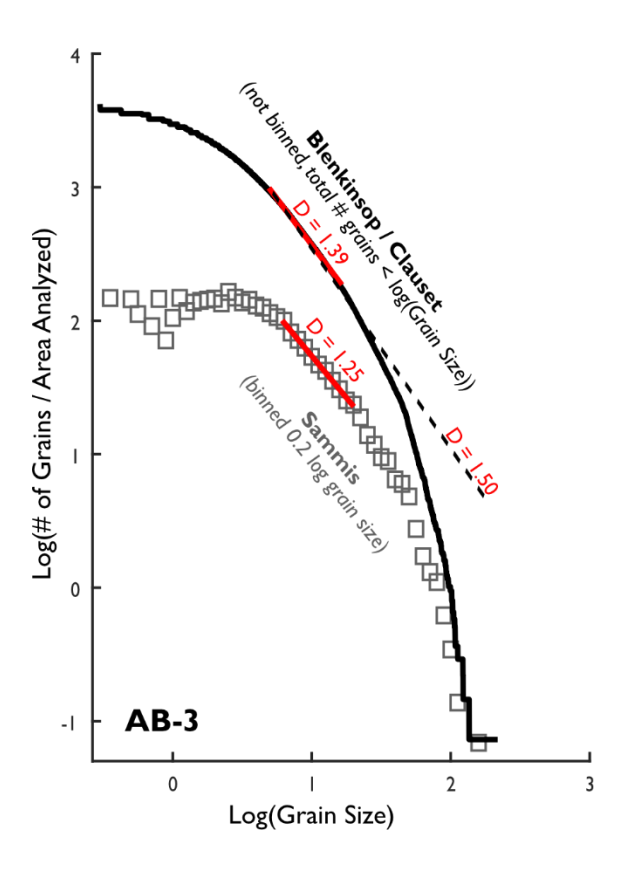


Figure B4: Comparison between fits from previous studies. We plot the data from AB-3 using the Blenkinsop [1991] continuous data and the binned data in the style of Sammis [1989]. Fits using least squares regression are plotted in red, and the dashed line shows the fit using maximum likelihood.

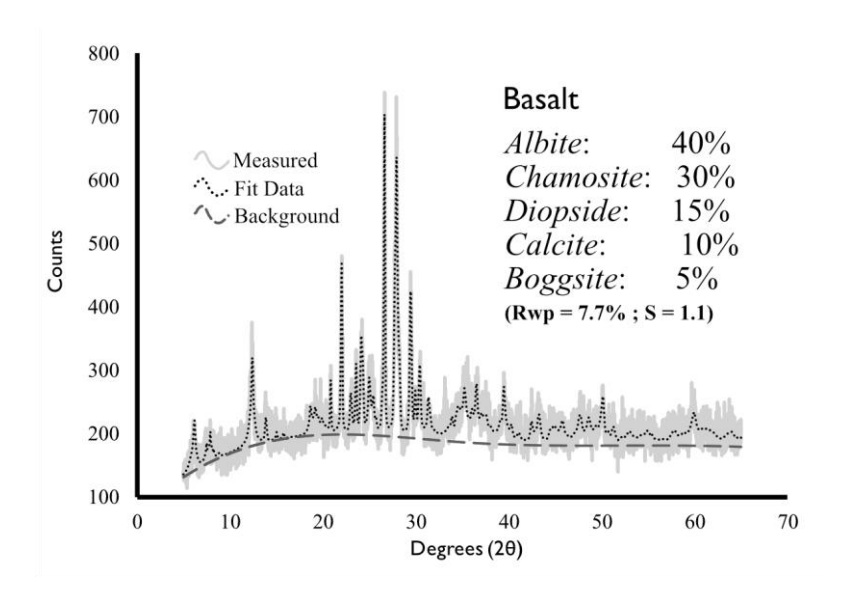


Figure B5. Reitveld results from XRD on fresh basalt from the Mugi Mélange.

AGING	mu	error	a	error	b	error	dc	error	stiff	a-b	error
AB-1 (2 to 0.2)	0.60	1.1E-04	0.0090	1.3E-04	0.015	8.5E-05	147	3.8E+00	0.63	-0.0057	1.6E-04
AB-1 (0.2 to 2)	0.63	2.3E-05	0.0049	1.3E-04	0.009	1.2E-04	63	1.6E+00	0.63	-0.0040	1.7E-04
AB-1 (2 to 0.2)	0.65	9.7E-05	0.0116	1.4E-04	0.013	1.1E-04	68	1.4E+00	0.63	-0.0011	1.8E-04
AB-2 (2 to 0.2)	0.64	5.6E-05	0.0082	7.1E-05	0.013	4.8E-05	119	1.6E+00	0.63	-0.0049	8.6E-05
AB-2 (0.2 to 2)	0.69	2.2E-05	0.0059	1.5E-04	0.009	1.4E-04	45	1.0E+00	0.63	-0.0033	2.0E-04
AB-3 (2 to 0.2)	0.60	8.5E-05	0.0097	1.3E-04	0.012	1.2E-04	42	7.1E-01	0.63	-0.0025	1.7E-04
AB-3 (0.2 to 2)	0.62	2.5E-05	0.0067	2.0E-04	0.010	2.0E-04	29	6.9E-01	0.63	-0.0035	2.9E-04
SM-1 (2 to 0.2)	0.51	9.3E-05	0.0091	8.8E-05	0.005	5.7E-05	216	1.2E+01	0.63	0.0040	1.0E-04
SM-1 (0.2 to 2)	0.50	2.8E-05	0.0054	1.2E-04	-0.003	9.3E-03	150	5.3E+02	0.63	0.0080	9.3E-03
SM-1 (2 to 0.2)	0.54	7.9E-05	0.0078	1.1E-04	-0.001	1.2E-04	14576	2.5E+03	0.63	0.0090	1.6E-04
SM-2 (2 to 0.2)	0.48	8.0E-05	0.0094	7.6E-05	0.004	2.2E-04	400	1.5E+02	0.63	0.0053	2.3E-04
SM-2 (0.2 to 2)	0.50	2.9E-05	0.0073	1.2E-04	-0.001	5.2E-02	100	6.1E+03	0.63	0.0082	5.2E-02
SM-3 (2 to 0.2)	0.48	8.0E-05	0.0079	9.8E-05	-0.002	1.1E-04	5477	6.4E+02	0.63	0.0095	1.5E-04
SM-3 (0.2 to 2)	0.47	2.1E-05	0.0084	9.7E-05	-0.002	1.4E-02	100	8.8E+02	0.63	0.0099	1.4E-02
SLIP											
AB-1 (2 to 0.2)	0.60	1.1E-04	0.0083	1.2E-04	0.013	8.9E-05	69	9.8E-01	0.63	-0.0048	1.5E-04
AB-1 (0.2 to 2)	0.63	2.2E-05	0.0055	1.4E-04	0.010	1.2E-04	111	4.2E+00	0.63	-0.0044	1.9E-04
AB-1 (2 to 0.2)	0.65	9.4E-05	0.0106	1.3E-04	0.012	1.0E-04	45	6.6E-01	0.63	-0.0010	1.6E-04
AB-2 (2 to 0.2)	0.64	5.8E-05	0.0073	6.8E-05	0.012	5.1E-05	62	4.9E-01	0.63	-0.0044	8.5E-05
AB-2 (0.2 to 2)	0.69	2.2E-05	0.0066	1.6E-04	0.010	1.4E-04	75	2.3E+00	0.63	-0.0036	2.1E-04
AB-3 (2 to 0.2)	0.60	9.0E-05	0.0085	1.3E-04	0.011	1.2E-04	27	4.0E-01	0.63	-0.0025	1.8E-04
AB-3 (0.2 to 2)	0.62	2.5E-05	0.0076	2.1E-04	0.011	2.1E-04	46	1.3E+00	0.63	-0.0036	3.0E-04
SM-1 (2 to 0.2)	0.51	9.2E-05	0.0091	8.3E-05	0.005	5.5E-05	133	5.0E+00	0.63	0.0041	9.9E-05
SM-1 (0.2 to 2)	0.50	2.8E-05	0.0047	1.8E-04	-0.001	2.0E-04	150	3.2E+01	0.63	0.0061	2.7E-04
SM-1 (2 to 0.2)	0.54	7.9E-05	0.0085	6.0E-05	-17.508	4.1E+02	4163440	9.8E+07	0.63	17.5160	4.1E+02
SM-2 (2 to 0.2)	0.48	7.9E-05	0.0094	7.1E-05	0.004	5.8E-04	400	2.0E+02	0.63	0.0050	5.9E-04
SM-2 (0.2 to 2)	0.50	2.8E-05	0.0058	2.9E-04	0.000	2.8E-04	45	8.3E+00	0.63	0.0060	4.0E-04
SM-3 (2 to 0.2)	0.48	7.1E-05	0.0085	5.5E-05	-2.239	1.8E+01	392363	3.1E+06	0.63	2.2475	1.8E+01
SM-3 (0.2 to 2)	0.47	2.1E-05	0.0076	1.5E-04	0.000	1.3E-04	100	1.2E+01	0.63	0.0078	1.9E-04

Table B1: Calculated rate-and-state parameters for each rate step between 0.28 and 2.8 $\mu m/s$ using both aging and slip laws.

xmin (not binned)	Blenk Best r ² (not binned)	Best D (not binned)	xmin (binned)	Best r ² (binned)	Best D (binned)	xmin	D values (Clauset)	ф	xmin	D values (Clauset)	Number of Grains 3-10 um	Number of Grains > 10 um	Area Analyzed (mm^2)	Area of Grains (%)		
1.39	0.9993	2.01	0.9	0.9935	1.57	9	1.76	0	7.9	1.73	4323	1145	4.01	17.6	AB2-W	EXPERIN
0.88	0.9992	1.35	0.7	0.9854	1.05	9	1.62	0.07	12.79	1.86	1183	380	0.97	25.5	AB2-M	EXPERIMENTAL SAMPLES
1.36	0.9987	2.15	0.85	0.9878	1.68	9	1.89	 0.08	8.69	1.88	 2530	602	2.65	13.3	AB2-SB	AMPLES
0.88	0.9988	1.39	0.8	0.9974	1.25	9	1.71	 0	5.23	1.5	 16579	5024	14.51	20.1	AB3-W	
0.88	0.9985	1.34	0.8	0.9958	1.19	9	1.67	 0	5.23	1.46	 12405	4019	9.29	25.7	АВЗ-М	
0.85	0.9986	1.70	0.7	0.9835	1.42	9	2.07	 0	5.98	1.88	 3790	772	4.15	9.1	AB3-SB	
1.15	0.9997	1.87	0.85	0.9965	1.72	9	1.95	 0	13.24	2.14	16806	3753	21.09	10	SM2-W	
1.16	0.9996	1.91	0.85	0.9947	1.7	9	1.98	 0	8.07	1.95	12182	2670	13.25	11	SM2-M	
0.96	0.9989	1.80	0.8	0.9904	1.75	9	2.07	0.45	9.7	2.3	4041	821	6.57	6.8	SM2-SB	
1.17	0.9983	2.06	0.7	0.9983	1.41	9	2.13	0	7.19	2.03	3828	800	9.99	4.1	SM3-W	
1.20	0.9983	2.13	0.7	0.9783	1.44	9	2.03	0	6.6	1.91	2304	478	2.71	5.7	SM3-M	
0.88	0.9993	1.62	0.6	0.9408	1.41	9	2.18	0.6	19.63	2.87	1411	293	6.2	3.8	SM3-SB	
1.37	0.9983	3.00	0.4	0.9893	0.86	9	2.43	 0.31	13.15	3.16	 4218	799	2.23	15.7	AB-F	NATL
7 1.13	33 0.9999) 1.53	0.95	93 0.9978	5 1.475	9	3 1.62	 0	5 6	5 1.55	 8 41523	10325	36.6	7 25.6	: AB-B	NATURAL SAMPLES
3 1.07	0.9996	1.98	0.9	78 0.9967	5 2.11	9	2.16	 0.02	7.67	2.13	 3 18745	5 3026	5 11.4	5 19.2	SM SM	IPLES

NATURAL SAMPLES

Table B2: Comparison between data fit using least squares regression (both binned and not binned; Figure B4) with the data fit using maximum likelihood (Clauset).

APPENDIX C

Supplementary Materials for Chapter 4

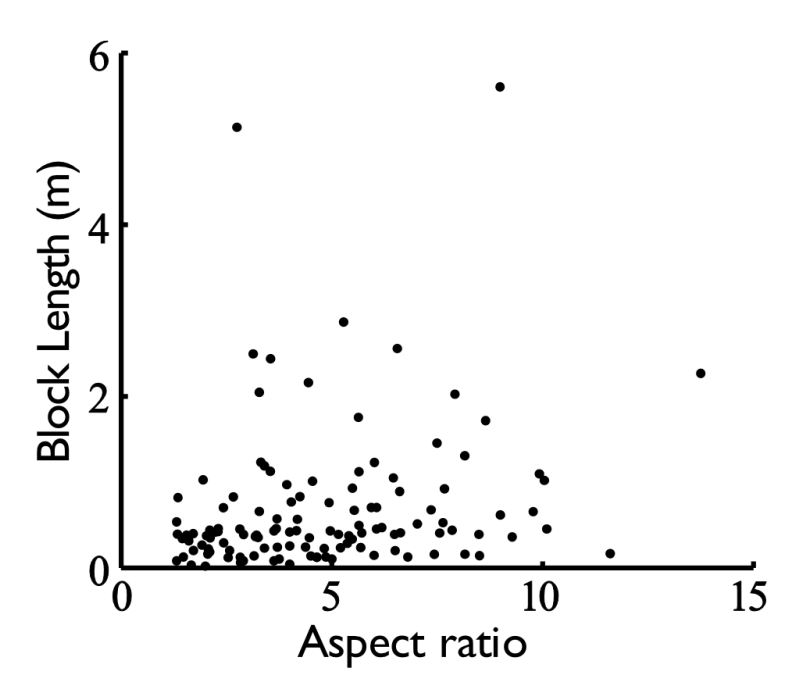


Figure C1. Relationship between basaltic block length and aspect ratio.

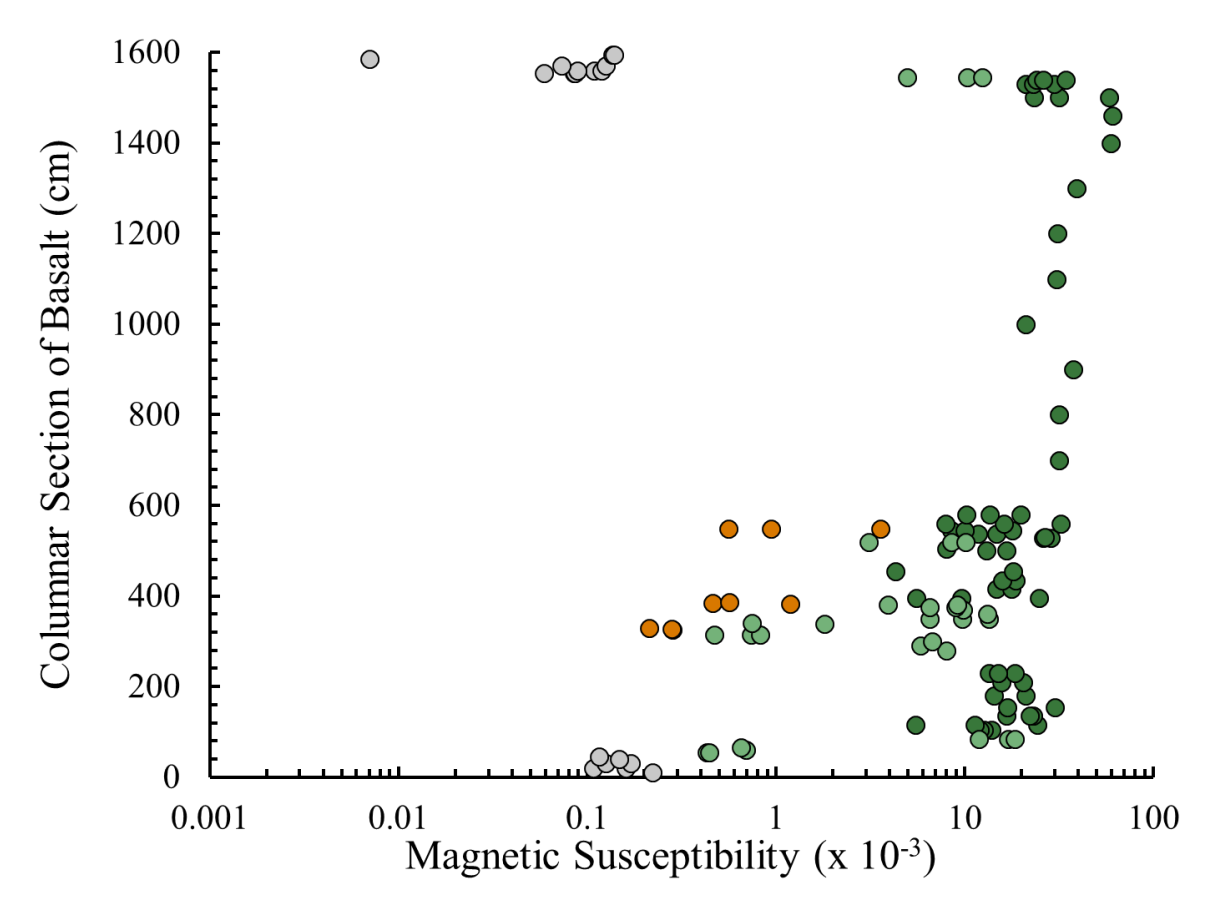


Figure C2. Magnetometer readings through the basaltic slab at the base of Unit 4. Dark green represents readings from basalt, light green from altered basalt, orange from late ankerite bearing faults cutting the basaltic slab and light grey from the shale matrix of the mélange above and below the basaltic slab.